PATH INTEGRAL MONTE CARLO AND THE ELECTRON GAS

BY

ETHAN W. BROWN

DISSERTATION

Submitted in partial fulfillment of the requirements
for the degree of Doctor of Philosophy in Physics
in the Graduate College of the
University of Illinois at Urbana-Champaign, 2014

Urbana, Illinois

Doctoral Committee:

Professor Taylor Hughes, Chair
Professor David M. Ceperley, Director of Research
Professor S. Lance Cooper
Dr. Jonathan DuBois, LLNL Mentor
Assistant Professor André Schleife

Abstract

Path integral Monte Carlo is a proven method for accurately simulating quantum mechanical systems at finite-temperature. By stochastically sampling Feynman's path integral representation of the quantum many-body density matrix, path integral Monte Carlo includes non-perturbative effects like thermal fluctuations and particle correlations in a natural way. Over the past 30 years, path integral Monte Carlo has been successfully employed to study the low density electron gas, high-pressure hydrogen, and superfluid helium. For systems where the role of Fermi statistics is important, however, traditional path integral Monte Carlo simulations have an exponentially decreasing efficiency with decreased temperature and increased system size. In this thesis, we work towards improving this efficiency, both through approximate and exact methods, as specifically applied to the homogeneous electron gas.

We begin with a brief overview of the current state of atomic simulations at finite-temperature before we delve into a pedagogical review of the path integral Monte Carlo method. We then spend some time discussing the one major issue preventing exact simulation of Fermi systems, the sign problem. Afterwards, we introduce a way to circumvent the sign problem in PIMC simulations through a fixed-node constraint. We then apply this method to the homogeneous electron gas at a large swatch of densities and temperatures in order to map out the warm-dense matter regime. The electron gas can be a representative model for a host of real systems, from simple medals to stellar interiors. However, its most common use is as input into density functional theory. To this end, we aim to build an accurate representation of the electron gas from the ground state to the classical limit and examine its use in finite-temperature density functional formulations.

The latter half of this thesis focuses on possible routes beyond the fixed-node approximation. As a first step, we utilize the variational principle inherent in the path integral Monte Carlo method to optimize the nodal surface. By using a ansatz resembling a free particle density matrix, we make a unique connection between a nodal effective mass and the traditional effective mass of many-body quantum theory. We then propose and test several alternate nodal ansatzes and apply them to single atomic systems. Finally, we propose a method to tackle the sign problem head on, by leveraging the relatively simple structure of

permutation space. Using this method, we find we can perform exact simulations this of the electron gas and ^{3}He that were previously impossible.

To Silva, my family, and my friends.

Acknowledgments

This thesis would not have been possible without oxygen, water, food, shelter, electricity, computers, and the notion that the universe operates on physical principles. Beyond these basic needs, it is unequivocally the people in my life that I must thank the most. David Ceperley has been an excellent adviser, granting guidance when needed, while providing ample space to explore the problems I find interesting. I certainly recognize that his support of me has shaped my career for the better, and I feel privileged to be counted among his students. I must also thank Jonathan DuBois for being a superb mentor during my time at Lawrence Livermore National Laboratory. I cherish both his advice and friendship, and I look forward to our continuing collaboration. I would also like to thank all my collaborators: Bryan Clark for showing me the proverbial *path integral ropes* and helping me through his and Ken Esler's PIMC++ suite, Markus Holzmann for providing derivations on a moments notice, and Berni Alder for being a constant reminder that I should strive to do impactful work. I want to thank both the Ceperley and Quantum Simulations groups for their willingness to share their knowledge and to go out for lunch. I want to thank my friends, with whom I spent many a late night, both working and not, and whose companionship I sincerely treasure. To my family: I am deeply thankful for your life-long love and unwavering support. You have provided me everything and shown me how to live well. Last, but not least, I am truly indebted to my wife and love, Silva Skenderi-Brown. Her enduring patience and compassion should never go unnoticed.

Funding Agencies: This work was supported by DOE grant DE-FG52-09NA29456. In addition, the work of E. Brown and J. DuBois was performed under the auspices of the U.S. Department of Energy by Lawrence Livermore National Laboratory under Contract DE-AC52-07NA27344 with support from LDRD 10-ERD-058 and the Lawrence Scholar program. Computational resources included LC machines at Lawrence Livermore National Laboratory through the institutional computation grand challenge program, and Jaguar and Kraken at Oak Ridge National Laboratory through XSEDE.

Academic Disclaimer: The author wrote this dissertation in support of requirements for the degree Doctor of Philosophy in Physics at University of Illinois, Urbana-Champaign. The research is funded in part by the LLNL Graduate Scholars Program, and is not a deliverable for any United States government

agency. The views and opinions expressed are those of the author, and do not state or reflect those of the United States government or Lawrence Livermore National Security, LLC.

Table of Contents

List of Tables

List of Figures

List of Abbreviations

BDHC	Brown-DuBois-Holzmann-Ceperley
DFT	density functional theory
HEG	homogeneous electron gas
HF	Hartree-Fock
KS	Kohn-Sham
KSDT	Karasiev-Sjostro-Dufty-Trickey
LDA	local density approximation
LFC	local field corrections
MD	molecular dynamics
OCP	one component plasma
OFDFT	orbital-free density functional theory
PDW	Perrot-Dharma-wardana
PIMC	path integral Monte Carlo
PZ	Perdew-Zunger
QMC	quantum Monte Carlo
RPA	random phase approximation
RPIMC	restricted path integral Monte Carlo
STLS	Singwi-Tosi-Land-Sjölander
TI	Tanaka-Ichimaru

List of Symbols

β	$(k_\beta T)^{-1}$
ρ	density matrix
τ	time step
Ψ	wave function
Ω	volume of the simulation cell
D	dimension of simulation cell
$\mathcal{H}$	Hamiltonian
$\mathcal{K}$	kinetic action
k_B	Boltzmann's constant
M	number of time slices
m_e	electron mass
N	number of particles
$\hat{\mathcal{O}}$	observable operator
$\mathcal{P}$	permutation operator
$\mathbf{R}$	DN-dimensional vector representing the positions of all the particles in the system
$\mathcal{S}$	imaginary-time action
T	temperature
$\mathcal{U}$	potential action
$\mathcal{Z}$	partition function

Chapter 1

Introduction

> *The underlying physical laws necessary for the mathematical theory of a large part of physics and the whole of chemistry are thus completely known, and the difficulty is only that the exact application of these laws leads to equations much too complicated to be soluble. It therefore becomes desirable that approximate practical methods of applying quantum mechanics should be developed, which can lead to an explanation of the main features of complex atomic systems without too much computation.*
>
> *Paul Dirac, 1929*

By the end of the 1920's, physicists had developed a near complete picture of the quantum mechanical principles governing ordinary matter. The culmination of this work is the Dirac equation (or Schrödinger equation if neglecting relativistic effects), whose solution exactly describes the behavior of quantum systems. If it were possible to find this solution for matter at normal energy scales, most of quantum chemistry, condensed matter physics and material science would be considered solved problems. Unfortunately, as the originators of these equations quickly realized, very few systems can be solved exactly. This led Dirac to give what is commonly known as *Dirac's challenge* in the epigraph. In line with these marching orders, since then much of theoretical physics, chemistry, and materials science has been devoted to finding better approximate methods that yield physically relevant results.

Originally, all this work was necessarily done analytically. However, with the advent of digital computers, numerics began to accomplish what was impossible before. Since the 1960's, these methods have improved dramatically due in part to faster machines, but mostly do to better algorithms. In recent decades, such methods have come to the fore, and simulation has become a ubiquitous tool, used in most major disciplines of scientific inquiry. In physics and chemistry, atomistic simulation can explore regimes that analytic study cannot broach, and numerical experiments are used to produce data that is either too expensive or difficult to attain through other means. Even still, there has yet to be a numerical method that can efficiently predict the properties of all systems. Instead a diaspora of methods has emerged, each with a specific realm of applicability. Some methods, however, maintain the potential to be *black boxes* with universal applicability, though algorithmic challenges remain.

In this thesis, we present another incremental step towards this goal both by applying an existing method, path integral Monte Carlo, to a previously unstudied system and by introducing methodological improvements to further expand its applicability. In the rest of this chapter, we discuss several atomistic simulation techniques, focusing specifically on each method's balance between efficiency and accuracy. We then introduce our system of interest, the homogeneous electron gas, and motivate it through the lens of a finite-temperature regime that is currently inaccessible to analytic study, warm-dense matter. Finally we provide an outline of the rest of the thesis.

1.1 Electronic structure methods

The purpose of any simulation method is to have real predictive power. To have this power when studying anything on the level of single atoms to molecules to whole crystals, one must account for the correlations between both the electrons and ions. Methods that do generally fall under the broad umbrella of *electronic structure*, referring to the effect the electronic orbitals of individual atoms may work in conjunction to affect the structure of a composite system. A superb review of electronic structure, including its history, theoretical background, numerics and experiment, can be found in Ref. [76]. Here we focus specifically on the simulation methods within electronic structure.

1.1.1 Classical simulation

Systems at extreme temperatures or with very weak quantum correlation are often studied with classical methods, i.e. methods that do not explicitly treat the quantum properties of the constituent particles. Accordingly, classical simulation is often used in the study of plasmas or biological molecules. Atoms are treated as distinguishable point particles, and usually a pairwise effective potential is meant to account for major correlation effects. Early potentials, such as those suggested by Leonard-Jones, were effective in describing noble gases. However, when the temperature is lowered or the average interparticle spacing is near the order of the thermal DeBroglie wavelength, quantum correlations become important, and classical simulation methods fail. In these situations, methods that address the quantum nature of the particles are necessary.

1.1.2 Tight-binding

Perhaps the most widely used of the electronic structure methods in condensed matter physics is the *tight-binding* method. In tight-binding each atom is treated as a fixed point in space with an associated number

of electronic orbitals, hence its other name in quantum chemistry, *linear combination of atomic orbitals* (LCAO). For N atoms with M orbitals per atom, there is a discrete basis of NM elements forming an $NM \times NM$ Hamiltonian matrix. Solving this system then simply amounts to diagonalizing this Hamiltonian to find the energy eigenstates. Naive diagonalization, however, can scale as poorly as $\mathcal{O}(N^M)$. This limits the success of this method to small systems unless qualifying approximations about the sparsity of the Hamiltonian can be made. The most common of these is to ignore the long-range character of a system and assume each atomic site only influences its nearest neighbors. Next- and next-next-nearest neighbor interactions can then be added back in sequentially until a result is converged.

In order to make connection with a real system, often, a parameterized analytic form for the matrix elements of the Hamiltonian is used, and the parameters are optimized to match the physical properties of the original system. This can limit the *transferability* of the tight-binding method. In other words the simulation may be very accurate for the system for which the parameters were created, however, when applied to another system results may be very poor. Nevertheless, tight-binding simulations have been successful at describing the behavior of many molecular and extended systems, e.g. lattices of atoms, where the long-ranged interactions of the constituent electrons are effectively screened by intermediate atomic sites.

The simplest, and historically first, implementation of tight-binding is the Hartree-Fock (HF) method. This method assumes the many-body wavefunction can be written as a single Slater determinant which is optimized self-consistently through a set of mean field equations. Thus interparticle correlations are largely ignored as Coulomb repulsion and fermionic exchange are only included as averaged quantities. The HF method is then only truly applicable to systems in which particle-particle correlation effects are weak.

It is possible to improve upon the HF method by perturbatively adding correlation corrections to the HF Hamiltonian through the Møllet-Plesset method. For weakly to moderately correlated systems, the second-order perturbation, MP2, can be satisfactory. For strongly correlated systems, however, the required higher level perturbations become increasingly expensive to compute.

The configuration-interaction method (CI) extends the single Slater determinant wave function of HF to a basis of determinants. When the basis is complete, the method is dubbed full CI (FCI), and is tantamount to exact diagonalization of the full Hamiltonian. As explained above this is often prohibitively expensive. Instead, often the Hamiltonian is constrained to a restricted subspace of low energy excitations. The number of such excitations can then be added in sequentially, though typically going beyond triple excitations is computationally intractable.

1.1.3 Ab initio

For some systems, important physics cannot be projected onto a tight-binding model, either due to their size, the necessary number of included orbitals, or their physical nature (e.g. quantum liquids). For such systems there are methods that take only the atomic number and position as input instead of trying to explicitly represent the many-body wave function. These methods are dubbed *ab initio*, or *from the beginning*, since they are formulated from first principles. They can be broadly divided into two subgroups: effective single particle and explicitly correlated methods.

Density functional theory

The most widely used example of an effective single particle method is density functional theory (DFT), which is discussed in detail in Chapter 4. In DFT, the many-body interacting problem is recast into a set of single-body non-interacting problems, each with an effective, mean-field external potential determined by the probability density of particles. DFT has seen tremendous success in the fields of quantum chemistry, biology, and material science [66]. It is among the most efficient of all the ab initio methods while maintaining real predictive power, making it the closest to being a black box that researchers can simply *use*. Nevertheless, it is not without its own issues.

As written originally by Hohenberg and Kohn [53], DFT is in principle an exact method. However, the precise form of the external potential functional of the probability density is not *a priori* known, and approximate ansatzes must be used instead. Many such approximate functionals exist, with varying levels of accuracy. The simplest is the local density approximation (LDA) in which the local electronic correlation energy is treated as if it is a homogeneous electron gas at the same density. The LDA fails when this correlation energy is not a smoothly varying function of the density, though it may be improved upon with gradient corrections (GGA). Even still DFT is restricted to systems in which correlation effects are not too important. In systems with strong electronic correlations, DFT can be qualitatively wrong. Moreover, assessing the relative accuracy of different functional ansatz within DFT can be a difficult task since there is no systematic way to converge to the correct solution, e.g. a variational principle.

Quantum Monte Carlo

When the above methods fail, it becomes necessary to use a method that is explicitly correlated. Quantum Monte Carlo (QMC) methods are among the most accurate available. In principle, they require no qualifying approximation and are able to solve the many-body problem exactly through a stochastic integration. Rather than explicitly attempting to represent the many-body wave function of the system, the

expectation values of observable operators are computed by sampling the positions of the electrons with a system dependent probability distribution function. Because the simulations take place in the configuration space of the electrons, correlation effects can be introduced in a natural way. As a result, these methods scale much more effectively with system size than the quantum-chemistry methods described above. For systems with fermions, however, enforcing anti-symmetry can make QMC methods scale exponentially due to sampled weights of approximately equal value and opposite sign. This exponential cost can be traded for an approximation which fixes the sign of the weights to be positive, though its application must be carefully controlled, as discussed in Chapter 3.

Because of their accuracy, QMC studies are often used as benchmarks with which to compare analytics, experiment, and other numerical methods. In fact, QMC estimates of the homogeneous electron gas are vital input for the LDA functional of DFT described above. Because of this and its canonical nature, the homogeneous electron gas has frequently been the target of methodological improvements in QMC methods.

1.2 Warm-dense matter

Together, the electronic structure techniques have been successful at exploring both the properties of condensed matter systems at low temperature as well as plasmas at high temperature (typically well above the Fermi temperature, T_F). However, there exists an important intermediate regime where *warm* states of matter are inadequately described by traditional theoretical frameworks. More precisely, warm-dense matter (WDM) is defined as the region of phase space where the Coulomb coupling parameter

$$\Gamma \equiv q^2/(ak_BT), \tag{1.1}$$

with a being the average interparticle spacing, and the electron degeneracy parameter

$$\Theta \equiv T/T_F \tag{1.2}$$

are both approximately unity. This implies that the electronic correlation of the system is on par with the relevant thermal effects. Likewise, quantum statistics play an important role, since here the average interparticle spacing is on the same order as the thermal DeBroglie wavelength. This places the WDM regime exactly in between weakly coupled plasma physics and condensed matter physics.

In the real universe, WDM is predicted to occur in planetary and stellar interiors [26]. Moreover, WDM has recently been shown to be accessible in several experimental setups. Within the condensed matter

physics community, interest has been stimulated by the emergence of new techniques for generating strong shock waves in materials via large-scale lasers, heavy ion beams, or energetic materials [17, 65]. Within the plasma physics community, the development of novel sources enabling experimental access to plasma-like states of matter at low temperature and high density has lead to emerging research opportunities at the forefront of the field [72]. All of these methods have the capability of being used in conjunction with one another, e.g. an explosively generated shock wave may be probed by an x-ray source, etc. Additionally short pulse lasers have recently been shown to be powerful tools in WDM research as they can be used to both produce and diagnose WDM [77]. In Fig. 1.1, we highlight the region of the temperature-density phase space occupied by the WDM regime.

The microscopic description of WDM poses a particular difficulty. Since WDM operates around the Fermi temperature and at high densities, classical mechanics is far from adequate. It is not convenient to describe the system as a perturbation from the ground state, that is as a sum over electronic excitations, since at this temperature there are so many states. The current workhorse of the WDM regime is DFT paired with molecular dynamics (DFTMD). However as the temperature is raised, this method quickly becomes computationally intractable due to spreading of the Fermi function and, consequently, an explosion in the number of orbitals needed to describe the relevant physics. At a sufficiently high temperatures, one needs a method that treats electrons and other quantum particles as particles and not as delocalized wavefunctions. Furthermore, at finite-temperature DFTMD introduces an uncontrolled approximation: the temperature dependence of correlation is included in an ad hoc way by naively using the zero-temperature exchange-correlation energy functional at a finite-temperature density. Without a reliable benchmark, it is possible that DFTMD at finite-temperature may currently be producing qualitatively different physical behavior than the real system being studied.

This dissertation will attempt to provide a solution to the these issues through the use and improvement of the path integral Monte Carlo (PIMC) method, a finite-temperature breed of QMC. Imaginary time path integrals provide a particularly fortuitous formalism for WDM, since they supply a direct mapping of the quantum system into a classical system and reduce to the classical limit at high temperature. A major conceptual difficulty preventing the straightforward use of the path integral method is the issue of how to map fermion statistics into a probability. As we discuss below, this has an *in principle* solution: the restricted path integral method. For PIMC to be a truly first principles method and join its zero-temperature analogues as a gold standard benchmark, we must carefully account for errors associated with the restriction and search for ways to ameliorate them. To this end, we choose the lens of the homogeneous electron gas (HEG) due its simplicity, range of character, and ubiquitous application as a model and benchmark. Our

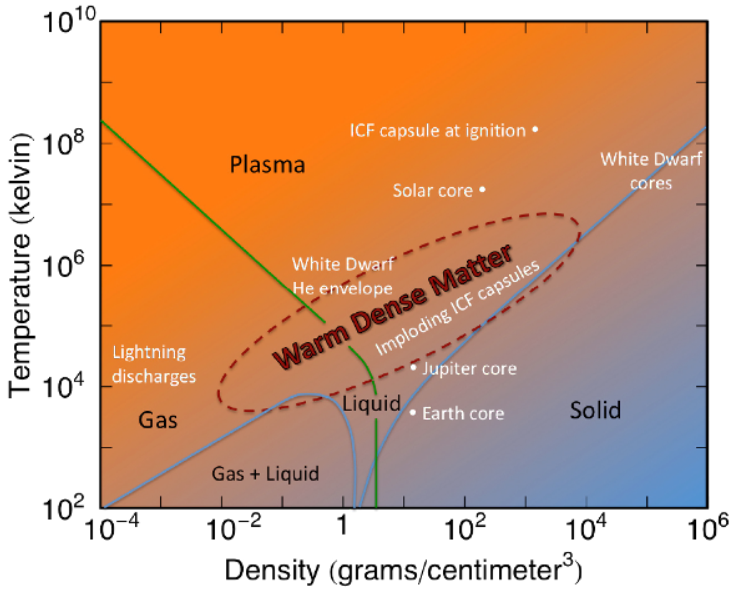

Figure 1.1: Regions of the warm-dense regime accessible to various experimental setups [94].

efforts to improve the PIMC method will then translate to improvements in methods that depend on the precise estimates of the HEG at finite-temperature, specifically the DFTMD used to study WDM.

1.3 Outline

Here we provide an account of the organization of this material.

The first section of the thesis is predominantly methodological. We begin in Chapter 2 with a detailed account of the path integral Monte Carlo method. We pay specific attention to the implementation of long-ranged Coulomb potentials in PIMC through the use of Ewald summation. As mentioned, for fermions the sign problem prevents efficient simulation thus in Chapter 3, we spend some time discussing the one possible solution, the fixed-node constraint. We again specifically examine its use in Coulomb systems, with an emphasis on implementation and possible ergodicity issues. Next, in Chapter 4 we provide a brief overview of the density functional theory (DFT) method as one motivation for studying the homogeneous electron gas. We make sure to include a discussion of both zero- and finite-temperature formulations and point out the current issues with the latter.

In Chapter 5, we apply the restricted PIMC method to the homogeneous electron gas at a large swatch of densities and temperatures in order to map out the warm-dense matter regime. We find the simple free particle nodal structure to provide an accurate representation of the actual nodal structure by connecting to previous classical and ground state results. In this chapter, we attempt to be in line with scientific

provenance, giving as many simulation details as possible in order to allow reproducibility. With this data, in Chapter 6, we fit an analytic form to the exchange-correlation energy of the electron gas from the ground state to the classical limit and examine its use in an actual finite-temperature density functional formulation of atomic aluminum. Not surprisingly, we find that discrepancies emerging from the more accurate finite-temperature dependence translate in to discrepancies of the aluminum phase diagram.

The latter half of this thesis focuses on possible routes beyond the fixed-node approximation. As a first step, in Chapter 7 we utilize the variational principle inherent in the path integral Monte Carlo method to optimize the nodal surface. By using an ansatz resembling a free particle density matrix, we make a unique connection between a nodal effective mass and the traditional effective mass of many-body quantum theory. We then propose and test several alternate nodal ansatzes and apply them to single atomic systems. Finally in Chapter 8, we propose a method to tackle the sign problem head on, by leveraging the relatively simple structure of permutation space. Using this method, we find we can perform exact simulations this of the electron gas and ^{3}He that were previously impossible.

Chapter 2

Path integral Monte Carlo

In this chapter, we provide an overview of the path integral Monte Carlo (PIMC) method. For a more complete discussion of PIMC for bosons, we refer the reader to David Ceperley's review [21]. PIMC is a computational method for simulating many-body physics. PIMC can provide essentially exact thermodynamic measurements for systems in equilibrium. Unlike many other methods which purport to do the same, PIMC is not based off ground state wave functions but off the semi-classical path integral picture of the many-body density matrix originally introduced by Feynman [43]. This feature grants PIMC simple access to finite-temperature quantum-mechanical quantities while maintaining a classical analogue. In the proceeding we will derive the method from first-principles, discuss the specifics of computing actions, and finally give details of an actual PIMC simulation.

2.1 Formalism

We define the many-body density matrix to be

$$\rho(R, R'; \beta) = \langle R \mid e^{-\beta \hat{H}} \mid R' \rangle \tag{2.1}$$

where $R \equiv (r_1, \ldots, r_N)$ with r_i specifying the D-dimensional coordinates of the i^{th} of N particles, $\beta \equiv 1/k_B T$, and $\mathcal{H}$ specifying the many-body Hamiltonian. In this form ρ solves the many-body Bloch equation given by

$$-\frac{d}{d\beta}\rho = \hat{\mathcal{H}}\rho \tag{2.2}$$

with the initial condition $\rho(R, R'; 0) = \delta(R - R')$. It is also possible to write ρ as a Boltzmann factor weighted sum over eigenstates of $\mathcal{H}$,

$$\rho(R, R'; \beta) = \sum_i \Psi_i^\dagger(R)\Psi_i(R) \exp\left[-\beta E_i\right] \tag{2.3}$$

though in the proceeding we focus mainly on the form in (2.1).

The thermal expectation value of any observable may be computed from this definition by

$$\begin{aligned} \langle \hat{\mathcal{O}} \rangle &= Tr(\hat{\mathcal{O}}\rho)/Tr(\rho) && (2.4) \\ &= \frac{1}{\mathcal{Z}} \int dR \langle R \mid \hat{\mathcal{O}} e^{-\beta \hat{\mathcal{H}}} \mid R \rangle. && (2.5) \end{aligned}$$

where we have defined the quantum statistical partition function $\mathcal{Z}$ as the trace of the density matrix,

$$Z(\beta) = Tr(\rho) = \int dR \langle R \mid e^{-\beta \hat{H}} \mid R \rangle = \int dR \rho(R, R; \beta). \tag{2.6}$$

If we knew $\rho(R, R'; \beta)$, we would be ready for simulation. However, the many-body density matrix is almost always not known in a closed form for arbitrary temperatures. In order to transform the above to something more amenable to direct calculation, we utilize the convolution property of density matrices, i.e.

$$\begin{aligned} \rho(R, R'; \beta) &= \langle R \mid e^{-\beta \hat{H}} \mid R' \rangle && (2.7) \\ &= \int dR'' \langle R \mid e^{-\frac{\beta}{2} \hat{H}} \mid R'' \rangle \langle R'' \mid e^{-\frac{\beta}{2} \hat{H}} \mid R' \rangle && (2.8) \\ &= \int dR'' \rho(R, R''; \frac{\beta}{2}) \rho(R'', R'; \frac{\beta}{2}). && (2.9) \end{aligned}$$

By inserting the resolution of identity, we are left with the product of two density matrices at twice the temperature $\frac{\beta}{2}$. Repeating this procedure M times, such that $\beta = M\tau$, the many-body density matrix becomes

$$\rho(R, R'; \beta) = \int dR_1 dR_2 \dots dR_{M-1} \rho(R, R_1; \tau) \rho(R_1, R_2; \tau) \dots \rho(R_{M-1}, R'; \tau). \tag{2.10}$$

Thus we have effectively reduced the problem of finding a low temperature density matrix to one of finding the product of many high temperature density matrices. As the temperature raises, the density matrix becomes increasingly classical and potentially solvable. In the next section, we will outline how we compute the solution for each high temperature density matrix.

In order to properly account for the quantum statistics of the simulated particles, we must sum over all possible permutations $\mathcal{P}$ of the corresponding symmetry group $\mathcal{S}_N$ with their respective sign weights. All bosonic configurations are positive, while for fermions configurations with an odd number of odd permuta-

tions are negative. We are left with the following expression for our many particle partition function

$$Z(\beta) = \frac{1}{N!}\sum_{\mathcal{P}\in\mathcal{S}_N}(\pm 1)^{\mathcal{P}}\int dR\rho(R,\mathcal{P}R;\beta) \tag{2.11}$$

$$= \frac{1}{N!}\sum_{\mathcal{P}\in\mathcal{S}_N}(\pm 1)^{\mathcal{P}}\int dR\int dR_1\dots dR_{M-1}\rho(R,R_1;\tau)\dots\rho(R_{M-1},\mathcal{P}R;\tau) \tag{2.12}$$

where the sign is + for bosons and − for fermions.

All that remains is the calculation of each high temperature $\rho(R,R';\tau)$. Before we move on, however, it is important to point out that we have already arrived at the Feynman path integral picture [43]. To compute an observable, as in (2.4), we must trace over all possible paths from R to R_1 through R_{M-1} and back to R. This is the imaginary time version of the *sum over histories* Feynman developed for quantum electrodynamics. The difference here is that the paths loops back on one another forming structures resembling classical ring polymers, which turns out to be a very useful physical analogue when doing actual simulations.

2.2 Computing actions

For each high temperature density matrix in (2.10), we may define an imaginary time action

$$S(R,R';\tau) \equiv -ln[\rho(R,R';\tau)]. \tag{2.13}$$

Using (2.1) we see this is nothing more than $\tau\hat{\mathcal{H}}$. We define the Hamiltonian in the usual way

$$\hat{\mathcal{H}} = \hat{T}+\hat{V} \tag{2.14}$$

$$= -\sum_i[\lambda_i\nabla_i^2 + V_{ext}(r_i)] + \frac{1}{2}\sum_{i\neq j}V_{ij}(|r_i-r_j|) \tag{2.15}$$

where we have defined $\lambda_i \equiv \frac{\hbar^2}{2m}$, V_{ext} is an external potential, and V_{ij} is a pair potential. Because the kinetic and potential terms in (2.14) do not generally commute, writing a closed form for action can be a difficult task. Nevertheless, we still find it convenient to break it up into kinetic and potential parts, which we define

$$\mathcal{K}(R,R';\tau) = -ln[e^{-\tau\hat{T}}] \tag{2.16}$$

$$\mathcal{U}(R,R';\tau) = -ln[e^{-\tau(\hat{T}+\hat{V})}] - \mathcal{K}(R,R';\tau). \tag{2.17}$$

It is possible to solve for the free kinetic piece analytically to be

$$\mathcal{K}(R,R';\tau)=\sum_i[\frac{D}{2}ln(4\pi\lambda\tau)+\frac{|r_i-r_i'|^2}{4\lambda\tau}]. \tag{2.18}$$

In periodic boundary conditions with $\Omega=L^D$ this becomes

$$\mathcal{K}(R,R';\tau)=\sum_i[\frac{D}{2}ln(4\pi\lambda\tau)+\sum_n\frac{|r_i-r_i'+nL|^2}{4\lambda\tau}]. \tag{2.19}$$

where $n\equiv(n_0,\ldots,n_D)$ with $n_i=-\infty,\ldots,\infty$.

The more difficult task is computing (2.17) since there is not necessarily an analytic form for the many-body interacting problem. In fact, to our knowledge, a form only exists for free particles in a box or harmonic trap and the two-body problem. Thus, in the following sections we will discuss approximate ways to compute $\mathcal{U}$.

2.2.1 Primitive approximation

The simplest thing we can do is just assume $\hat{T}$ and $\hat{V}$ do commute and separate the exponential. According to Trotter's theorem

$$e^{-\tau(\hat{T}+\hat{V})}=\lim_{M\to\infty}(e^{-\frac{\tau}{M}\hat{T}}e^{-\frac{\tau}{M}\hat{V}})^M. \tag{2.20}$$

More explicitly, one can show [30]

$$e^{-\tau(\hat{T}+\hat{V})}=e^{-\tau\hat{T}}e^{-\tau\hat{V}}e^{-\frac{\tau^2}{2}[\hat{T},\hat{V}]}e^{-\frac{\tau^3}{6}[[\hat{T},\hat{V}],\hat{T}+2\hat{V}]}e^{-\mathcal{O}(\tau^4)}. \tag{2.21}$$

The *primitive approximation* ignores all terms of $O(\tau^2)$ and smaller, becoming exact in the limit $\tau\to 0$. Within the primitive approximation, $\mathcal{U}$ may be written,

$$\mathcal{U}(R,R';\tau)=\frac{\tau}{2}(V(R)+V(R')). \tag{2.22}$$

The many-body density matrix then becomes

$$\rho(R,R';\beta) \quad = \quad \int dR_1dR_2\ldots dR_{M-1}\exp[-\sum_{i=0}^{M}[\frac{ND}{2}ln(4\pi\lambda\tau)+\sum_n\frac{|R_{i-1}-R_i+nL|^2}{4\lambda\tau}+\tau V(R_i+nL)]$$

where we have defined $R_0\equiv R$ and $R_M=R'$. Here the classical isomorphism becomes apparent. The kinetic piece forms spring-like bonds between adjacent time slices with the first and last time slices being

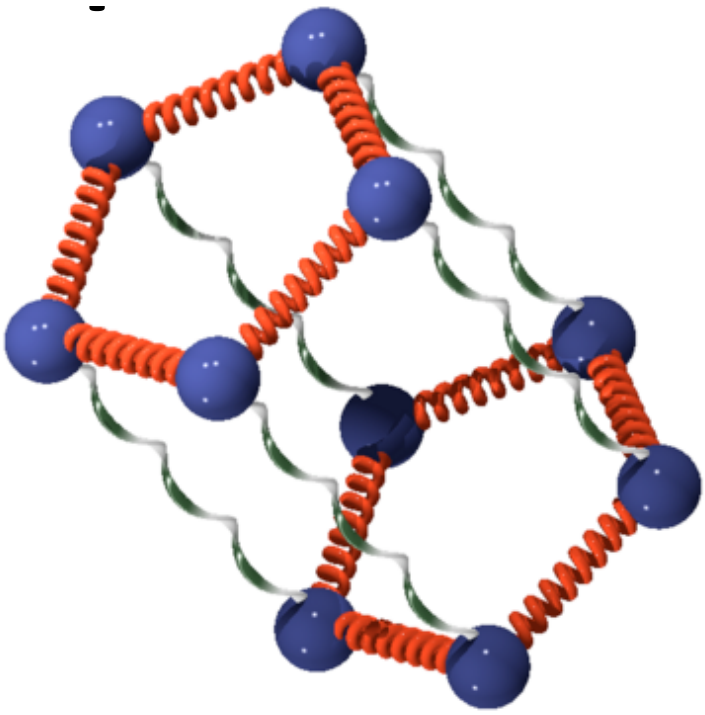

Figure 2.1: Classical physical picture of a path integral Monte Carlo simulation of 2 particles, each with 5 time slices. Here the purple balls represent each bead along the path of a single particle. The red springs represent the kinetic spring action between time slices of the same particles. The silver curls represent the interparticle potential present between beads of like time slices on different paths.

the same. The potential piece interacts between all N particles in the same time slice. Each particle then forms a necklace of beads, one for each time slice, forming a closed path, see Fig (2.2.1). Throughout the remainder of the text, we will use this nomenclature of *bead* to describe the individual time slices of a particle's trajectory and *path* to describe the closed loop it forms.

Often times a more precise form of the action is required for proper convergence. At low temperatures, paths in the primitive approximation are necessarily long due to the $\mathcal{O}(\tau^2)$ convergence. A better action can speed up the convergence in τ, thus requiring fewer time slices and shorter paths. Many such higher-order approximations exist [30, 99], however here we focus specifically on what is termed the *pair approximation*.

2.2.2 Pair approximation

Taking the $M \to \infty$ of (2.10) allows us to rewrite the density matrix in the traditional continuous path integral formalism as,

$$\rho(R, R'; \tau) = \int_{R \to R'} dR_t e^{-S(R_t)} \tag{2.23}$$

$$= \int_{R \to R'} dR_t \exp\left[-\int_0^\tau dt(\lambda \dot{R_t}^2 + V(R_t))\right] \tag{2.24}$$

where $S(R_t)$ is now the continuous imaginary-time action. We can rewrite this to be

$$\rho(R, R'; \tau) = \int_{R \to R'} dR_t \exp[-\int_0^\tau dt \lambda \dot{R_t}^2] \exp[-\int_0^\tau dt V(R_t))] \tag{2.25}$$

$$= \rho_0(R, R'; \tau) \frac{\int_{R \to R'} dR_t \exp[-\int_0^\tau dt \lambda \dot{R_t}^2] \exp[-\int_0^\tau dt V(R_t))]}{\rho_0(R, R'; \tau)} \tag{2.26}$$

$$\equiv \rho_0(R, R'; \tau) \langle e^{-\int_0^\tau dt V(R_t)} \rangle_{BRW} \tag{2.27}$$

where we have now defined $\rho_0(R, R'; \tau) \equiv \int_{R \to R'} dR_t exp[-\int_0^\tau dt \lambda \dot{R_t}^2]$ as the many-body free particle density matrix. The notation $\langle \dots \rangle_{BRW}$ denotes an average over the Brownian random walk created by the free particle weights, a method originally developed by Feynman and Kac [43].

The base approximation of the pair action is to assume the many-body action may be written as a product of 2-body actions. To start, we return to (2.27), looking specifically at the potential piece. If we have only pairwise interactions, we may write

$$\langle e^{-\int_0^\tau dt V(R(t))} \rangle_{BRW} = \langle \prod_{i<j} e^{-\int_0^\tau dt v(r_{ij}(t))} \rangle_{BRW} \tag{2.28}$$

where the product is over all pairs of particles, $r_{ij} \equiv |r_i - r_j|$, and $v(r_{ij})$ is a pairwise potential. Looking at the form of the kinetic action in (2.19) and the Feynman-Kac representation in (2.27), it becomes clear that for small τ paths going straight from R to R' contribute most to the BRW average. Paths that stray from a straight line are exponentially suppressed by the Gaussian weight. Thus for reasonably small τ, we can write

$$\langle \prod_{i<j} e^{-\int_0^\tau dt v(r_{ij}(t))} \rangle_{BRW} \approx \prod_{i<j} e^{-\tau \int_0^1 dt v([1-t]r_{ij} + t r'_{ij})} \tag{2.29}$$

This will also be true for a two-particle system,

$$\langle e^{-\int_0^\tau dtv(r_{ij}(t))}\rangle_{BRW} \approx e^{-\tau\int_0^1 dtv([1-t]r_{ij}+tr'_{ij})}, \tag{2.30}$$

which leads us to the conclusion that for small τ

$$\langle e^{-\int_0^\tau dtV(R(t))}\rangle_{BRW} \approx \prod_{i<j}\langle e^{-\int_0^\tau dtv(r_{ij}(t))}\rangle_{BRW}. \tag{2.31}$$

It is worth noting that this final approximation should hold for larger τ than the approximations in (2.29) and (2.30) since the paths thrown out in these are now reintroduced.

From here, we rewrite the many-body density matrix as

$$\rho(R,R';\tau) \approx \rho_0(R,R';\tau)\prod_{i<j}e^{-u(r_i,r_j,r'_i,r'_j;\tau)} \tag{2.32}$$

$$\approx \prod_{i<j}\rho(r_i,r_j,r'_i,r'_j;\tau) \tag{2.33}$$

which defines both the *pair action* $u(r_i,r_j,r'_i,r'_j;\tau)$ and *pair density matrix* $\rho(r_i,r_j,r'_i,r'_j;\tau)$. Thus the process of finding a high-temperature density matrix has been reduced to finding the product of many high-temperature, two-body density matrices. Calculating $\rho(r_i,r_j,r'_i,r'_j;\tau)$ will be the subject of the following sections.

2.2.3 Computing pair actions

There exist several ways to exactly compute the two-body density matrix, though we only highlight a couple here. To begin for any pair of particles, one may write the $4D$ dimensional pair density matrix in a combination of center of mass $\bar{r} = \frac{m_i r_i + m j r_j}{m_i + m_j}$ and relative coordinates $r_{ij} = r_i - r_j$,

$$\rho(r_i,r_j,r'_i,r'_j;\tau) = \rho_{cm}(\bar{r},\bar{r}';\tau)\rho_{rel}(r_{ij},r'_{ij};\tau) \tag{2.34}$$

where center of mass piece is simply the free particle action $\rho_0(\bar{r},\bar{r}';\tau)$. For any central potential, the ρ_{rel} may be be expanded in partial waves as [98]

$$\rho_{rel}(r_{ij},r'_{ij};\tau) = \frac{1}{4\pi r r'}\sum_{l=0}^{\infty}(2l+1)\rho_l(r,r',\tau)P_l(cos(\theta)) \tag{2.35}$$

where P_l are Legendre polynomials, $r \equiv |r_{ij}|$, and θ is the angle between r_{ij} and r'_{ij}, leaving only three free parameters.

The first route to computing $\rho_l(r, r'; \tau)$ is the simple summation over eigenstates mentioned in (2.3). Expressed in terms of radial eigenfunctions this is

$$\rho_l(r, r'; \tau) = \sum_i \Psi^\dagger_{i,l}(r)\Psi_{i,l}(r') \exp\left[-\tau E_i\right] + \int_0^\infty dk \Psi_{k,l}(r)^\dagger \Psi_{k,l}(r') \exp\left[-\tau E_k\right] \tag{2.36}$$

representing both bound and continuum states. If the eigenstates are known with high precision, this is the preferred method of calculation. With increased temperature, more eigenstates must be included in the sum, however in most situations this is not a bottleneck.

When the ground state wavefunctions of a pair potential are not known, the method of choice is the matrix squaring technique. Matrix squaring again relies on the convolution property of density matrices given in (2.9), but extended to partial waves

$$\rho_l(r, r'; \tau) = \int_0^\infty dr'' \rho_l(r, r''; \frac{\tau}{2}) \rho_l(r'', r'; \frac{\tau}{2}). \tag{2.37}$$

In practice this integral may not be taken exactly since one does not know the exact form of the high-temperature density matrix. However, at a high enough temperature $2^n/\tau$, the semi-classical approximation presented in (2.30) is sufficiently accurate. This makes the matrix squaring procedure to attain $\rho_l(r, r'; \tau)$ a simple two-step process: First, for some sufficiently high temperature, use the semi-classical approximation,

$$\rho_l(r, r'; \tau/2^n) = \rho_{l,0}(r, r'; \tau) \exp\left[-\frac{\tau}{2^n} \int_0^1 v([1-t]r + tr')dt\right] \tag{2.38}$$

where $\rho_{l,0}(r, r'; \tau/2^n)$ is the free particle density matrix in radial coordinates. Second, do n squaring procedures as

$$\rho_l(r, r'; \tau/2^i) = \int_0^{r_c} dr'' \rho_l(r, r''; \tau/2^{i+1}) \rho_l(r'', r'; \tau/2^{i+1}) + \int_{r_c}^\infty dr'' F(r, r', r''; \tau/2^{i+1}) \tag{2.39}$$

where we have introduced a cutoff r_c, i runs from n to 0, and $F(r, r', r''; \tau)$ is an analytically solvable approximation, see [98].

Once $\rho_l(r, r'; \tau)$ is computed, one can again form $\rho_{rel}(r_{ij}, r'_{ij}; \tau)$ through (2.35). The pair action may

then be written,

$$u(r_{ij}, r'_{ij}; \tau) \equiv -\ln[\frac{\rho_{rel}(r_{ij}, r'_{ij}; \tau)}{\rho_0(r_{ij}, r'_{ij}; \tau)}] \tag{2.40}$$

as in (2.33). For computational convenience, this is often fitted to an expansion of three alternative degrees of freedom defined as $s \equiv \mid r_{ij} - r'_{ij} \mid, z \equiv \mid r_{ij} \mid - \mid r'_{ij} \mid, q \equiv (\mid r_{ij} \mid + \mid r'_{ij} \mid)/2$. This allows us to write,

$$u(r_{ij}, r'_{ij}, \tau) = \frac{1}{2}(u(r_{ij}, r_{ij}, \tau) + u(r'_{ij}, r'_{ij}, \tau)) + \sum_{k=1}^{k_{max}} \sum_{j=0}^{k} u_{kj}(q, \tau) z^{2j} s^{2(k-j)} \tag{2.41}$$

where the first term is simply the primitive approximation.

As an example of both approaches, we examine the Coulomb potential whose two-body ground state wavefunctions can be readily computed, see Appendix A. Additionally, because of a special property of the $1/r$ potential in 3-dimensional space, the z term in the sum in (2.41) may be completely neglected [93]. Naively we expect the direct partial wave summation to perform better since the Coulomb eigenstates are known exactly. However it is useful to see under what conditions the matrix squaring technique is comparable in order to act as a guide for other potentials and boundary conditions when the eigenstates are not known.

To begin we compare the diagonal density matrix for both approaches for two electrons with $\tau = 1/10$. Near the origin, $r_{ij}, r'_{ij} \to 0$, we expect the pair action to behave as predicted analytically (see Appendix A),

$$\lim_{r,r' \to 0} u(r, r'; \tau) = u(0, 0; \tau) - \frac{Z_1 Z_2}{2\lambda}(r + r') \tag{2.42}$$

where the first term is the exact cusp condition given by

$$u(0, 0; \tau) = \sum_{i=1}^{\infty} (\pm 1)^i \kappa_i \gamma^{i/2} \tag{2.43}$$

with the parameters κ_i come from the cumulant expansion of $\rho_{rel}(r, r'; \tau)$. The sign is $+$ for repulsive interactions and $-$ for attractive interactions. The second term is the $1s$-orbital contribution. For large separations, $r_{ij}, r'_{ij} \gg 1$, we expect the diagonal pair action to behave as in the primitive approximation, giving back a $1/r$ potential. In Fig. 2.2.3 we plot this behavior for three different values of τ. We see that at larger τ, the primitive approximation becomes closer to the exact action, i.e. the pair action becomes $1/r$.

Both approaches are able to recreate the results in Fig. 2.2.3 with great accuracy. However, we find that at high temperature (small τ), the eigenstate summation becomes numerically unstable for large distances and repulsive interactions for the exchange pair action. This can be overcome by first fitting the same

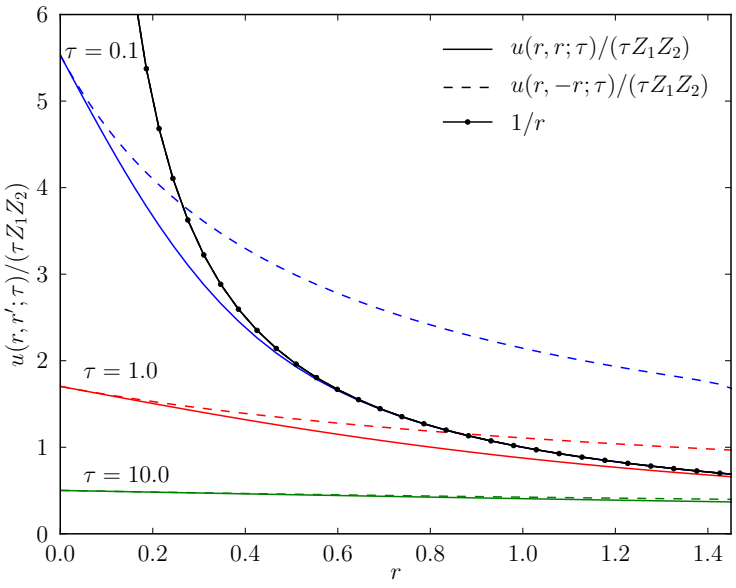

Figure 2.2: Direct (solid lines) and exchange (dashed lines) electron-electron pair actions for three different values of τ computed with the sum over eigenstates method of (2.3). For each the exchange term, when $r' = -r$, is larger since the path must diffuse around regions of high potential to go from r to $-r$. At $r = 0$, all actions reach the proper cusp condition. At large r, the diagonal action, $r' = r$ becomes $1/r$ (black solid-dotted line) and the primitive approximation becomes exact.

exchange pair action with attractive interactions to a cumulant expansion as in (2.43). On the contrary, the matrix squaring technique requires a fine grid close to the origin in order to recover the create cusp condition. Additionally larger values of τ require more squaring steps and with each comes possible numerical instability. For a detailed comparison, we point the reader to Ref. [38].

2.2.4 Long range potentials

Using the above prescription for the pair action works well when studying isolated systems of atoms or molecules. However, often times one wishes to extrapolate to the thermodynamic limit which necessitates the use of periodic boundary conditions. In a periodic box of length L the total potential becomes

$$V = \sum_{i<j} \sum_{n=0}^{\infty} v(r_{ij} + nL) + \frac{1}{2} \sum_{i=1}^{N} \sum_{n\neq 0}^{\infty} v(nL) \tag{2.44}$$

where we have included a sum over all periodic images. If $v(r) \sim 1/r$, this expression only converges conditionally. The solution to this issue was first presented by Ewald [39], in which one breaks the potential

into short range and long range parts such that

$$v_{EW}(r_{ij}) = \sum_{n=0}^{\infty} v_s(r_{ij} + nL) + \sum_{k\neq 0} \tilde{v}_l(k) e^{ikr_{ij}} + v_{BG} \tag{2.45}$$

where $\tilde{v}_l(k)$ is the Fourier transform of the long range piece, and v_{BG} is a constant term which guarantees charge neutrality given by $\tilde{v}_s(0) + \tilde{v}_l(0)$. This makes the total potential

$$V = \sum_{i<j} v_{EW}(r_{ij}) + \sum_i v_M \tag{2.46}$$

where v_M is the constant Madelung correction given by $v_M = \frac{1}{2} \lim_{r\to 0}[v_{EW}(r) - v(r)]$.

Traditionally v_l is chosen to be a Gaussian screened Coulomb potential and $v_s(r) = v(r) - v_l(r)$. However this choice is arbitrary, and it has been shown that one can minimize the required number of terms in each sum through least squares optimization [82]. The fit may either be formed in real space or momentum space and may be applied to either the short range piece or the long range piece. Some have reported greater numerical accuracy through real space fitting, though it is also more computationally demanding [38, 81]. When dealing with irregular potentials (e.g. pseudopotentials), it may be favorable to fit the long range piece which often has a regular $(1/r^n)$ decay. For all possible choices, the result is usually expressed as an expansion in a basis of piecewise quintic Hermite polynomials. The other piece (long or short) is the difference between this expansion and the original potential. It is often computationally convenient to choose $v_s(r)$ to go to zero at a cutoff distance less than half the box width such that only a single image in required. Thus the result is usually written

$$v_{OPT}(r_{ij}) = v_s(r_{ij}) + \sum_{\substack{k\neq 0 \\ |k|<k_c}} \tilde{v}_l(k) e^{ikr_{ij}} + v_{BG} \tag{2.47}$$

where k_c is a numerically sufficient cutoff in momentum space.

When dealing with a long range pair action, similar choices arise. The first (historical) option is to use the short range potential from the optimized Ewald breakup to form a short range pair action $u_s(r, r'; \tau)$. The long range piece is then added back in through the primitive approximation as

$$u_{OPT}(r, r'; \tau) = u_s(r, r'; \tau) + \frac{\tau}{2} \sum_{\substack{k\neq 0 \\ |k|<k_c}} \tilde{v}_l(k)(e^{ikr} + e^{ikr'}) + u_{BG}, \tag{2.48}$$

though random phase approximation corrections to the long range piece can also be included. In this case

the matrix squaring technique is preferable since the eigenstates of $v_s(r)$ are not generally known. The short range piece $u_s(r, r'; \tau)$ is fit to the same form as (2.41).

A second option is to perform the optimized breakup on the diagonal pair action itself [81]. Starting from the primitive approximation of the Ewald potential, off-diagonal information is added through a correction term as

$$u_{OPT}(r, r'; \tau) = \frac{\tau}{2}(v_{OPT}(r) + v_{OPT}(r')) + \sum_{n,n'=0}^{\infty} \Delta u(r + nL, r' + n'L; \tau) \tag{2.49}$$

where $\Delta u(r, r'; \tau) \equiv u(r, r'; \tau) - \frac{\tau}{2}(v(r) + v(r'))$. This correction decays faster than the bare potential because at long distances the primitive approximation becomes numerically exact, and thus the sum converges for finite n. The advent of this method is that the $u(r, r'; \tau)$ in the correction term is the precisely the pair action derived from $v(r)$ in the previous section. For the Coulomb potential then, one can calculate it by summing over its known eigenstates instead of using the matrix squaring method. Finally, $\Delta u(r, r'; \tau)$ can be fit to the same form as (2.41) for computational convenience.

For both methods, to reform the full pair action, one uses a form analogous to (2.46)

$$\mathcal{U}(R, R'; \tau) = \sum_{i<j} u_{OPT}(r_{ij}, r'_{ij}; \tau) + \tau \sum_i v_M. \tag{2.50}$$

Either way one wishes to include the long range potential, both the above approximations are controllable through the time step τ. More specifically since both rely on the primitive approximation, they will converge to the exact answer as $\mathcal{O}(\tau^2)$. It is important to note, however, that the prefactor of this convergence should in principle be much smaller since the primitive approximation is generally good at larger distances, presumably where the long range pair action becomes important.

2.3 Monte Carlo Sampling

With the above path integral expressions, we may now numerically evaluate observables of interest. In order to perform such high-dimensional integrals, we rely on the Metropolis Monte Carlo scheme. [79]

2.3.1 Metropolis Monte Carlo

This method for numerical integration ensures convergence provided *ergodicity* and *detailed balance*. Ergodicity guarantees the entire configuration space is accessible through a finite sequence of MC steps. Detailed

balance may be stated as

$$T(R \to R') \times A(R \to R') \times \rho(R, R; \beta) = T(R' \to R) \times A(R' \to R) \times \rho(R', R'; \beta) \tag{2.51}$$

where $T(R \to R')$ is the probability of proposing a MC move $R \to R'$, $\rho(R, R; \beta) = \exp[-S(R, R; \beta)]$ is the statistical weight of the configuration R, and $A(R \to R')$ is the probability of accepting the proposed move.

Typical moves consist of translating some portion of the path containing several time slices. A procedure is followed to design the new path, defining the sampling probability $T(R \to R')$. If one then defines the acceptance probability as

$$A(R \to R') = min\{1, \frac{T(R' \to R)\rho(R', R'; \beta)}{T(R \to R')\rho(R, R; \beta)}\}, \tag{2.52}$$

it is easy to see the algorithm obeys the detailed balance condition. Thus, provided all domains of the configuration space is accessible, we are guaranteed under the central limit theorem to converge to the equilibrium distribution. The details of these sampling moves are outlined in the next few sections.

2.3.2 Bisection

The simplest possible move would be to displace a random, single bead of a random, single path iteratively. However, this process lacks efficiency. Instead it is much more efficient to displace large swaths of beads through a multilevel *bisection*. An L-level bisection move operates on $2^L + 1$ adjacent time beads, though the end beads remain fixed and only $2^L - 1$ beads are moved. At the first stage, a new location is chosen for the middle bead, creating two new segments. Next, the new middle bead location is fixed while the beads at the center of the two new segments are placed at new locations. This process is repeated until all the $2^L - 1$ have been displaced.

For a $L = 1$ level bisection at bead t, the acceptance probability is

$$\begin{aligned} A(r_b \to r'_b) &= min\{1, \frac{T(r_b \to r'_b)\exp[-S(r_{b-1}, r'_b; \tau) - S(r'_b, r_{b+1})]}{T(r'_b \to r_b)\exp[-S(r_{b-1}, r_b; \tau) - S(r_b, r_{b+1})]}\} & (2.53) \\ &= min\{1, \frac{T(r_b \to r'_b)}{T(r'_b \to r_b)}\exp[-\Delta\mathcal{K}]\exp[-\Delta\mathcal{U}]\}. & (2.54) \end{aligned}$$

The forward and reverse sampling probabilities are chosen to be normal distributions,

$$T(r_b \to r'_b) = (2\pi\sigma^2)^{D/2}\exp[-\frac{(r'_b - \bar{r})}{2\sigma^2}] \tag{2.55}$$

and

$$T(r_b' \to r_b) = (2\pi\sigma^2)^{D/2} \exp\left[-\frac{(r_b - \bar{r})}{2\sigma^2}\right] \tag{2.56}$$

where $\bar{r} \equiv \frac{1}{2}(r_{b-1} + r_{b+1})$. The change is kinetic action is given by

$$\begin{aligned} \Delta\mathcal{K} &= \mathcal{K}(r_{b-1}, r_b'; \tau) + \mathcal{K}(r_b, r_{b+1}'; \tau) + \mathcal{K}(r_{b-1}, r_b; \tau) + \mathcal{K}(r_b, r_{b+1}; \tau) & (2.57) \\ &= \frac{1}{2\lambda\tau}[(r_b' - \bar{r})^2 - (r_b - \bar{r})^2]. & (2.58) \end{aligned}$$

Thus we see that if we choose $\sigma = \sqrt{\lambda\tau}$, we sample the kinetic action exactly, i.e.

$$A(r_b \to r_b') = min\{1, \exp\left[-\Delta\mathcal{U}\right]\}. \tag{2.59}$$

For higher levels, the result is the same with $\tau \to \tau_l \equiv 2^{l-1}\tau$ and $\sigma \to \sigma_l \equiv \sqrt{\lambda\tau_l}$, where ℓ is the current bisection level with $l = 1$ being the lowest possible level. At each level of the bisection, the new bead position can be written as

$$r_b' = \frac{1}{2}(r_{b-2^{l-1}} + r_{b+2^{l-1}}) + \eta\sqrt{\sigma_l} \tag{2.60}$$

where η is a normally distributed random vector with unit variance and zero mean. In this way, the acceptance probability of the whole bisection move is the same as (2.59). There is a choice, however, of how this acceptance probability gets evaluated. Typically, we evaluate the change in potential action only at the lowest level after sampling only the kinetic action at every higher level as described. This leads to every higher level being accepted with probability 1. On the other hand, the change in potential action may also be used in every level's acceptance condition provided the final weight is still given by (2.59). Using this technique can lead to swifter convergence to the equilibrium distribution even though it can also be more computationally demanding.

2.3.3 Permutations

In order to explore the entire configuration space for systems with quantum statistics (e.g. bosons and fermions), it is necessary to also sample permutations of particles. In the path integral picture this amounts to having paths of length $n\beta$ that incorporate n particles with $1 \leq n \leq N$. The entire permutation space S_N consists of all possible combinations $\{n_1, n_2, \ldots, n_N\}$ such that $N = \sum_i n_i$.

To sample permutation space, we first choose a time slice b for an n-body permutation $\mathcal{P}$ to occur. We then use the bisection move to construct new paths for each of the involved n particles to their respective permuted points. For each particle i, a new path segment is created which begins at its own bead on time

slice $b-(2^L+1)$ and terminates at the bead belonging to particle $\mathcal{P}_i$ on time slice b. The entire move is accepted or rejected as a whole based on the final change in action.

There are several ways to propose possible permutations $\mathcal{P}$. Naively, one could simply iterate through all of S_N, however this has exponential growth with the number of particles N. This lack of efficiency is compounded since most of the proposed permutations would be rejected. A more intelligent sampling scheme must circumvent the exponential scaling as well as ignore unlikely possibilities.

To arrive at such an algorithm, we choose the transition probability for a L-level bisective permutation between particles i and j to be written as

$$T(R \to \mathcal{P}_{ij}R) = \mathcal{N}\frac{\exp\left[-\frac{(r'_j-r_i)^2}{\lambda\tau_L}\right]\exp\left[-\frac{(r'_i-r_j)^2}{\lambda\tau_L}\right]}{\exp\left[-\frac{(r'_i-r_i)^2}{\lambda\tau_L}\right]\exp\left[-\frac{(r'_j-r_j)^2}{\lambda\tau_L}\right]} \tag{2.61}$$

where $\mathcal{N}$ is a normalization constant, and r, r' are the bead coordinates at time slices $b-(2^L+1)$ and b, respectively. With this choice, the ratio of forward and reverse transition probabilities will again cancel the change in kinetic action. If we define

$$t_{ij} \equiv \frac{\exp\left[-\frac{(r'_j-r_i)^2}{\lambda\tau_L}\right]}{\exp\left[-\frac{(r'_i-r_i)^2}{\lambda\tau_L}\right]} \tag{2.62}$$

we may write $T(R \to \mathcal{P}_{ij}R) = \mathcal{N}t_{ij}t_{ji}$. Furthermore a three-particle permutation transition probability may be written $T(R \to \mathcal{P}_{ijk}R) = \mathcal{N}t_{ij}t_{jk}t_{ki}$. This result can generalize to any n-particle permutation. For computational convenience, however, we usually truncate at four-particle permutations. This makes the normalization constant

$$\mathcal{N} = \sum_i (t_{ii} + \sum_j t_{ij}(t_{ji} + \sum_k t_{jk}(t_{ki} + \sum_l t_{kl}t_{li}))) \tag{2.63}$$

where $t_{ii} = 1$. For N particles, calculating every possible four-particle permutation would then require the construction of a table of size $\mathcal{O}(N^4)$. However, this work can be much reduced by removing elements for which t_{ij} is small. A single element of the table is selected according to its respective probability. Once selected, the reverse table is constructed to compute the proper acceptance condition and normalization.

An alternative method for selecting a single permutation avoids the need to create such a large table without truncation at *four*-particle permutations [11]. First randomly select a single particle i and construct a table with entries

$$\tilde{t}_{ij} \equiv \exp\left[-\frac{(r'_j - r_i)^2}{\lambda\tau_L}\right]. \tag{2.64}$$

The move is then continued with probability

$$A_j = \frac{\sum_{j\neq i} \tilde{t}_{ij}}{\sum_j \tilde{t}_{ij}}. \tag{2.65}$$

If the acceptance test passes, an entry j is sampled from $\tilde{t}_{ij}$ with probability

$$T_j = \frac{\tilde{t}_{ij}(1-\delta_{ij})}{\sum_{j\neq i} \tilde{t}_{ij}}. \tag{2.66}$$

Next, a new table $\tilde{t}_{jk}$ is constructed in the same way as (2.64), and the move is continued with probability $A_k = \sum_{k\neq j} \tilde{t}_{jk} / \sum_k \tilde{t}_{jk}$ and, if accepted, a new particle k is chosen from the distribution $T_k = \tilde{t}_{jk}(1-\delta_{jk}) / \sum_{k\neq j} \tilde{t}_{jk}$. If it turns out that $k = i$, then the loop is closed and the permutation has been chosen. If not, the process continues, only now the acceptance condition becomes

$$A_l = \frac{\sum_{l\neq j,k} \tilde{t}_{kl}}{\sum_l \tilde{t}_{kl}}. \tag{2.67}$$

If this passes, a new particle l is chosen from the distribution

$$T_l = \frac{\tilde{t}_{kl}(1-\delta_{lj}-\delta_{lk})}{\sum_{l\neq j,k} \tilde{t}_{kl}} \tag{2.68}$$

where both particles that have already been included are chosen again with probability 0. This procedure is iterated until the loop has closed and the permutation has been chosen resulting in an $\mathcal{O}(N^3)$ algorithm.

The choice between the two described methods is directed by the system under study. For both methods, once the permutation has been chosen, a bisection is performed to construct the newly permuted paths. However, only in the first method can some of the cost of building the permutation table be ameliorated. This is accomplished by building the t_{ij} table for a fixed bisection range, and then attempting several permuting bisection moves in that range. For the second method, new tables must be constructed for each iteration. Thus, if long permutations are important, it may become useful to use the second method. However, in most cases the first method provides greater efficiency.

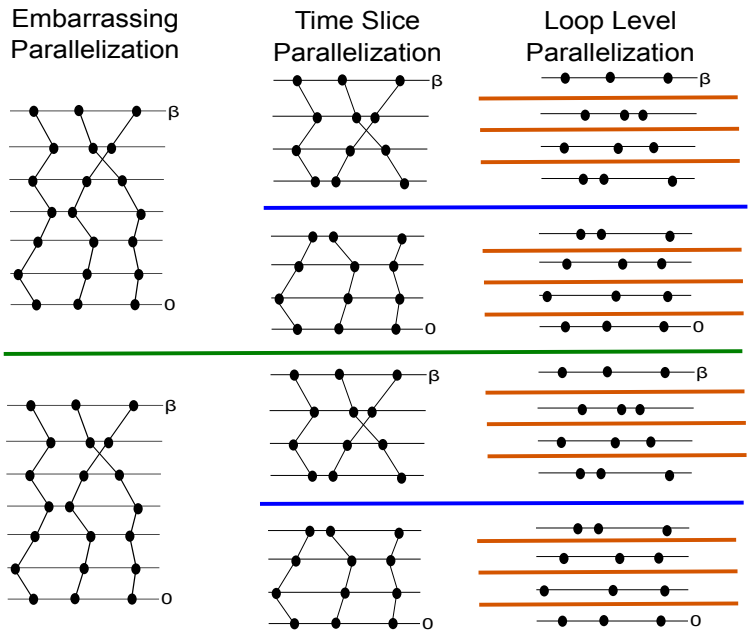

Figure 2.3: The three levels of parallelization possible for PIMC.

2.4 Implementation

2.4.1 Algorithm

With all the above pieces in place, the PIMC algorithm is relatively straight forward. Bisections and permutations are iteratively applied to diffuse the paths through configuration space, tallying observables along the way. Once it is believed that a statistically independent sample has been created, the summed observables are averaged and written to file. This *blocking* procedure avoids auto-correlation errors between configurations that are not statistically independent as well as limits the amount the disk is accessed. After a run is completed, statistical analysis is performed on the blocked data to produce averages and error bars for each observable. We refer the reader to Appendix B for the algorithm pseudocode.

2.4.2 Parallelization

Often times, we require a large number of time slices and/or are simulating a large number of particles, necessitating the use of massively parallel high-performance computers (HPC). To leverage the number of cores available on these machines, we take advantage of three types of parallelization.

At the base level, because PIMC simulations boil down to random sampling, we may perform many simultaneous simulations of the same system to improve statistical measures. This idea is often termed *embarrassing* parallelization since it scales trivially with the number of cores available. This is accomplished

using the Message Passing Interface (MPI) protocol which allows for simple parallelization onto different MPI processes with distributed memory architectures.

For very long paths, it is often advantageous to split up contiguous groups of time slices onto different MPI processes. On each process, the edge time slices are shared with its neighboring processes and remain fixed, while the middle time slices are free to diffuse. To maintain ergodicity, the entire path is periodically randomly shifted among the processes, so that the edge time slices change.

Finally we often break each MPI process into many threads through the OpenMP shared memory protocol. This allows loops over time slices to be trivially parallelized when the computation within the loop is independent for each time slice. Ideally the path is split into as many MPI processes as efficient bisecting diffusion allows. A single MPI process is then placed onto a single HPC node, and OpenMP is used to distribute the work of the MPI process onto the cores of the node. We show all three levels of parallelization schematically in Fig. 2.4.2.

Chapter 3

Restricted path integral Monte Carlo

In this chapter we focus on the simulation of Fermi systems with PIMC. From the definition of the Fermi density matrix, we quickly realize there is an issue with the alternating sign. We then define this *fermion sign problem* and its implications for measuring observables in simulation. Next we present a way of circumventing the sign problem while introducing a small, uncontrolled approximation, the *fixed-node approximation*. For reference, we present two simple systems where the density matrix is known exactly, and thus we may quantify the approximate solution. Finally, we discuss implementing the fixed-node approximation in PIMC simulations and its associated difficulties.

3.1 Fermion sign problem

Similarly to (2.12), we may write the many-body, quantum-statistical density matrix as

$$\rho_{B/F}(R, R'; \beta) = \frac{1}{N!} \sum_{\mathcal{P} \in \mathcal{S}_N} \sigma_{\mathcal{P}, B/F} \rho_D(R, \mathcal{P}R'; \beta) \tag{3.1}$$

$$= \frac{1}{N!} \sum_{\mathcal{P} \in \mathcal{S}_N} \sigma_{\mathcal{P}, B/F} \int dR_1 \dots dR_{M-1} \rho_D(R, R_1; \tau) \dots \rho_D(R_{M-1}, \mathcal{P}R'; \tau) \tag{3.2}$$

where once again the sum is over all possible permutations $\mathcal{P}$ belonging to the symmetric group $\mathcal{S}_N$ for N particles. The subscripts B, F, D signify that these are boson, fermion, and boltzmannon density matrices, respectively. The sign weight $\sigma_{\mathcal{P}}$ for each respective permutation depends on its constituent particle type. For bosons, all permutations contribute positive weight, making $\rho(R, R'; \beta)$ a real probability distribution. For fermions, however, only permutations with an even number of exchanges contribute positive weight, while those with an odd number of exchanges contribute negative weight. This presents an issue for simulation since Monte Carlo sampling requires an all positive probability distribution.

To make the sampling distribution positive again, PIMC simulations of fermions actually simulate the same bosonic system while explicitly tracking the sign weight of each measurement. This results in fermionic

observables of the form

$$\begin{aligned} \langle \hat{\mathcal{O}} \rangle_F &= Tr(\hat{\mathcal{O}}\rho_F)/Tr(\rho_F) && (3.3) \\ &= \frac{Tr(\hat{\mathcal{O}}\rho_F)/Tr(\rho_B)}{Tr(\rho_F)/Tr(\rho_B)} && (3.4) \\ &= \langle \hat{\mathcal{O}}_F \rangle_B / \langle \sigma_F \rangle_B && (3.5) \end{aligned}$$

where we now need to record both the signed observable $\hat{\mathcal{O}}_F$ and average sign weight σ_F while sampling from the bosonic distribution. The denominator of (3.5) can be rewritten as

$$\langle \sigma_F \rangle_B = \frac{\mathcal{Z}_F(\beta)}{\mathcal{Z}_B(\beta)} = \exp\left[-\beta(\mathcal{F}_F(\beta) - \mathcal{F}_B(\beta))\right] \tag{3.6}$$

where $\mathcal{F}$ is the many-body free energy. For N particles, the fermion free energy is always greater than the boson free energy. In fact, for non-interacting particles this becomes

$$\langle \sigma_F \rangle_{B,0} = \exp\left[-\frac{N^2}{V}(2\pi\lambda\beta)^{D/2}\right], \tag{3.7}$$

implying the average value of the sign decreases exponentially with decreased temperature and increased number of particles. In Fig. 3.1, we plot the average value of the sign for a system of free fermions versus temperature, showing the exponential decay. Since all observables measured in simulation must be normalized by $\langle \sigma \rangle$, there is a corresponding exponential increase in the variance of signed observables $\hat{\mathcal{O}}_F$, causing their precise calculation to be computationally intractable. This is the signature of the infamous fermion sign problem.

It is worth noting that at finite-temperature and finite number of particles, the average value of the sign is still non-zero. In zero-temperature QMC, there is what some call a *true* sign problem, in that the average value of the sign is precisely zero. Thus the PIMC sign problem is really more of a *sign issue*. Because of this, there are still some regimes where fermionic simulation is possible, as we shall see later. For now, however, we turn to the aforementioned workaround to what we will continue to call the fermion sign problem.

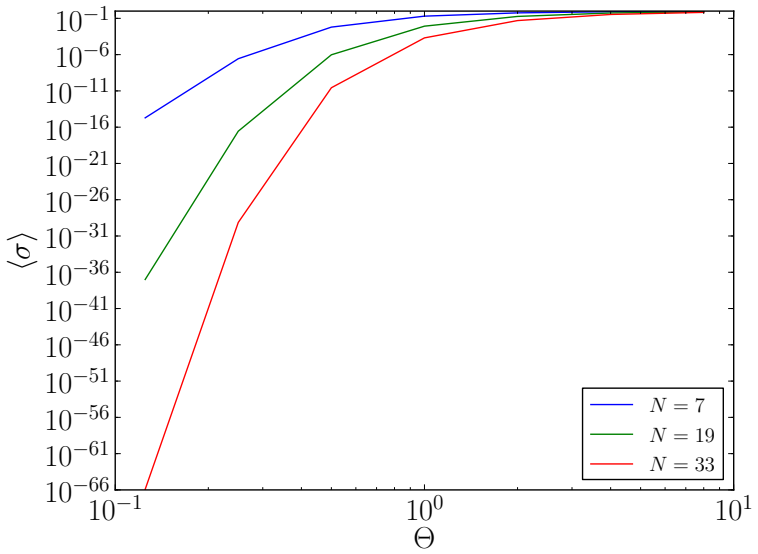

Figure 3.1: The average value of the sign $\langle\sigma\rangle$ for $N = 7$, 19, and 33 free fermions at several values of $\Theta \equiv T/T_F$. We see the exponential decay to zero with decreased temperature which is indicative of the sign problem mentioned in the text.

3.2 Fixed-node for path integrals

Recall from (2.2) that the many-body density matrix may also be defined as the solution to the Bloch equation. For fermions this takes the form

$$-\frac{d}{d\beta}\rho_F(R,R';\beta) = \hat{\mathcal{H}}\rho_F(R,R';\beta) \tag{3.8}$$

with the initial condition $\rho_F(R,R';0) = \hat{\mathcal{A}}\delta(R-R')$ where $\hat{\mathcal{A}}$ is the anti-symmetrization operator. The fixed-node method for path integrals, which is also called the *restricted path* or *constrained path* method, involves supplanting this initial condition with zero boundary conditions [25]. To show that this is a mathematically consistent operation, we must prove that the zero boundary condition solution both solves the Bloch equation and is unique.

Suppose we specify a *reference time slice* $R^\star$ such that $\rho_F(R,R^\star;0) = \hat{\mathcal{A}}\delta(R-R^\star)$. This defines a *nodal surface* for all $0 \le \tau \le \beta$,

$$\Upsilon(R^\star;\tau) \equiv \{R \mid \rho_F(R,R^\star;\tau) = 0\}, \tag{3.9}$$

which is a DN-dimensional manifold that divides the $(DN+1)$-dimensional configuration space into pockets of fixed sign. We may then solve the Bloch equation within each pocket by inserting an infinite potential barrier precisely along the nodal surface to enforce the zero boundary condition.

To prove uniqueness, we suppose there are two solutions to the Bloch equation $\rho_1(R,R^\star;\beta)$ and $\rho_2(R,R^\star;\beta)$

which both satisfy the zero boundary condition. We may then define a third function $\phi \equiv \rho_1 - \rho_2$ which clearly also solves the Bloch equation with the same boundary conditions,

$$0 \quad = \quad (\hat{\mathcal{H}} + \frac{d}{d\tau})\phi(R, R^\star; \tau). \tag{3.10}$$

Recalling that $\hat{\mathcal{H}} = -\lambda\nabla_R^2 + V(R)$, we can write

$$0 \quad = \quad \int_0^\beta d\tau \int dR e^{2V_0\tau}\phi(R, R^\star; \tau)(-\lambda\nabla_R^2 + V(R) + \frac{d}{d\tau})\phi(R, R^\star; \tau) \tag{3.11}$$

where V_0 is defined as a lower bound to the potential $V(R)$. Through a combination of Stoke's and Green's theorem combined with the zero boundary condition (see Appendix C), we arrive at

$$0 \quad = \quad \int dR \frac{e^{2V_0\beta}}{2}\phi(R, R^\star; \tau)^2 \tag{3.12}$$

$$+ \int dR \int_0^\beta d\tau \{(V(R) - V_0)e^{2V_0\tau}\phi(R, R^\star; \tau)^2 + e^{2V_0\tau}(\nabla_R\phi(R, R^\star; \tau))^2\}. \tag{3.13}$$

Since each term is positive, we immediately realize that $\phi(R, R^\star; \tau) = 0$ and thus $\rho_1 = \rho_2$. Therefore the zero boundary condition defines a unique solution to the Bloch equation, and the fixed-node method is mathematically consistent.

We may now define the *reach* as the set of all continuous paths $R_\tau \to R^\star$, for which $\rho(R_\tau, R_\star, \tau) \neq 0$, i.e. a node-avoiding path,

$$\Gamma(R^\star; \tau) = \{R_\tau \mid \rho(R, R^\star; \tau) \neq 0\}. \tag{3.14}$$

All paths contributing to the Bloch equation solution with zero boundaries belong to this set. Odd permutations must cross a node an odd number of times and thus are not allowed by this constraint. In fact, they are exactly canceled by all paths of node-crossing even permutations due to the tiling theorem proved in Appendix C. This leaves us with the following expression for the density matrix,

$$\rho_F(R, R^\star; \beta) = \frac{1}{N!}\sum_{\mathcal{P}, even} \int_{R_i \in \Gamma(R^\star;\tau)} dR_1 \ldots dR_{M-1}\rho_D(R, R_1; \tau)\ldots\rho_D(R_{M-1}, \mathcal{P}R^\star; \tau) \tag{3.15}$$

We have thus turned the sign-full expression for the density matrix into one which includes only terms of a single sign, making it a true probability distribution and allowing efficient Monte Carlo sampling. However, this all hinges on *a priori* knowledge of the density matrix nodal structure. In general, the nodes of the density matrix are not known or analytically solvable. To escape this self-consistency issue, a trial

density matrix is introduced which approximates the actual nodal structure. This ansatz is a solution to the Bloch equation inside the trial nodal cells and obeys the correct initial conditions, providing an exact solution only when its nodes are the true nodes of the density matrix. For N particles of a single fermion species, it is often simplest to write down the anti-symmetrized density matrix as the Slater determinant of single-particle distinguishable density matrices, $\rho(R, R^\star; \tau) = \frac{1}{N!} \det \rho_{ij^\star}(\tau)$. For multiple fermion species, the nodal constraint is taken as a product of such Slater determinants. In the next sections, we present two such ansatzes.

3.3 Free particle nodes

From (2.19) we know the free particle many-body density matrix can be written

$$\rho_0(R, R^\star; \tau) = (4\pi\lambda\tau)^{-D/2} e^{-\sum_i \frac{|r_i - r_i^\star|^2}{4\lambda\tau}}. \tag{3.16}$$

For free fermions this becomes

$$\begin{aligned} \rho_{0,F}(R, R^\star; \tau) &= \frac{1}{N!} \sum_{\mathcal{P}\in\mathcal{S}_\mathcal{N}} (4\pi\lambda\tau)^{-D/2} \exp\left[-\sum_i \frac{|r_i - \mathcal{P}r_i^\star|^2}{4\lambda\tau}\right] && (3.17) \\ &= \frac{1}{N!} \det\left[(4\pi\lambda\tau)^{-D/2} \exp\left(-\frac{|r_i - r_j^\star|^2}{4\lambda\tau}\right)\right] && (3.18) \end{aligned}$$

where the second equality is only true because there are no interactions. Our reach is then defined by when this determinant becomes zero. Thus in simulation we often drop the repeated cofactors, and define

$$\rho_{ij_\star} = \exp\left[-\frac{(r_i - r_{j\star})^2}{4\lambda\tau}\right]. \tag{3.19}$$

For two particles in open space, the condition that (3.18) is zero results in a hyperplane nodal surface $\Upsilon(r_1^\star, r_2^\star; \tau)$ defined by

$$(r_1 - r_2) \cdot (r_1^\star - r_2^\star) = 0. \tag{3.20}$$

which clearly holds at coincidence points ($r_1 = r_2$) and points of orthogonality ($r_{12} \perp r_{12}^\star$). For periodic boundary conditions and for more than two particles, the nodal surface is more complex, though some general rules still hold. The first, most obvious rule is that coincidence points still lie directly on the nodal surface. The second, less obvious rule is that free particle nodes maintain the maximal property in which the reach is divided into a single positive region and a single negative region. This has been shown analytically

for small clusters of particles and numerically for N particles [25].

Using a non-interacting nodal structure to constrain interacting systems is, on the surface, counterintuitive. Nevertheless, they have been surprisingly good in many simulations of several systems [14, 20, 80]. This is likely due to the fact that in the classical limit, free particle nodes become the exact nodal structure. Additionally the translational symmetry of the systems studies is reflected in the free particle nodal structure. Thus, generally we expect free particle nodes to be best when correlation effects are weak, at high temperature, and when the system obeys translational symmetry.

3.4 Harmonic nodes

Next we present the nodal structure for free particles in an external harmonic trap, at least in part because it is the only other exactly solvable many-body system, but also because it provides a convenient testbed for nodal improvements.

Recall that the harmonic potential may be written $V(r) = \frac{m\omega^2 r^2}{2}$. In the continuous path integral picture, this leads to a density matrix of the form

$$\begin{aligned} \rho(R,R';\beta) &= \int_R^{R'} dR_\tau \exp\left[-\mathcal{S}(R,R';\beta)\right] && (3.21) \\ &= (\frac{1}{4\pi\lambda\beta})^{ND/2} \int_R^{R'} dR_\tau \exp\left[-\int_0^\beta d\tau (\frac{\dot{R_\tau}^2}{4\lambda} + \frac{\omega^2 R_\tau^2}{4\lambda})\right] && (3.22) \end{aligned}$$

where R_τ is a continuous DN-dimensional variable between R and R'. To compute this integral, it is most straightforward to use the standard fluctuation expansion which makes use of the fact that the action decomposes into the sum of a classical and fluctuation part, such that

$$R_\tau = R_{cl,\tau} + \delta R_\tau. \tag{3.23}$$

It is clear that the classical piece obeys the equation of motion $\ddot{R}_{cl} = \omega^2 R_{cl}$ subject to the conditions $R_{cl,0} = R$ and $R_{cl,\beta} = R'$ such that $\delta R_0 = \delta R_\beta = 0$. Making the variable substitutions, we find

$$\mathcal{S}(R,R';\beta) = \int_0^\beta d\tau (\frac{\dot{R}_{cl,\tau}^2}{4\lambda} + \frac{\omega^2 R_{cl,\tau}^2}{4\lambda}) + \int_0^\beta d\tau (\frac{\delta\dot{R}_\tau^2}{4\lambda} + \frac{\omega^2 \delta R_\tau^2}{4\lambda}) \tag{3.24}$$

where the cross-terms are zero due to the listed identities. Thus we find that we can split the full density matrix into

$$\rho(R,R';\beta) = (\frac{1}{4\pi\lambda\beta})^{ND/2} e^{-\mathcal{S}_{cl}(R,R';\beta)} F_\omega(\beta), \tag{3.25}$$

where $\mathcal{S}_{cl}$ is the classical action and $F_\omega(\beta)$ is the fluctuation factor. Solving the classical equation of motion, we find its contribution to be

$$e^{-\mathcal{S}_{cl}(R,R';\beta)} = \exp\,[-\frac{\omega}{4\lambda\sinh\,(\beta\omega)}((R^2+R'^2)\cosh\,(\beta\omega)-2RR')]. \tag{3.26}$$

To solve for $F_\omega(\beta)$, we may transform the integral using Fourier components $\delta x_{i,d,\tau} = \sum_{n=1}^{\infty} c_{i,d,n} sin(\omega_{i,d,n}\tau)$ [64] such that

$$\begin{aligned} F_\omega(\beta) &= \int_R^{R'} dR_\tau \exp\,[-\int_0^\beta d\tau(\frac{\delta\dot{R}_\tau^2}{4\lambda}+\frac{\omega^2\delta R_\tau^2}{4\lambda})] &(3.27)\\ &= \prod_{i=1}^{N}\prod_{d=1}^{D}\prod_{n=1}^{\infty}\int_{-\infty}^{\infty} dc_{i,d,n}\frac{\beta\omega_{i,d,n}^2}{\sqrt{8\pi\lambda}}\exp\,[-\frac{\beta}{8\lambda}(\omega^2+\omega_{i,d,n}^2)c_{i,d,n}^2] &(3.28)\end{aligned}$$

where the first product is over particle number, the second over dimensions, and the third over Fourier coefficients. If we assume the harmonic frequency to be the same in all dimensions, i.e. $\omega_{i,d,n} = \omega_n = \pi n/\beta$, these Gaussian integrals are easily computed to be

$$\begin{aligned} F_\omega(\beta) &= \prod_{i=1}^{N}\prod_{d=1}^{D}\prod_{n=1}^{\infty}(\frac{\omega_n^2}{\omega^2+\omega_n^2})^{1/2} &(3.29)\\ &= \prod_{i=1}^{N}\prod_{d=1}^{D}(\prod_{n=1}^{\infty}1+\frac{\beta\omega^2}{\pi n^2})^{-1}. &(3.30)\end{aligned}$$

Finally, we recognize the product over n as a representation of $\sinh\,(\beta\omega)/(\beta\omega)$, thus

$$F_\omega(\beta) = (\frac{\beta\omega}{\sinh\,(\beta\omega)})^{ND/2}. \tag{3.31}$$

This makes our full density matrix

$$\rho(R,R';\beta) = (\frac{\omega}{4\pi\lambda\sinh\,(\beta\omega)})^{ND/2}\exp\,[-\frac{\omega}{4\lambda\sinh\,(\beta\omega)}((R^2+R'^2)\cosh\,(\beta\omega)-2RR')]. \tag{3.32}$$

As a sanity check, one can see that in the limit $\omega \to 0$, we return the free particle density matrix,

$$\rho(R,R';\beta) = (\frac{1}{4\pi\lambda\beta})^{ND/2}\exp\,[-\frac{1}{4\lambda\beta}(R-R')^2]. \tag{3.33}$$

Now to once again examine the two-particle nodal constraint, we take (3.32) as $\rho_{ij^\star}$ and compute the determinant. Not surprisingly we once again find the nodal surface to be represented by the equation $(r_1-r_2)\cdot(r_1^\star-r_2^\star)$. For more than two particles, however, harmonic nodes differ from those of free particles.

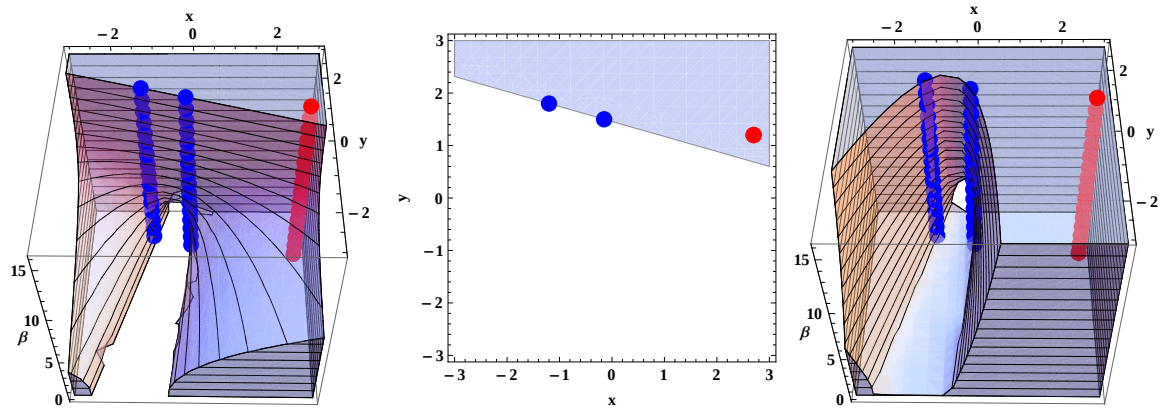

(a) (b) (c)

Figure 3.2: An example nodal surface for three particles in a two dimensional harmonic trap. Here all time slices occupy the same point in space, showing how the exact nodal structure (a) is the precise extrapolation from the ground state nodal structure (b) to those of free particles (c).

In Fig. 3.2 we plot three nodal surfaces for three particles in a two dimensional harmonic trap. Specifically we show the region of space that a single particle is allowed to move if the other two particles are fixed, for the exact nodal constraint, the ground state nodal constraint, and the free particle nodal constraint. We find, as expected, that the exact nodal constraint smoothly extrapolates to the free particle constraint at high temperature and to the ground state constraint at zero-temperature. The transition between the two appears to happen fairly rapidly, implying that if we know a system is in a high or low temperature regime, approximating its nodes with free or ground state nodes, respectively, should be accurate. Later on, we will present a method for quantifying this assertion, but for now we move on to the implementation of nodal constraints in PIMC simulations.

3.5 The fixed-node action in simulation

In order to enforce a nodal constraint within PIMC, the sign weight must be computed after every Monte Carlo step. If the sign ever becomes negative, that step is rejected. Typically we accomplish this in conjunction with the permuting bisection move by checking the sign on a configuration only after it has been accepted at every bisection level. This amounts to computing $\det[\rho_{ij^\star}]$ for every time slice involved in the bisection move. If the every determinant is positive, the move is accepted, otherwise it rejected. If the reference slice is part of the bisective move, then the check must be done for every time slice along the path.

There are a couple tricks that help with this process. First, the determinant is an $\mathcal{O}(N^3)$ operation. It was shown previously that this can be improved with smart updating techniques [19, 28]. Second, if we

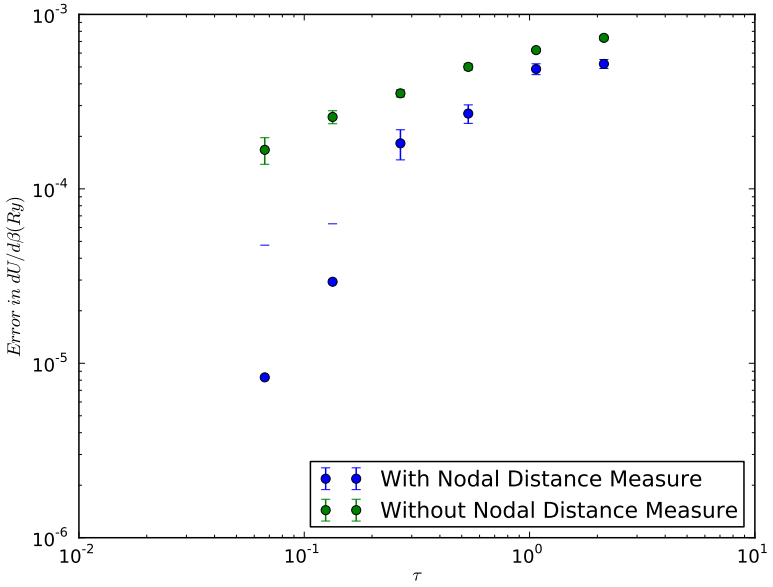

Figure 3.3: Average error in the total energy with time step for two different nodal actions applied to a system of 33 electrons at a density of $r_s = 1.0$ and temperature $T/T_F = 1.0$. Using a nodal distance measure (blue points) as in (3.37) converges quicker than using the nodal primitive approximation (green points).

redefine how we measure time differences in the restriction to be,

$$\tau_r = \begin{cases} \tau, & \text{if } 0 \leq \tau \leq \beta/2 \\ \beta - \tau, & \text{if } \beta/2 \leq \tau \leq \beta \end{cases}, \tag{3.34}$$

we can use two reference slices [24]. In other words we compute the simple convolution

$$\rho(R, R'; \beta) = \int dR^\star \rho(R, R^\star, \beta/2)\rho(R^\star, R'; \beta/2) \tag{3.35}$$

in order to double the temperature of the nodal restriction. The hope is that this allows the use of free particle nodes down to lower temperatures.

If we think of the nodal surface as an infinite potential,

$$V_N = \begin{cases} 0, & \text{if } \det\left[\rho_{ij^\star}\right] > 0 \\ \infty, & \text{if } \det\left[\rho_{ij^\star}\right] < 0 \end{cases}, \tag{3.36}$$

the algorithm outlined above is tantamount to treating this potential with the primitive approximation. As stated previously, this approximation comes with a time step error. Here, the error arises from paths that

cross and recross the nodal surface in a time smaller than the time step. Also as before, the time step error can be improved by using a higher order approximation for the nodal action.

Using the method of images, the exact nodal action for a single particle in a $1D$ box of length L can be shown to be,

$$\mathcal{U}_N(x,x';\tau) = -\sum_{n,n'=0}^{\infty} \ln\left[1-\exp\left(-\frac{(d+nL)(d'+n'L)}{\lambda\tau}\right)\right] \tag{3.37}$$

where d is the distance to the node of $\rho(x,x';\tau) - \rho(x,x';\tau)$, and the sum is over periodic images of the box. In a many-body system in higher dimension, if we assume the nodal surface locally approximates a hard wall, without curvature, we can use this same form for the nodal action. Clearly this must be true as the nodal distance becomes small and a particle approaches the nodal surface. In fact, this is precisely where the nodal action starts to play a role and should suffice to prevent cross-recross type errors. What is left then is how to accurately calculate the distance to the nodal surface for a many-body system, for which there exist several options.

The most obvious estimate of the nodal distance is simply the nearest distance to the coincidence point of two particles. This provides an upper bound on the minimum distance, $d(r_i,r_j) \leq r_{ij}/\sqrt{2}$, though generally it may be smaller. For a more precise estimate, one can use the Newton-Raphson method which gives the distance to the nearest node as,

$$d(R,R^\star) = \frac{|\det[\rho_{ij^\star}]|}{|\nabla \det[\rho_{ij^\star}]|}. \tag{3.38}$$

This procedure can be repeated several times until the level of desired precision is reached. Another alternative is to conduct a simple line search in the direction of the gradient of $\det[\rho_{ij^\star}]$.

Both these more precise methods, beyond the single iteration Newton-Raphson, can become computationally intensive, so it is desirable to limit their use. On the other hand if the estimated nodal distance is wildly different from its true value, it runs the risk of biasing the simulation. With this in mind, we typically use a hybrid approach where we first use the single iteration Newton-Raphson method to estimate the distance to the nearest node, $d(R,R^\star)_1$. If this distance is more than an order of magnitude larger than the thermal DeBroglie wavelength, $\lambda\tau$, we assume the node likely is not playing much of a role and use

$$d(R,R^\star) \equiv \min\left(d(R,R^\star)_1, \min_{i,j}(r_{ij}/\sqrt{2})\right) \tag{3.39}$$

as the estimate. If this distance is on the order of or smaller than DeBroglie wavelength, we then employ either more Newton-Raphson iterations or the $1D$ line search until a desired precision is achieved. In this way we balance both efficiency and accuracy. Typically checking the distance to the nodes is the most

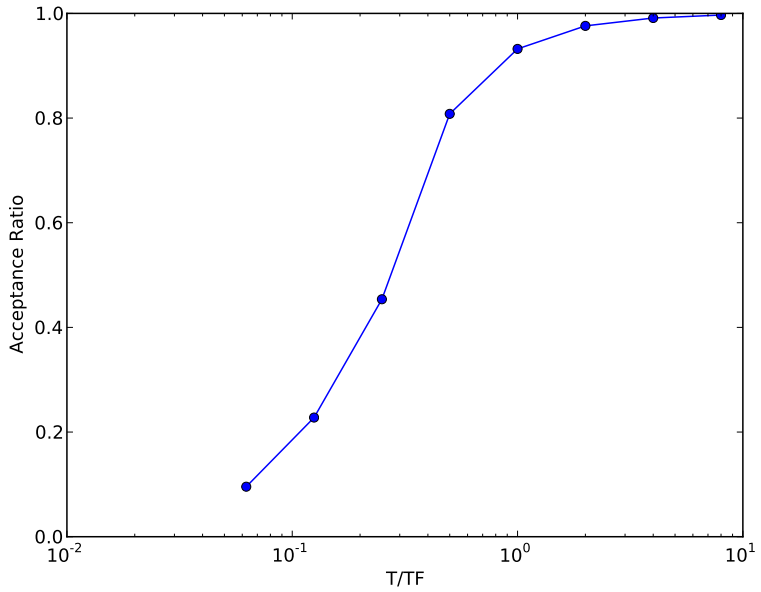

Figure 3.4: The average acceptance ratio for an $L = 3$ level bisective move for a system of 33 electrons at a density of $r_s = 1.0$ for various temperatures. Here T_F is the Fermi temperature. As the temperature is lowered the acceptance ratio decays to zero due to reference point freezing.

time consuming step in the PIMC method because of the repeated determinant calculations, thus high-order approximations are only added on an as-needed basis. In Fig. 3.3 we plot a comparison between the primitive nodal action and that of (3.37). It is clear that the latter converges much faster with decreased time step, though both eventually converge to the same result. The total efficiency of convergence, computer time divided by error, must be considered to decide which route is preferable.

3.6 Reference point freezing

Generally there are two options to translate the reference slice itself: simply include it as part of a bisective move or switch which time slice is defined as the reference. For either method, every time the reference slice itself is translated, the nodal constraint must be checked on every time slice. For long paths, i.e. lower temperatures, it is not difficult to see how this may become an issue. On or near the reference slice, the nodal surface is free particle-like. However, as β increases, the character of the nodal surface far away from the reference slice can change dramatically, as shown in Fig. 3.2. Consequently small shifts in the position of a particle on the reference slice can amount to large shifts of the nodal surface far away. This effect causes the reference slice to become frozen in configuration space as most proposed moves are rejected.

In Fig. 3.4, we plot the effect of reference point freezing for a system of electrons at various temperatures.

For an $L = 3$ level bisective move for different temperatures, the acceptance rate quickly decays to zero. The same effect can be shown for moves that simply relabel which time slice is the reference. To overcome this issue and perform the integral over $R^\star$, we were required to run thousands of clones at the same temperature, each starting from a different equilibrated configuration. Generally, however, reference point freezing remains a problem, particularly for low temperature and high density systems.

Chapter 4

Density Functional Theory

At present, the method of choice for treating electrons at finite-temperatures is density functional theory (DFT). This method has been used ubiquitously to simulate a diverse set of chemical systems at zero-temperature [66]. The success of DFT in such systems has led many to believe its usefulness should extend to finite-temperature, specifically to warm dense matter (WDM). However in practice its finite-temperature formulation is ad hoc and has uncontrolled approximations. In this chapter we review both the zero and finite-temperature formalisms of DFT followed by a discussion of its use in the simulation of WDM systems.

4.1 Zero-temperature density functional theory

4.1.1 Hohenberg-Kohn formulation

In 1964, DFT was first made possible by Hohenberg and Kohn by proving two clever theorems [53]. We begin with a derivation of both of these theorems, and then transition into the full zero-temperature DFT formulation.

The first theorem stated that for any system of N particles in an external potential V_{ext}, the single-particle ground state density $n_0(r)$ is uniquely determined. Assuming there are two potentials, $V_{ext}^{(1)}$ and $V_{ext}^{(2)}$, that differ than more than a constant that give the same density, $n_0(r)$. Because both of these potentials belong to the distinct Hamiltonians, $\mathcal{H}^{(1)}$ and $\mathcal{H}^{(2)}$, they also correspond to distinct ground state wavefunctions, $\Psi_{ext}^{(1)}(r)$ and $\Psi_{ext}^{(2)}(r)$.

We can now write the ground state energy as

$$E^{(1)} = \langle \Psi^{(1)} \mid \mathcal{H}^{(1)} \mid \Psi^{(1)} \rangle. \tag{4.1}$$

Assuming the ground state is non-degenerate, the variational principle holds such that

$$E^{(1)} < \langle \Psi^{(2)} \mid \mathcal{H}^{(1)} \mid \Psi^{(2)} \rangle. \tag{4.2}$$

Likewise, because both potentials produce the same equilibrium density, we know that

$$\langle \Psi^{(1)} \mid \mathcal{H}^{(1)} \mid \Psi^{(1)} \rangle = \langle \Psi^{(1)} \mid \mathcal{H}^{(2)} \mid \Psi^{(1)} \rangle - \int dr (V_{ext}^{(1)}(r) - V_{ext}^{(2)}(r)) n_0(r) \tag{4.3}$$

The indices may be trivially swapped giving

$$\langle \Psi^{(2)} \mid \mathcal{H}^{(2)} \mid \Psi^{(2)} \rangle = \langle \Psi^{(2)} \mid \mathcal{H}^{(1)} \mid \Psi^{(2)} \rangle + \int dr (V_{ext}^{(1)}(r) - V_{ext}^{(2)}(r)) n_0(r). \tag{4.4}$$

Adding these two equations together we find that

$$E^{(1)} + E^{(2)} < E^{(1)} + E^{(2)} \tag{4.5}$$

which is a contradiction. Therefore V_{ext} is unique via proof by *reductio ad absurdum*, and thus the ground state density is uniquely determined.

The second theorem states that the energy may be written as a universal functional of density, $E_V[n]$, and the exact ground state density gives the minimum of this functional. From the first theorem, we know that the external potential is uniquely specified by the density. Likewise, since the functional forms of the kinetic term T and internal potential term U are the same for all systems, the ground state wavefunction is also a unique functional of the density. This implies we may write the total energy as a functional of the density,

$$\begin{aligned} E_V[n] &= \int dr V_{ext}(r) n(r) + \langle \Psi[n] \mid T + U \mid \Psi[n] \rangle & (4.6) \\ &\equiv V[n] + F[n] & (4.7) \end{aligned}$$

where we have defined an external potential functional, $V[n] \equiv \int dr V_{ext}(r) n(r)$, and a universal functional of the kinetic and interacting contributions, $F[n] \equiv \langle \Psi[n] \mid T + U \mid \Psi[n] \rangle$. By inspection, we find that the exact ground state density gives the exact ground state energy, i.e. $E_V[n_0] = E_0$.

To show that $E_V[n]$ assumes its minimum at the exact ground state density, we once again utilize the variational principle. Given the unique ground state density $n_0(r)$, the ground state energy may be written

$$E_0 = E[n_0] = \langle \Psi_0 \mid \mathcal{H} \mid \Psi_0 \rangle \tag{4.8}$$

where Ψ_0 is the ground state wavefunction uniquely determined by the ground state density. Then due to

the variational principle, we know that for another density $n'(r)$,

$$E[n'] = \langle \Psi' \mid \mathcal{H} \mid \Psi' \rangle > \langle \Psi_0 \mid \mathcal{H} \mid \Psi_0 \rangle = E[n_0] \tag{4.9}$$

where Ψ' is the wavefunction uniquely determined by this density. Therefore $n_0(r)$ provides the unique minimum for the ground state energy functional.

With these two theorems, Hohenberg and Kohn proved that there is a one-to-one correspondence between the ground state density and an external potential, paving the way for straight-forward calculation of the ground state energy. One catch, however, is that minimizing the energy functional requires each density explored during the minimization process to correspond to a real, smooth external potential, a property called V-representability. This is not generally true. Nevertheless, if we write

$$F[n] = \min_{\Psi \to n} \langle \Psi[n] \mid T + U \mid \Psi[n] \rangle \tag{4.10}$$

where the minimization is constrained to N particle anti-symmetric functions, the density maintains a property called N-representability. Lieb and Levy showed the variational principle still holds provided this weaker constraint [73, 74].

Finally, for Coulomb potential systems, it is often useful to separate out terms such that

$$E_V[n] \quad = \quad V[n] + T_s[n] + U_H[n] + E_{xc}[n] \tag{4.11}$$

where $T_s[n]$ is the kinetic energy functional for a system of non-interacting particles at density $n(r)$, $U_H[n]$ is the classical Hartree interacting potential,

$$U_H[n] = \frac{1}{2} \int dr \int dr' \frac{n(r)n(r')}{|r - r'|}, \tag{4.12}$$

and $E_{xc}[n]$ is called the *exchange-correlation* functional. Essentially everything unknown was moved to this final term, defining it as

$$E_{xc}[n] = (T[n] - T_s[n]) + (\frac{1}{2} \int dr \int dr' \frac{n(r, r')}{|r - r'|} - U_H[n]) \tag{4.13}$$

where $n(r, r')$ is the two-body correlation function.

Two pieces remain to creation of a full DFT computational method: A choice must be made on how to compute each known term in (4.11), and we must find a method to approximate the generally unknown

exchange-correlation functional.

4.1.2 Kohn-Sham orbitals

Most often a formalism developed by Kohn and Sham is used [67]. There we define the energy functional,

$$E_V[n] = V[n] + T_s[\{\phi_i[n]\}] + U_H[n] + E_{xc}[n] \tag{4.14}$$

where we have introduced the full set of occupied orbitals $\{\phi_i[n]\}$ which reproduces the density by,

$$n(r) = \sum_i^N |\phi_i(r)|^2. \tag{4.15}$$

Now, the non-interacting contribution to the kinetic operator is written as a sum over Kohn-Sham orbitals

$$T_s[\{\phi_i[n]\}] = -\frac{\hbar^2}{2m}\sum_i^N \int dr \phi_i^\dagger(r)\nabla^2\phi_i(r). \tag{4.16}$$

We may now minimize the energy by taking a functional derivative with respect to the orbital set,

$$\begin{aligned}
\frac{\delta E[n]}{\delta\phi_i^\star(r)} &= \frac{\delta T_s[\{\phi_i[n]\}]}{\delta\phi_i^\star(r)} + [\frac{\delta V[n]}{\delta n(r)} + \frac{\delta U_H[n]}{\delta n(r)} + \frac{\delta E_{xc}[n]}{\delta n(r)}]\frac{\delta n(r)}{\delta\phi_i^\star(r)} && (4.17)\\
&= \frac{\delta T_s[\{\phi_i[n]\}]}{\delta\phi_i^\star(r)} + [V_{ext}(r) + V_H(r) + V_{xc}(r)]\phi_i(r) && (4.18)\\
&= \epsilon_i\phi_i(r) && (4.19)
\end{aligned}$$

where $V_H(r) = q^2\int dr' \frac{n(r')}{|r-r'|}$ is simply the Hartree potential, and V_{xc} is calculated directly from E_{xc}. If we now define,

$$V_s(r) \equiv V_{ext}(r) + V_H(r) + V_{xc}(r) \tag{4.20}$$

we arrive upon a single-body auxiliary Schrödinger equation,

$$[-\frac{\hbar^2}{2m}\nabla^2 + V_s(r)]\phi_i(r) = \tau_i\phi_i(r) \tag{4.21}$$

which yields orbitals that reproduce the density $n(r)$ of the original system.

The above are together considered the Kohn-Sham equations. Effectively they have replaced the problem of minimizing the energy functional with the problem of solving N non-interacting Schrödinger equations. The normal procedure is to first start with an initial guess for $n(r)$, calculate the corresponding $V_s(r)$, solve

for the set of occupied orbitals $\{\phi_i(r)\}$, and finally form a new $n(r)$. This process is repeated until the desired level of convergence is achieved. It is important to note that the eigenvalues given by solving the Kohm-Sham equations are not the system's single particle energies, though in certain situations they can provide a reasonable approximation to band structure and binding energies [68].

The final component of this scheme is the exchange-correlation potential V_{xc}, which contains all many-body aspects of the problem. The exchange-correlation energy functional is often broken into exchange and correlation contributions, $E_{xc} = E_x + E_c$. The exchange functional may be written down exactly as,

$$E_x[\{\phi_i[n]\}] = -\frac{1}{2}\sum_{jk}\int dr \int dr' \frac{\phi_j^\dagger(r)\phi_k^\dagger(r')\phi_j(r')\phi_k(r)}{|r-r'|}, \tag{4.22}$$

though no such exact form exists for E_c. The simplest approximation for this quantity comes from the local density approximation (LDA) [88]. In the LDA, one assumes the actual inhomogeneous system (with density $n(r)$ in potential $V_s(r)$) to be decomposed into infinitesimal cells in which the quantities $n(r)$ and $V_s(r)$ are taken to be constant. This allows one to write,

$$E_c[n] \approx \int dr n(r) e_c^{hom}[n(r)]. \tag{4.23}$$

where $e_c^{hom}[n(r)]$ is the per particle correlation energy of the homogeneous electron gas at density $n(r)$. For a homogeneous electron liquid, the form of $e_x^{hom}[n]$ is again exactly known. On the other hand, $e_c^{hom}[n]$ is more complicated to compute analytically. Instead, most often estimates of $e_c^{hom}[n]$ come from precise, zero-temperature quantum Monte Carlo (QMC) calculations [22]. Both analytic and numeric methods for calculating the correlation energy are discussed in detail in Chapter 5.

There exist extensions beyond the LDA, including the generalized gradient approximation (GGA) which incorporates the effects of fluctuations in the density, the inclusion of spin degrees of freedom, exact exchange functionals, and the relaxation of the LDA to nonlocal integral-dependent density functionals [68]. It should be noted, however, that all the mentioned methods still rely heavily on the numerical results of QMC.

4.1.3 Orbital free density functional theory

An alternative method, though less used, keeps the kinetic term, $T_s[n]$, as an explicit functional of the density instead of introducing an orbital basis. To do so, however, an approximation must be made. If we assume the density is a slowly varying function in space, the Thomas-Fermi approximation provides a viable candidate. This amounts to using the free gas form for the kinetic energy functional, effectively ignoring

kinetic exchange and correlation effects, i.e.

$$T[n] \approx \frac{DN}{10} k_F^2(n) n \tag{4.24}$$

where k_F is the Fermi momentum. Analytic gradient corrections can be added, equivalent to the GGA for the exchange-correlation energy [58]. However, even these corrected models have been shown to incur serious errors when simulating correlated systems, and fail to reproduce the accuracy of the Kohn-Sham formulation [60].

4.2 Finite-Temperature DFT

4.2.1 Mermin formulation

Only a year after publication, Hohenberg and Kohn's proof was extended to finite-temperatures by Mermin [78]. To do so, first notice the grand canonical potential,

$$\Omega = -\frac{1}{\beta} \ln \operatorname{Tr} e^{-\beta(\mathcal{H}-\mu N)}, \tag{4.25}$$

may be written as a functional of a density matrix as,

$$\Omega[\rho] = \operatorname{Tr} [\rho(\mathcal{H} - \mu N + \frac{1}{\beta} \ln \rho)], \tag{4.26}$$

and is subject to the variational principle

$$\Omega[\rho] > \Omega[\rho_0] \text{ if } \rho \neq \rho_0 \tag{4.27}$$

where

$$\rho_0 = \frac{e^{\beta(\mathcal{H}-\mu N)}}{\operatorname{Tr} e^{\beta(\mathcal{H}-\mu N)}}. \tag{4.28}$$

To extend the first Hohenberg-Kohn theorem at finite-temperature, we must assume once again there are two external potentials, $V_{ext}^{(1)}$ and $V_{ext}^{(2)}$, that correspond to the same equilibrium density, $n_0(r) = \operatorname{Tr} \rho_0^{(i)} \Psi^{\dagger(i)} \Psi^{(i)}$, $i = 1, 2$. From (4.26), we can write,

$$\Omega[\rho_0^{(1)}] = \operatorname{Tr} [\rho_0^{(1)} (\mathcal{H}^{(1)} - \mu N + \frac{1}{\beta} \ln \rho_0^{(1)})]. \tag{4.29}$$

Using the variational principle, we know

$$\begin{aligned} \Omega[\rho_0^{(1)}] &< \mathrm{Tr}\,[\rho_0^{(2)}(\mathcal{H}^{(1)} - \mu N + \frac{1}{\beta}\ln\rho_0^{(2)})] && (4.30) \\ &= \Omega[\rho_0^{(2)}] + \mathrm{Tr}\,[\rho_0^{(2)}(V_{ext}^{(2)} - V_{ext}^{(1)})]. && (4.31) \end{aligned}$$

As in the zero-temperature derivation, we can once again switch the indices and add the two equations together to find,

$$\Omega[\rho_0^{(1)}] + \Omega[\rho_0^{(2)}] < \Omega[\rho_0^{(1)}] + \Omega[\rho_0^{(2)}], \tag{4.32}$$

proving only a single $V_{ext}(r)$ can result in a given density matrix $\rho_0(r)$. Furthermore, because by definition $\rho_0(r)$ uniquely determines the density, $n_0(r)$, we know that $V_{ext}(r)$ uniquely determines $n_0(r)$ as was the case at zero-temperature.

Because of this fact, (4.26) can be written purely as a functional of the density,

$$\Omega[n;\beta] = \int dr(V_{ext}(r) - \mu)n(r) + F[n;\beta], \tag{4.33}$$

where we have defined the finite-temperature universal functional $F[n;\beta]$ and have explicitly denoted which functions depend on temperature. Clearly at the equilibrium density, $\Omega[n_0;\beta]$ becomes the equilibrium grand potential. The fact that this density minimizes the grand potential functional follows again from the variational principle. As before, the Lieb-Levy N-representability property can be applied, making the universal functional,

$$\begin{aligned} F[n;\beta] &= \min_{\rho\to n} \mathrm{Tr}\,[\rho(T + U + \frac{1}{\beta}\ln\rho)] && (4.34) \\ &\equiv T[n;\beta] + U[n;\beta] - \frac{1}{\beta}S[n;\beta] && (4.35) \end{aligned}$$

where we have defined $S[n;\beta]$ as the finite-temperature entropy functional of the density.

Once again for Coulomb systems, it is typical to separate terms. It is convenient to use a similar form as in the zero-temperature case,

$$\Omega[n;\beta] = V[n;\beta] + F_s[n;\beta] + U_H[n;\beta] + F_{xc}[n;\beta] \tag{4.36}$$

where we have defined

$$F_s[n;\beta] \equiv T_s[n;\beta] - \frac{1}{\beta}S_s[n;\beta] \tag{4.37}$$

as the non-interacting free energy and

$$F_{xc}[n;\beta] \equiv (T[n;\beta] - T_s[n;\beta]) + (U[n;\beta] - U_H[n;\beta]) - \frac{1}{\beta}(S[n;\beta] - S_s[n;\beta]) \tag{4.38}$$

as the exchange-correlation free energy.

4.2.2 Kohn-Sham at finite-temperature

To apply the Kohm-Sham method at finite-temperature, we once again introduce a set of orbitals that reproduce the density. The only difference is that when composing the density from the orbitals, the states are weighted by a temperature dependent function

$$n(r;\beta) \quad = \quad \sum_i \rho_i(\beta) f_i^\dagger(r)\phi_i(r). \tag{4.39}$$

For a non-interacting system f_i is simply the Fermi function, i.e. $f_i(\beta) = 1/(e^{\beta(\epsilon_i - \mu)} + 1)$ [37].

In the Kohn-Sham framework, the finite-temperature versions of the noninteracting kinetic and entropy functionals are

$$T_s[n;\beta] = -\frac{\hbar^2}{2m}\sum_i^N \int dr f_i(\beta)\phi_i^\dagger(r)\nabla^2\phi_i(r) \tag{4.40}$$

and

$$S_s[n;\beta] = -\sum_i [f_i(\beta)\ln f_i(\beta) + (1 - f_i(\beta))\ln(1 - f_i(\beta))], \tag{4.41}$$

respectively [37]. The classical Hartree potential becomes

$$U_H[n;\beta] = \frac{1}{2}\int dr \int dr' \frac{n(r;\beta)n(r';\beta)}{|r - r'|}, \tag{4.42}$$

and if $F_{xc}[n;\beta]$ is broken into exchange and correlation parts, the finite-temperature exchange is written

$$F_x[n;\beta] = -\frac{1}{2}\sum_{ij} f_i(\beta)f_j(\beta)\int dr \int dr' \frac{\phi_i^\dagger(r)\phi_j^\dagger(r')\phi_i(r')\phi_j(r)}{|r - r'|}. \tag{4.43}$$

Once again the final missing piece is the correlation functional, defined as $F_c[n;\beta] \equiv F_{xc}[n;\beta] - F_x[n;\beta]$, and once again approximations of its form must be made. In modern Kohn-Sham, finite-temperature DFT calculations, it is assumed that

$$F_c[n;\beta] \approx E_c[n(r;\beta)], \tag{4.44}$$

i.e. that the functional form is the same for finite-temperatures as it is at zero-temperature, only implicitly including temperature dependence through the occupation of orbitals composing the density. While this may be true for the Hartree energy $U_H[n;\beta]$, there is no reason to expect it hold for an arbitrary correlated system. Additionally, this approximation effectively sets the difference between the interacting and noninteracting entropy to zero, which is in general not true. The issue would seem to be especially dire in the warm-dense matter regime, where temperature and entropic effects become important. Nevertheless, this effective zero-temperature Kohn-Sham formalism is used regularly to study WDM systems. In Chapter 5, we test the validity of this approximation when applied to the homogeneous electron gas. In Chapter 6, we create a new explicitly finite-temperature functional to use in its place, and explore its application to several warm-dense systems.

There is a second, more technical, issue with the Kohn-Sham approach at finite-temperature. As temperature increases, an ever-increasing number of orbitals will be required to construct larger ensembles of states, making calculations computationally expensive. More concretely, a $T = 0$ Kohn-Sham DFT calculation scales as $\mathcal{O}(N_e^3)$, where N_e is the number of electrons in the simulation. At finite-temperature, this scaling changes to $\mathcal{O}(N_b^3)$, where N_b is the number of thermally occupied levels and $N_b \gg N_e$. Due to the nature of the Fermi function $\rho_i(\beta)$, N_b grows exponentially with increased temperature. This makes Kohn-Sham DFT calculations much beyond the Fermi temperature to be computationally intractable.

4.2.3 Orbital free at finite-temperature

In response to exponential blowup of required orbitals, there has been recent attention on finite-temperature orbital free methods. The Kohn-Sham orbitals are replaced by explicit functionals of the density, as in zero-temperature OFDFT, resulting in an $\mathcal{O}(N_e)$ simulation. Once again, however, an a priori way to determine such functionals has yet to materialize.

Recent efforts have extended the finite-temperature kinetic energy functional much beyond the Thomas-Fermi approximation to an accuracy approaching that of Kohn-Sham [58, 60, 104]. The exchange-correlation free energy is also replaced by a single functional which at the LDA level can be written

$$F_{xc}[n;\beta] = \int dr f_{xc}[n(r;\beta);\beta] \tag{4.45}$$

$$\approx \int dr f_{xc}^{hom}[n(r;\beta;\beta)]. \tag{4.46}$$

Several forms for $f_{xc}^{hom}[n;\beta]$ are presented in Chapter 5 and tested in Chapter 6.

Chapter 5

Homogeneous electron gas

> *. . . we have in the cathode rays matter in a new state, a state in which the subdivision of matter is carried very much further than in the ordinary gaseous state: a state in which all matter that is, matter derived from different sources such as hydrogen, oxygen, etc. is of one and the same kind; this matter being the substance from which the chemical elements are built up.*
>
> *J. J. Thomson, 1897*

Discovered by J. J. Thomson in 1897, the electron was the first elementary particle to be clearly identified [102]. Almost three decades later, Pauli, Fermi, and Dirac were able to describe it as a spin-1/2 quantum mechanical object, leading to several physical insights [33, 40, 87]. First and foremost, the Pauli exclusion principle, in which indistinguishable electrons are disallowed from occupying the same quantum state, led to a consistent picture of the structure and stability of the atoms that compose our world. Shortly after, Bloch and Wigner countered this individualistic picture by predicting the emergent ordered, many-body structures of the ferromagnet and Wigner crystal [9, 108]. Such phases were shown to be manifest only through the collective interactions of many electrons. It was at this point that the homogeneous electron gas (HEG), a translationally invariant system of only electrons, grew to prominence.

In the 1950's, Landau, followed by Bohm, Pines, Nozieres, and Anderson, completely redirected condensed matter physics by developing a picture of the HEG in which its low temperature properties were governed by the elementary excitations supported by a given phase [4, 10, 71, 84]. At intermediate densities exists Landau's famous Fermi liquid phase, where the low temperature excitations, dubbed *quasiparticles*, are effectively non-interacting particles. Fermi liquid theory has been widely successful in describing simple metals and semiconductors because many materials behave qualitatively similar to an intermediate density HEG. Correspondingly there has since been an intense interest in discovering where Fermi liquid theory breaks down. Some early searches looked at the low density phases predicted by Bloch and Wigner, where the relative interaction strength is large compared to the kinetic energy of the electron. It was found that for the ferromagnet, the quasiparticles turned out to be spin waves, while for the Wigner crystal, they are quantized lattice vibrations, also known as phonons [86]. Around the same time, Bardeen, Cooper, and

Schrieffer produced a working theory of superconductivity in which a phonon mediated electronic interaction forces the quasiparticles to form pairs of opposite momentum electrons [7]. This landmark result sparked a fresh interest in the nature of strongly correlated electrons that has continued to present time. Along the way systems with constrained geometry and/or strong magnetic fields have been discovered to exhibit other exotic phases such as integer quantum Hall, fractional quantum Hall, Luttinger liquids, heavy fermions, and high-temperature superconductivity [50, 85].

Simultaneously, Hohenberg, Kohn, and Sham's development of density functional theory (DFT) revolutionized the field of quantum chemistry and biology [53, 67].[1] Its reliance on precise estimates of the HEG's correlation energy led to Ceperley and Alder's use of zero-temperature quantum Monte Carlo (QMC), which in 1980 gave the first exact ground state energies for select phases [22]. Since that time, QMC has become the de facto method of choice for accurate, thermodynamic limit information of the electron gas, leading to higher and higher fidelity determination of its phases [54, 69, 101, 110]. At every step, DFT has improved concurrently, both with the inclusion of more precise HEG correlation energies, as well as the introduction of more refined density functionals [89].

All the work mentioned thus far was focused on the zero or low temperature behavior of the HEG. During the same period, however, an almost independent set of researchers were focused on studying essentially the same system at high temperatures [31, 52]. They named their system the one-component plasma (OCP) since it consists of completely ionized atoms swimming in a homogeneous sea of neutralizing electrons in contrast to the opposite case in the HEG. Beyond being a canonical system in plasma physics, it turns out the OCP is an appropriate model for some stellar objects and planetary interiors [52].

The classical OCP can be determined through a single parameter, the *Coulomb coupling parameter*,

$$\Gamma \equiv q^2/(ak_BT) \tag{5.1}$$

with a being the average interparticle distance. Using this parameter, some of the first Monte Carlo simulations explored the phases of the classical OCP [31, 52]. First-order quantum mechanical effects have since been included [3, 51, 56, 92]. However, the accuracy of these results quickly deteriorates as the temperature is lowered and quantum correlations play a greater role. This was seen clearly in a more recent a study of the low density OCP with PIMC [57]. The breakdown is most apparent in the warm-dense matter (WDM) regime where both Γ and the *electron degeneracy parameter*,

$$\Theta \equiv T/T_F \tag{5.2}$$

[1] See Chapter 4 for an overview of DFT and the application of the HEG therein.

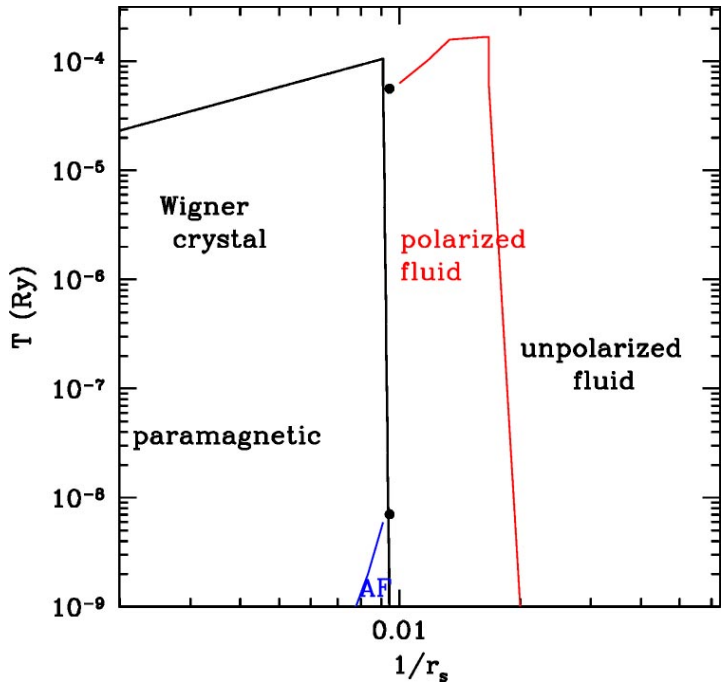

Figure 5.1: Phase diagram of the $3D$ homogeneous electron gas or one-component plasma [110]. At low density and temperature, the system becomes crystallized as predicted by Wigner. At high density and temperature, the system behaves qualitatively like a classical plasma. In between several phase transition lines have been predicted through various numerical studies, discussed in the text [57, 110].

with T_F being the Fermi temperature, are close to unity.

Combining these results with the previous zero-temperature HEG work gives the tentative phase diagram of the $3D$ electron liquid, see Fig. 5.1.[2] We see at zero-temperature both the crystalline phase predicted by Wigner and the polarized phase predicted by Bloch. In between, QMC has predicted an antiferromagnetic phase [110]. Additional exotic spin phases have been speculated from extensive Hartree-Fock calculations [6]. At finite-temperature, low density PIMC simulations determined the crossover temperature into the Wigner crystal phase. The cross over into the polarized phase at finite-temperature is predicted through a simulation of the Stoner model [57]. The finite-temperature antiferromagnetic phase transition point is determined by an excited state QMC calculation [110]. All other areas of the finite-temperature phase diagram are largely unexplored, including the unpolarized regime. This leaves a large swath of uncharted territory, which is precisely the regime where warm-dense matter (WDM) falls.

As mentioned in Chapter 1, WDM bridges the gap between condensed matter and classical plasma physics. Because of the roughly equal competition between thermal, kinetic, interaction, and exchange effects, neither field can provide an accurate picture of the important physics. Condensed matter perturbative

[2]We will use the term *electron liquid* from here on to describe both the HEG and OCP together as the same system.

methods are stymied by the lack of a small parameter around which to perturb. Plasma semi-classical methods are unable to include enough quantum mechanics. Finite-temperature DFT would seem a perfect marriage of the two regimes, but is restricted because of computational tractability and the lack of finite-temperature benchmarks for the electron liquid as described in Chapter 4.

Path integral Monte Carlo (PIMC), as described in Chapters 2 and 3, can fill this void. High-precision PIMC can both uncover the important missing features of the electron liquid phase diagram as well as provide essential benchmarks, just as zero-temperature QMC has up until this point. In the rest of this chapter, we first examine the Hamiltonian of the electron liquid in order to make its various regimes more concrete. We then present the PIMC simulation of the $3D$ electron liquid in the WDM regime as a first attempt to fill in the gaps currently missing from this phase diagram.

5.1 The Hamiltonian

For a system of electrons embedded in a uniform ionic background, the Hamiltonian reads

$$\hat{\mathcal{H}} = \sum_i \frac{\hat{p}_i^2}{2m} + \hat{\mathcal{H}}_{ee} + \hat{\mathcal{H}}_{eb} + \hat{\mathcal{H}}_{bb} \tag{5.3}$$

where

$$\hat{\mathcal{H}}_{ee} = \frac{1}{2}\sum_{i\neq j} v(|\hat{r}_i - \hat{r}_j|) = \frac{1}{2}\sum_{i\neq j} \frac{q^2}{4\pi\epsilon_0}\frac{1}{|\hat{r}_i - \hat{r}_j|}, \tag{5.4}$$

$\hat{p}$ and $\hat{r}$ are the quantum mechanical operators for momentum and position, respectively, m is the electron mass, and q is the electric charge. In a real solid, the ions form a lattice of positive charges. However since we wish to focus simply on the effects of the electron-electron correlation, we treat the ions as a homogeneous background in which the electrons may roam, leading some to call this the *jellium model*.

The final two terms represent the electrons interaction with the ionic background and the background's self-interaction. Specifically these take the form,

$$\hat{\mathcal{H}}_{eb} \equiv \int dr \int dr' \hat{n}(r) n_b(r') v(|r - r'|) \tag{5.5}$$

and

$$\hat{\mathcal{H}}_{bb} \equiv -\frac{1}{2}\int dr \int dr' n_b(r) n_b(r') v(|r - r'|) \tag{5.6}$$

where $\hat{n}$ is the electron density operator,

$$\hat{n}(r) = \sum_{i}^{N} \delta(r - \hat{r}_i), \tag{5.7}$$

and $n_b = n$ is the density of a constant, positive uniform background.

We assume the electrons are contained in a D-dimensional cubic box of side length L and must sum over all periodic images. Here this is denoted by the sum over all D-dimensional unit vectors a. In the thermodynamic limit, both L and N tend to infinity such that the density, $n \equiv \frac{L^D}{N}$, is constant. This changes the electron-electron interaction to become

$$\hat{\mathcal{H}}_{ee} = \frac{1}{2}(\sum_{a} \sum_{i \neq j} v(|\hat{r}_i - \hat{r}_j + aL|) + \hat{N} v_{mad}) \tag{5.8}$$

where we have added the self-interaction due to periodic images, i.e. the Madelung constant

$$v_{mad} \equiv \sum_{a \neq 0} v(|aL|) = \sum_{a \neq 0} \frac{1}{r_s} \frac{1}{|aL|}. \tag{5.9}$$

Because of the long-ranged Coulomb interaction, the sum in (5.8) and integrals in (5.5) and (5.6) do not converge. By examining the full Hamiltonian, however, we see the divergent pieces of the background terms are exactly canceled by the long-ranged part of the electron-electron interaction. To see this it is convenient to transform the Coulomb potential into a Yukawa potential in the limit that α is zero, i.e.

$$v(r) = \frac{1}{r_s} \frac{1}{r} = \lim_{\alpha \to 0} \frac{1}{r_s} \frac{e^{-\alpha r}}{r} = \lim_{\alpha \to 0} v_\alpha(r). \tag{5.10}$$

Taking its Fourier transform we find that the electron-electron interaction becomes,

$$\hat{\mathcal{H}}_{ee} = \frac{1}{2}[\lim_{\alpha \to 0} \sum_{k} \frac{\tilde{v}_\alpha(k)}{L^D} (\hat{n}_{-k} \hat{n}_k - \hat{N}) + \hat{N} v_{mad}] \tag{5.11}$$

where each component of k is an integer multiple of $2\pi/L$, $\tilde{v}_\alpha(k)$ is the Fourier transform of the Yukawa potential, and $\hat{n}_k$ is the Fourier transform of the density operator. Note that subtracting $\hat{N}$ removes the self-interaction term, which was accounted in real space by $i \neq j$. If we do the same for $\hat{\mathcal{H}}_{eb}$ and $\hat{\mathcal{H}}_{bb}$, we find the total Hamiltonian can be written

$$\hat{\mathcal{H}} = \frac{1}{r_s^2} \sum_{i} \hat{p}_i^2 + \frac{1}{2} \lim_{\alpha \to 0} [\frac{1}{L^D} \sum_{k} \tilde{v}_\alpha(k) (\hat{n}_{-k} \hat{n}_k - \hat{N}) + \hat{N} v_{mad} - 2\tilde{v}_\alpha(0) n_b \hat{N} + \tilde{v}_\alpha(0) n_b^2 L^D]. \tag{5.12}$$

Using the fact that $n_b = \hat{n}_{k=0}/L^D = \hat{N}/L^D = n$, we notice we can treat the $k = 0$ term separately as,

$$\hat{\mathcal{H}} = \frac{1}{r_s^2}\sum_i \hat{p}_i^2 + \frac{1}{2}(\lim_{\alpha\to 0}\frac{1}{L^D}[\sum_{k\neq 0}\tilde{v}_\alpha(k)(\hat{n}_{-k}\hat{n}_k - \hat{N}) - \tilde{v}_\alpha(0)\hat{N}] + \hat{N}v_{mad}). \tag{5.13}$$

In the thermodynamic limit, the per particle contribution of the both the $k = 0$ term and Madelung constant goes to zero. Thus we are free to take the $\alpha \to 0$ limit, and we are left with

$$\hat{\mathcal{H}} = \frac{1}{r_s^2}\sum_i \hat{p}_i^2 + \frac{1}{2L^D}\sum_{k\neq 0}\tilde{v}(k)(\hat{n}_{-k}\hat{n}_k - \hat{N}). \tag{5.14}$$

which is completely regularized.

As mentioned in Chapter 2, the Coulomb interaction is necessarily broken into short and long range pieces such that $v(r) = v_s(r) + v_l(r)$, and (5.13) becomes

$$\begin{aligned}\hat{\mathcal{H}} = \frac{1}{r_s^2}\sum_i \hat{p}_i^2 + \frac{1}{2}(\frac{1}{L^D}[\sum_{k\neq 0}(\tilde{v}_s(k) + \tilde{v}_l(k))(\hat{n}_{-k}\hat{n}_k - \hat{N}) - (\tilde{v}_s(0) + \tilde{v}_l(0))\hat{N}] \\ + \hat{N}\sum_{a\neq 0}(v_s(|aL|) + v_l(|aL|)).\end{aligned} \tag{5.15}$$

The short range potential decays quickly, so it is often evaluated directly in position space. The long range potential is kept in momentum space, resulting in

$$\begin{aligned}\hat{\mathcal{H}} = \frac{1}{r_s^2}\sum_i \hat{p}_i^2 + \frac{1}{2}(\sum_a\sum_{i\neq j} v_s(|\hat{r}_i - \hat{r}_j + aL|) + \frac{1}{L^D}[\sum_{k\neq 0}\tilde{v}_l(k)(\hat{n}_{-k}\hat{n}_k - \hat{N}) - (\tilde{v}_s(0) + \tilde{v}_l(0))\hat{N}] \\ + \hat{N}\sum_{a\neq 0}(v_s(|aL|) + v_l(|aL|)).\end{aligned} \tag{5.16}$$

If the short range piece decays to zero within the first periodic image, this simplifies to

$$\hat{\mathcal{H}} = \frac{1}{r_s^2}\sum_i \hat{p}_i^2 + \frac{1}{2}(\sum_{i\neq j} v_s(|\hat{r}_i - \hat{r}_j|) + \frac{1}{L^D}[\sum_{k\neq 0}\tilde{v}_l(k)(\hat{n}_{-k}\hat{n}_k) - \tilde{v}_s(0)\hat{N}] - v_l(0)\hat{N}) \tag{5.17}$$

which we compare to the potential breakup in Chapter 2.

Typically, we rescale the Hamiltonian into energy units of Rydbergs and length units of the Wigner-Seitz

radius. The latter is defined through the density by

$$r_s a_0 \equiv \begin{cases} (\frac{3}{4\pi n})^{1/3}, & 3D \\ (\frac{1}{\pi n})^{1/2}, & 2D \\ \frac{1}{2n}, & 1D \end{cases} \tag{5.18}$$

where a_0 is the Bohr radius. It is simple to show this the rescaled Hamiltonian takes the form

$$\hat{\mathcal{H}} = (\frac{1}{r_s^2}\sum_i \hat{p}_i^2 + \hat{\mathcal{H}}_{ee} + \hat{\mathcal{H}}_{eb} + \hat{\mathcal{H}}_{bb})Ry \tag{5.19}$$

where $Ry = \frac{q^2}{2a_0}$ and the interaction potential becomes

$$v(r) = \frac{1}{r_s}\sum_{i\neq j}\frac{1}{|\hat{r}_i - \hat{r}_j|}. \tag{5.20}$$

In this parametrization, the limits of the HEG become apparent. At high density, $r_s \ll 1$, and the kinetic term dominates. At low density, $r_s \gg 1$, and the potential term dominates. Thus by tuning a single parameter, the electron liquid ranges from a strongly correlated to weakly correlated system. It is this variability that has made the HEG a canonical playground for condensed matter theorists and spurred decades of investigation. At the same time, it also what makes its analytic study exceedingly difficult. As we shall see, however, PIMC is able to handle the full extent of properties, simultaneously addressing strong and weak correlation.

5.2 Path integral simulation

In the preceding we present calculations of the $3D$ finite-temperature homogeneous electron gas in the warm-dense regime ($r_s \equiv (3/4\pi n)^{1/3}a_0^{-1} = 1.0 - 40.0$ and $\Theta \equiv T/T_F = 0.0625 - 8.0$) using restricted path integral Monte Carlo (RPIMC), a method we reviewed in Chapters 2 and 3. We begin with a overview of simulation specifics including all possible sources of error, while trying to avoid duplication of previous chapters. We then present the precise energies, pair correlation functions, and structure factors obtained. For all densities, we find a significant discrepancy between the ground state parameterized local density approximation and our results around the Fermi temperature, T_F. In Fig. 5.2, we show the specific points in the warm-dense matter regime were simulated for both fully spin-polarized $\xi = 1$ and unpolarized $\xi = 0$ systems, where $\xi \equiv (N_\uparrow - N_\downarrow)/(N_\uparrow + N_\downarrow)$. All simulated points lie well within the WDM regime.

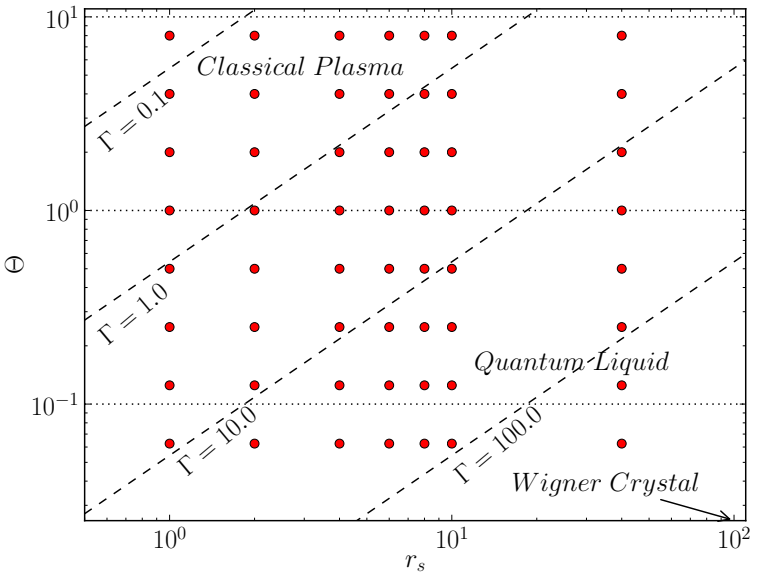

Figure 5.2: Temperature-Density points considered in the current study (dots). Several values of the Coulomb coupling parameter Γ (dashed lines) and the electron degeneracy parameter Θ (dotted lines) are also shown.

5.2.1 Nodal Constraint

PIMC allows in-principle exact calculations of equilibrium properties of quantum systems. For fermions, however, statistical weights of approximately equal magnitude and opposite sign make direct simulation computationally intractable at low temperatures. To circumvent this difficulty, a constraint is imposed such that sampled paths remain within the strictly positive region of a trial density matrix. Here we employ the free-electron density matrix,

$$\rho_0(R, R', \tau) = (4\pi\tau/r_s^2)^{-3N/2} \exp[-\frac{(r_i - r'_j)^2}{4\tau/r_s^2}] \tag{5.21}$$

where $R \equiv \{r_i\}$ is the set of all $3N$ particle coordinates and $\tau \equiv \beta/M$ with M the number of imaginary time discretizations. We expect this approximation to be best at high temperature and at low-density when correlation effects are weak. Specifically we compare (5.21) to the Feynman-Kac formulation for the full density matrix,

$$\rho_F(R, R', \beta) = \mathcal{A}\rho_0(R, R', \beta)\langle \exp[-\int_0^\beta d\tau V(R(\tau))]\rangle \tag{5.22}$$

where $\mathcal{A}$ is the anti-symmetrization operator and $\langle \dots \rangle$ denotes an average over Brownian walks from R' to R. As $\beta \to 0$, this average tends to unity, leaving only the anti-symmetrized kinetic term. Thus for any potential $V(R)$ bounded from below, the nodes of the full density matrix equal the nodes of the free-particle density matrix in the high-temperature limit.

Furthermore, we expect free-particle nodes to be accurate for a homogeneous system, such as the electron gas, where translational symmetry constrains the possible nodal surfaces [20]. Nevertheless further accounting of this approximation will be made through connection to prior semi-classical and ground-state simulations as well as exact evaluation of the unrestricted density matrix at higher temperatures. This is the only truly uncontrolled source of error in our calculations.

For the HEG, we make use of the nodal image action given in (3.37) since we find it has superior convergence properties for the regime of interest, see Fig. 3.3. Additionally, we use the hybrid update scheme described in Chapter 3 in order to calculate the nodal distance.

5.2.2 Statistical convergence

An error comes from the stochastic nature of the Monte Carlo algorithm itself. Throughout Monte Carlo sampling, each estimate will be different, however their average is guaranteed to converge as $N_{samp}^{-1/2}$ by the central limit theorem, where N_{samp} is the number of Monte Carlo steps [70]. Thus the statistical error can be controlled by simply gathering more statistics through sampling additional configurations. The standard error of the mean is then defined as

$$\epsilon = \sqrt{\frac{\sigma^2}{N_{samp}}} \tag{5.23}$$

where σ^2 is the variance given by

$$\sigma^2 = \frac{1}{N_{samp}-1} \sum_{i=1}^{N_{samp}} (\mathcal{O}_i - \langle \hat{\mathcal{O}} \rangle). \tag{5.24}$$

On the other hand, the central limit theorem assumes each configuration to be independent, which is in general not true in Monte Carlo sampling. Without enough time to diffuse between configurations, there will be a correlation between consecutive measurements. To calculate the contribution to the total error coming from auto-correlation, we define the error

$$\epsilon = \sqrt{\frac{\sigma^2}{N_{eff}}} \tag{5.25}$$

where N_{eff} is the number of statistically independent samples. We approximate N_{eff} as the total number of samples $N_{samples}$ divided by an auto-correlation constant κ defined as

$$\kappa \equiv 1 + \frac{2}{\sigma^2} \sum_{t=1}^{\infty} C(t). \tag{5.26}$$

For a discrete set of the data, the autocorrelation time $C(t)$ can be approximated

$$C(t) \approx \frac{1}{(N_{samp}-t)\sigma^2} \sum_{s=1}^{N_{samp}-t} (\mathcal{O}_s - \langle\mathcal{O}\rangle)(\mathcal{O}_{s+t} - \langle\mathcal{O}\rangle), \tag{5.27}$$

and the infinite sum is taken only to N_{samp} or until a single $C(t)$ value becomes negative.

Before long production runs, we first try to determine the autocorrelation time through this measure. We then average consecutive measurements into blocks of the same length and compute error estimates only from these blocks. A true estimate of the error can be found by taking larger and larger block sizes until the error converges. For most points, we were able to run long enough to have statistical errors on the same order or smaller as the other controllable errors. However, for the highest density points and lowest temperatures, the simulation can become very slow and the auto-correlation time long (see Chapter 3). For these points, statistics are gathered mainly through parallelization, though the statistical errors are still an order of magnitude larger than other controllable errors.

5.2.3 Time step convergence

As mentioned in Chapter 2, all discretizations of the many-body action incur a time step order. The primitive approximation comes with a time step error of $\mathcal{O}(\lambda\tau^2)$. To do better, we utilize the pair product approximation and write the many-body density matrix as a product of high-temperature two-body density matrices.

To account for the long-range nature of the Coulomb interaction, we split the density matrix into a short-range and long-range piece. Each short-range two-body density matrix is exactly solved at an even higher temperature, and then squared down to the temperature of interest τ^{-1}. It is then fit to expansion specified by 3 free parameters. Rebuilding the many-body density matrix out of such two-body density matrices comes with an error that scales as $\mathcal{O}(\tau^3/r_s^2)$. The long-range piece is included via Ewald summation at the level of the primitive approximation. Again this should incur an error that scales as $\mathcal{O}(\tau^2)$. However, because the primitive approximation also converges at large distances, the relative magnitude of this error is often an order of magnitude or more smaller than that of the short-range action. The precise form of this action is given in Chapter 2.

The final time step error originates from the nodal constraint. If included at the primitive approximation level, there is an additional error, beyond the usual $\mathcal{O}(\tau^2)$, arising from paths that cross and recross the nodal surface in an imaginary time less than τ. This crossing error can scale as poorly as $\mathcal{O}(\ln\tau)$. To help alleviate this effect, we use an image action to discourage paths from getting too close to nodes. The precise

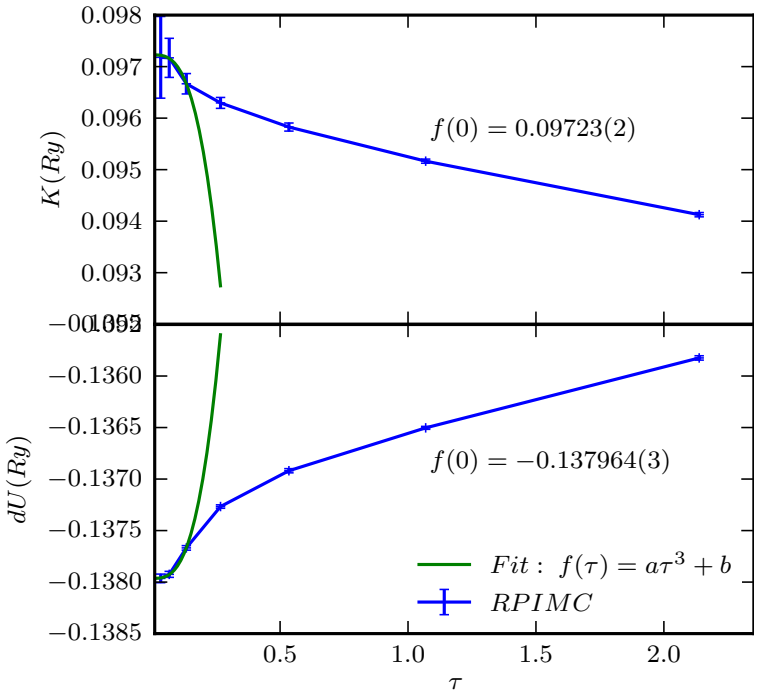

Figure 5.3: Convergence in τ for $\xi = 1$ and $r_s = 10.0$.

	r_s						
	1.0	2.0	4.0	6.0	8.0	10.0	40.0
$\xi = 0$	0.0005	0.0042	0.0170	0.0382	0.0679	0.1061	3.3938
$\xi = 1$	0.0007	0.0027	0.0214	0.0481	0.0855	0.1336	2.1380

Table 5.1: Time step τ (Ry^{-1}) used for each density r_s and polarization ξ.

form of this nodal action is given by (3.37).

In Fig. 5.3 we show the behavior of the time step convergence for $r_s = 10.0$, $\Theta = 1.0$, and $\xi = 1$ in both the kinetic K and potential $(dU/d\beta)$ energies. We see that for the smallest time steps, the convergence is roughly $\mathcal{O}(\tau^3)$ as predicted for the pair action. We performed a similar time step study for each polarization and density. At a specific density, once we found a value for τ which made the time step error smaller than the desired statistical error, we used it for all temperatures at that density. In this way changing temperatures simply amounts to changing the total number of time slices to represent a single particle. Table 5.1 gives the final time step used during simulations for each polarization and r_s.

5.2.4 Finite size effects

In order to provide useful benchmarks for DFT and the like, calculations must be accurate in the thermodynamic limit $N \to \infty$. Thus, for finite-size systems, a correction must be made to both the kinetic and potential terms. Finite-size errors for the HEG come from two sources. This first originates from the

discretization of the Fermi surface and approximating the Fermi sphere with a finite number of k-shells. To address this error, it helps to take N to be a so-called *magic number* which completely fills a fixed number of bands for the free Fermi gas. This helps to alleviate shell effects arising from a sharp Fermi surface. For the fully spin-polarized system, we simulated $N = 33$ electrons, while for the unpolarized system, we simulated $N = 66$ electrons, both of which are magic numbers.

The second source of finite-size error originates specifically from the long-range part of the interaction, which extends well beyond the size of the periodic box. To address this error in the potential, recall from (5.14) that

$$V_N = \sum_{k\neq 0} \frac{\tilde{v}_\alpha(k)}{L^D}(\hat{n}_{-k}\hat{n}_k - \hat{N}) \tag{5.28}$$

$$= \frac{2\pi}{r_s L^D}\sum_{k\neq 0}\frac{1}{k^2}(S_N(k) - 1). \tag{5.29}$$

where $S_N(k) \equiv \langle \hat{n}_{-k}\hat{n}_k\rangle/N$ is the finite-size static structure factor. As $N \to \infty$, the sum over k vectors is on a finer mesh, eventually becoming a smooth integral. This allows us to write the finite-size error as,

$$\Delta V_N = \frac{1}{4\pi^2 r_s}\int dk \frac{1}{k^2}(S(k) - 1) - \frac{2\pi}{r_s L^D}\sum_{k\neq 0}\frac{1}{k^2}(S_N(k) - 1) \tag{5.30}$$

where $S(k)$ is the structure factor in the thermodynamic limit. The leading order contribution comes from the terms without the structure factors and is simply the Madelung constant of (5.9). The remainder of the error originates from the discretization of the integral and the substitution of $S_N(k)$ for $S(k)$. The large k part of the structure factor originates from the short-range correlation, making its contribution to (5.30) negligible. For small k, the random phase approximation (RPA) becomes valid and implies that $S_N(k) \approx S(k)$ [27]. Thus the finite-size error in the potential originates mostly from the $k = 0$ term missing from the sum,

$$\Delta V_N = v_{mad} + \frac{1}{4\pi^2 r_s}\int dk \frac{1}{k^2}S(k) - \frac{2\pi}{r_s L^D}\sum_{k\neq 0}\frac{1}{k^2}S_N(k) \tag{5.31}$$

$$\approx v_{mad} + \frac{1}{4\pi^2 r_s}\int_{\mathcal{D}} dk \frac{1}{k^2}S(k) \tag{5.32}$$

where $\mathcal{D}$ is a k-space domain of volume $2\pi/L^D$ centered at $k = 0$. For the electron liquid, we know the small k form of $S(k)$ coming from the RPA [4], leading us to the final form of the potential energy finite size correction,

$$\Delta V_N = \frac{\omega_p}{2N} \tag{5.33}$$

where ω_p is the RPA plasmon frequency. In $3D$, $\omega_p = \sqrt{3/r_s^3}$.

The leading order kinetic finite-size effect may be found simply through a coupling constant integration in which

$$\begin{aligned} \Delta K_N &= \Delta E_N - \Delta V_N & (5.34) \\ &= \frac{1}{r_s^2}\int_0^{r_s} dr_s r_s \Delta V_N(r_s) - \Delta V_N & (5.35) \\ &= \frac{\omega_p}{2N}. & (5.36) \end{aligned}$$

At intermediate and high densities, however, a next order correction to the kinetic energy is necessary [35]. This is calculated by simply including the term beyond $\mathcal{O}(k^2)$ in the RPA structure factor, giving,

$$\Delta K_N = \frac{1}{N}\left(\frac{\omega_p}{2} + \frac{5.264}{\pi r_s^2 (2N)^{1/3}}[(1+\xi)^{2/3} + (1-\xi)^{2/3}]\right).$$

To account for finite-size at finite-temperature these corrections must be slightly modified. The error arising from the discretization of the Fermi surface should decay with increased temperature as the Fermi surface is no longer sharp, implying the *magic numbers* are still appropriate. Near $T = 0$, the forms of (5.33) and (5.34) are still appropriate, only instead we input the finite-temperature RPA structure factor. This amounts to multiplying the potential correction by $\coth(\beta\omega_p)$ and the kinetic correction by $\tanh(\beta\omega_p)$. Since it relies on the validity of the RPA at long-wavelength, this correction should still be accurate provided the small k behavior of the static structure factor behaves as in the RPA.

As T grows, this correction becomes inadequate. Instead, a more useful correction for these points extends from the classical regime. Again we may write the potential energy as $V = \frac{1}{2\Omega}\sum_k \frac{4\pi q^2}{k^2} S(k)$ where now the exact structure factor is given by

$$S(k) = \frac{2k^2}{r_s^2 \omega_p(k)}\left[\frac{1}{\exp^{\omega_p/T} - 1} + \frac{1}{2}\right]. \quad (5.37)$$

Here

$$\omega_p^2(k) \equiv \sqrt{\frac{3}{r_s^3}}(1 + k^2/k_s^2) \quad (5.38)$$

with

$$k_s^2 \equiv \frac{4\pi}{r_s(\partial\mu/\partial r_s)_T}, \quad (5.39)$$

though since we are mostly concerned with the small k limit, we take $\omega(k) \simeq \omega_p = \sqrt{3/r_s^3}$. The finite-size correction then just reads as $\Delta V = V_\infty - V_N$. This correction is again dominated by the long-wavelength

$(k \to 0)$ contribution. For $T \ll 1$ we recover the correction in (5.33). For $r_s \gg T^{-2/3}$, however, we arrive upon

$$\Delta V = \frac{T}{2N}. \tag{5.40}$$

At finite-temperatures, the virial theorem is $2T + V = 3PV$ where $P \equiv \partial F/\partial\Omega|_T$. If we ignore the finite-size correction coming from the entropy, we can use the same coupling constant integration as in (5.34) to find $\Delta E = T/(4N)$. Taking the difference with ΔV, we then find

$$\Delta K = -\frac{T}{4N}. \tag{5.41}$$

5.2.5 Energies

With the above accounting of possible errors, we are ready to calculate actual observables beginning with the energy. The most straight-forward to calculate the energy is to take the β derivative of the of the many-body partition function,

$$\begin{aligned}
\langle E \rangle &= -\frac{1}{\mathcal{Z}}\frac{\partial \mathcal{Z}}{\partial \beta} && (5.42)\\
&= -\frac{1}{\mathcal{Z}}\frac{\partial}{\partial \beta}\int \prod_{j=0}^{M-1} dR_j \prod_{i=1}^{M} e^{-S(R_{i-1},R_i;\tau)} && (5.43)\\
&= -\frac{1}{\mathcal{Z}}\frac{1}{M}\int \prod_{j=0}^{M-1} dR_j \frac{\partial \sum_{k=0}^{k-1} \mathcal{S}(R_k, R_{k+1};\tau)}{\partial \tau} \prod_{i=1}^{M} e^{-S(R_{i-1},R_i;\tau)} && (5.44)\\
&= \frac{1}{M}\sum_{k=1}^{M} \langle \frac{\partial \mathcal{S}(R_{k-1}, R_k;\tau)}{\partial \tau} \rangle && (5.45)\\
&= \frac{1}{M}\sum_{k=1}^{M} \langle \frac{DN}{2\tau} - \frac{(R_{k-1}-R_k)^2}{4\lambda\tau^2} + \frac{\partial \mathcal{U}(R_{k-1}, R_k;\tau)}{\partial \tau} \rangle. && (5.46)
\end{aligned}$$

where we have used the many-body action $\mathcal{S}$ given in Chapter 2. We define the kinetic and potential pieces of the total energy to be

$$\langle \mathcal{K} \rangle = \frac{1}{M}\sum_{k=1}^{M} \langle \frac{DN}{2\tau} - \frac{(R_{k-1}-R_k)^2}{4\lambda\tau^2} \rangle \tag{5.47}$$

and

$$\langle \mathcal{U} \rangle = \frac{1}{M}\sum_{k=1}^{M} \langle \frac{\partial \mathcal{U}(R_{k-1}, R_k;\tau)}{\partial \tau} \rangle \tag{5.48}$$

respectively.

Since we are using the nodal image action, it also makes a contribution to the total energy. Taking the

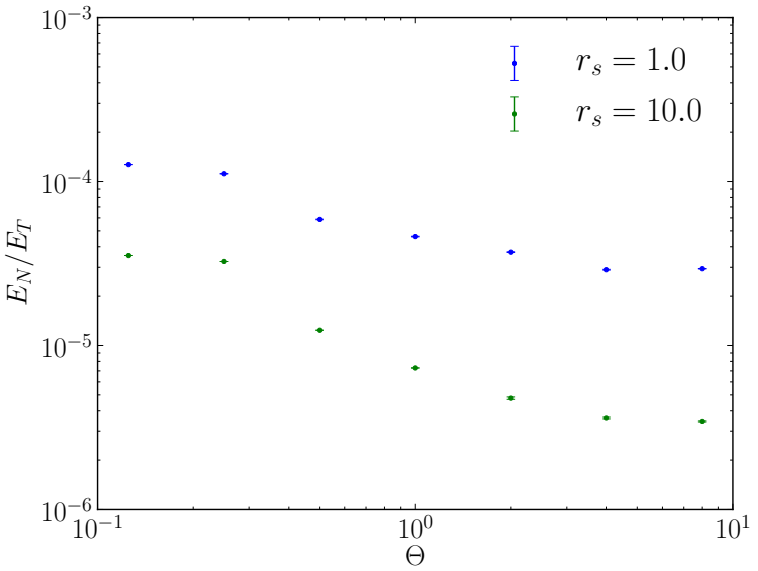

Figure 5.4: Relative contribution of the nodal energy for $r_s = 1.0$ and $r_s = 10.0$ for various temperatures $\Theta = T/T_F$ of the unpolarized state.

τ derivative of (3.37), we find

$$\frac{\partial \mathcal{U}_N}{\partial \tau} = -\frac{\partial}{\partial \tau} \sum_{n,n'=0}^{\infty} \ln\left[1 - \exp\left(-\frac{(d_{i-1}+nL)(d_i+n'L)}{\lambda\tau}\right)\right] \tag{5.49}$$

$$= -\sum_{n,n'=0}^{\infty} \frac{\frac{\partial}{\partial\tau}\left(\frac{(d_{i-1}+nL)(d_i+n'L)}{\lambda\tau}\right)}{\exp\left(\frac{(d_{i-1}+nL)(d_i+n'L)}{\lambda\tau}\right) - 1} \tag{5.50}$$

$$\equiv \sum_{n,n'=0}^{\infty} \frac{x_i(\tau)}{\lambda\tau(e^{x_i(\tau)}-1)}\left[1 - \frac{\partial}{\partial\tau}\ln\left(\tau x_i(\tau)\right)\right] \tag{5.51}$$

where we have defined $x_i \equiv (d_{i-1}+nL)(d_i+n'L)/\tau$. The τ derivative of the nodal distances is essentially zero, particularly at low temperatures. Indeed, the entire nodal contribution is essentially always the smallest contribution to the total energy. To visualize this, in Fig. 5.4, we plot the nodal energy as a relative fraction of the total energy at all temperatures with $r_s = 1.0$ and $r_s = 10.0$ for the unpolarized state. We see that while the nodal energy is largest at lower temperatures, its contribution to the total energy is almost negligible. At high density ($r_s = 1.0$), the nodal energy is two orders of magnitude larger than that of the low density system ($r_s = 10.0$). Because the nodal surface cuts through particle coincidence points, the density of nodes is directly proportional to the density of particles. Thus in a low density system, particles are often far away from the nodal surface, minimizing $\mathcal{U}_N$ and E_N.

In Fig. 5.5 we plot the total excess energy $(E_{tot} - E_0)/E_0$ for the polarized system at all temperatures with $r_s = 4.0$ and 40.0, where E_0 is defined to the be energy of the equivalent free fermion system. At

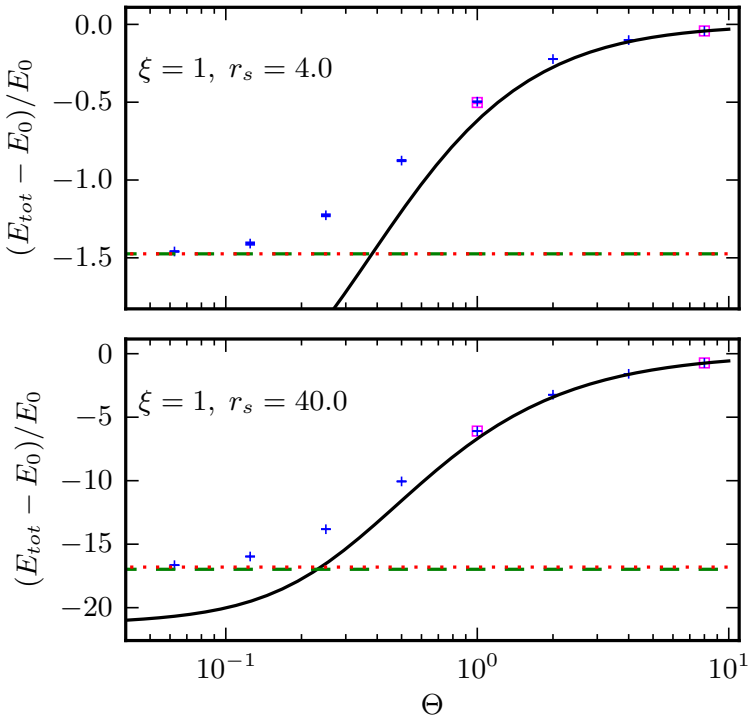

Figure 5.5: Excess energies for $r_s = 4.0$ (top) and $r_s = 40.0$ (bottom) for the polarized state. For both densities, the high temperature results fall smoothly on top of previous Monte Carlo energies for the classical electron gas [52] (solid line). Differences from the classical coulomb gas occur for $\Theta < 2.0$ for $r_s = 4.0$ and $\Theta < 4.0$ for $r_s = 40.0$. Simulations with the Fermion sign (squares) confirm the fixed-node results at $\Theta = 1.0$ and 8.0. The zero-temperature limit (dotted line) smoothly extrapolates to the ground-state QMC results of Ceperley-Alder [22] (dashed line).

the highest temperatures, our results match well with the purely classical Monte Carlo results of Ref. [52] (solid line). Tables 5.2 and 5.3 give this comparison at the highest temperature simulated ($\Theta = 8.0$) for the unpolarized and polarized liquid. For a few select points, we have performed the much more time-consuming but more accurate, signful PIMC simulation (squares). Where they were simulated, these points which are essentially exact, i.e. without possible nodal error, and match well with fixed-node results, see Tables 5.4 and 5.5. Finally, we know from Fermi liquid theory the low-temperature gas should have a linear form for the heat capacity, and therefore a quadratic form for the internal energy [43]. Thus for each density we fit the low-temperature points to a quadratic function and extrapolate to $0K$. Fig. 5.5 shows the extrapolated results (dotted line) match well with the zero-temperature QMC results of Ceperley-Alder [22] (dashed line). For a list of all zero-temperature extrapolations, see Tables 5.6 and 5.7.

r_s	1.0	2.0	4.0	6.0	8.0	10.0	40.0
E_{tot}	43.92(2)	10.788(4)	2.575(1)	1.0839(5)	0.5725(3)	0.3414(2)	−0.00619(1)
E_{tot}^{H}	43.798526	10.771176	2.575541	1.082986	0.571223	0.339894	−0.006384

Table 5.2: Comparison of energies at $\Theta = 8.0$ to the classical results of [52] at all densities simulated for the unpolarized liquid.

r_s	1.0	2.0	4.0	6.0	8.0	10.0	40.0
E_{tot}	70.07(2)	17.360(4)	4.224(4)	1.823(1)	0.991(1)	0.6117(6)	0.01232(6)
E_{tot}^{H}	69.832322	17.309836	4.227612	1.824996	0.992689	0.612032	0.011957

Table 5.3: Comparison of energies at $\Theta = 8.0$ to the classical results of [52] at all densities simulated for the polarized liquid.

r_s	Θ	$\langle sgn \rangle$	E_{tot}^{exact}	E_{tot}
1.0	1.0	0.0002(10)	−17(123)	5.21(2)
4.0	1.0	0.0040(7)	0.08(16)	0.083(1)
10.0	1.0	0.092(1)	−0.071(2)	−0.0719(1)
40.0	1.0	0.7689(9)	−0.03350(3)	−0.033504(7)
1.0	8.0	0.5568(5)	43.98(6)	43.92(2)
4.0	8.0	0.7415(3)	2.579(2)	2.575(1)
10.0	8.0	0.9070(2)	0.3418(2)	0.3414(2)
40.0	8.0	0.99826(3)	−0.006202(8)	−0.00619(1)

Table 5.4: Comparison of signful calculation E_{tot}^{exact} with the fixed-node calculations E_{tot} for the unpolarized ($\xi = 0.0$) gas at select densities and temperatures. The average value of the sign is shown for reference.

r_s	Θ	$\langle sgn \rangle$	E_{tot}^{exact}	E_{tot}
4.0	0.0625	−0.00055(62)	−0.5(1)	−0.1023(7)
10.0	0.0625	−0.002(1)	−0.16(2)	−0.1010(1)
1.0	1.0	0.0023(5)	2(4)	8.78(3)
4.0	1.0	0.0725(2)	0.306(3)	0.309(1)
10.0	1.0	0.4076(5)	−0.0374(2)	−0.0371(5)
40.0	1.0	0.9498(2)	−0.031581(6)	−0.03163(3)
1.0	2.0	0.0187(1)	17.5(4)	17.41(2)
1.0	4.0	0.1989(1)	34.97(3)	34.97(2)
1.0	8.0	0.5286(1)	70.11(2)	70.07(2)
4.0	8.0	0.8408(2)	4.226(2)	4.224(4)
10.0	8.0	0.93796(7)	0.6115(1)	0.6117(6)
40.0	8.0	0.99851(1)	0.012275(9)	0.01232(6)

Table 5.5: Comparison of signful calculation E_{tot}^{exact} with the fixed-node calculations E_{tot} for the polarized ($\xi = 1.0$) gas at select densities and temperatures. The average value of the sign is shown for reference.

r_s	$E_{tot}(0)$	$\lim_{T\to 0} E_{tot}(T)$	$E_c(0)$	$\lim_{T\to 0} E_c(T)$
1.0	$1.1726(2)^b$	1.16(1)	$-0.1210(2)$	$-0.13(1)$
2.0	$0.0041(4)^a$	0.003(2)	$-0.0902(4)$	$-0.091(2)$
4.0	$-0.1547(1)^d$	$-0.1542(5)$	$-0.0637(1)$	$-0.0632(5)$
6.0	$-0.1422(1)^d$	$-0.1425(2)$	$-0.0509(1)$	$-0.0512(2)$
8.0	$-0.1228(1)^d$	$-0.1228(1)$	$-0.0428(1)$	$-0.0428(1)$
10.0	$-0.10687(2)^b$	$-0.10643(8)$	$-0.03734(2)$	$-0.03690(8)$
40.0	$-0.0352375(6)^c$	$-0.035153(3)$	$-0.0137104(6)$	$-0.013626(3)$

Table 5.6: Zero-temperature extrapolations, $\lim_{T\to 0} E_{tot}(T)$, of finite-temperature PIMC calculations for the unpolarized ($\xi = 0.0$). We compare $E_{tot}(0)$ directly to previous QMC studies where possible (a, [22]), (b, [110]), (c, [69]), otherwise the Perdew-Zunger parameterization (d, [88]) is used.

r_s	$E_{tot}(0)$	$\lim_{T\to 0} E_{tot}(T)$	$E_c(0)$	$\lim_{T\to 0} E_c(T)$
1.0	$2.2903(1)^d$	2.29(1)	$-0.0632(1)$	$-0.07(1)$
2.0	$0.2517(6)^a$	0.251(2)	$-0.0480(6)$	$-0.048(2)$
4.0	$-0.1040(1)^d$	$-0.1042(6)$	$-0.0346(1)$	$-0.0348(6)$
6.0	$-0.1230(1)^d$	$-0.1228(3)$	$-0.0280(1)$	$-0.0278(3)$
8.0	$-0.1134(1)^d$	$-0.1130(2)$	$-0.0239(1)$	$-0.0235(2)$
10.0	$-0.1013(1)^a$	$-0.1013(1)$	$-0.0209(1)$	$-0.0209(1)$
40.0	$0.0351348(7)^c$	$-0.034894(8)$	$0.0618048(7)$	$-0.008224(8)$

Table 5.7: Zero-temperature extrapolations, $\lim_{T\to 0} E_{tot}(T)$, of finite-temperature PIMC calculations for the polarized ($\xi = 1.0$). We compare $E_{tot}(0)$ directly to previous QMC studies where possible (a, [22]), (b, [110]), (c, [69]), otherwise the Perdew-Zunger parameterization (d, [88]) is used.

5.2.6 Pair Correlations

An additional quantity of interest is the real space pair correlation function defined as

$$g(r) = \frac{2\Omega}{N^2}\langle \sum_{i<j} \delta(r_{ij} - r)\rangle \tag{5.52}$$

where $r_{ij} \equiv |r_i - r_j|$. For simulations with separate spin channels, the total pair correlation function is simply $g(r) = g_{\uparrow\uparrow}(r) + g_{\downarrow\uparrow}(r)$. In typical PIMC simulations, $g(r)$ may be averaged over all time slices. When imposing a fixed-node constraint, the reference slice breaks the time slice symmetry and $g(r)$ is only well-defined on the reference slice itself. For the HEG, however, we see negligible differences between the time slice averaged quantity and the reference slice pair correlation function. It is thus advantageous to take advantage of the time slice averaging for better statistical efficiency.

In Fig. 5.6 we plot the total pair correlation functions for $r_s = 1.0$ and $r_s = 10.0$ in the unpolarized state at all simulated temperatures. As is the case for the total energy, we again see a convergence to analytic ground-state curves. The small r behavior slightly deviates for $r_s = 1.0$, but this is due to the poor quality of small r QMC data which was used to create the analytic fit [48]. To show the classical limit, we also plot

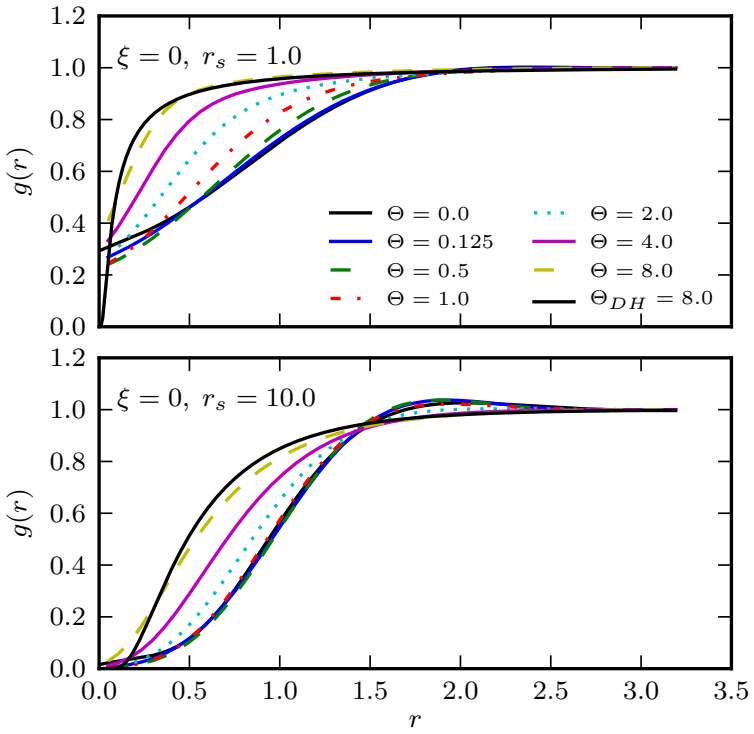

Figure 5.6: Total pair correlation functions for $r_s = 1.0$ and $r_s = 10.0$ in the unpolarized state. At $\Theta = 0.0$ is shown the ground state correlation function from Ref. [48]. Deviation from RPIMC is seen at small r, but this is most likely due to poor ground-state QMC data [47]. Also shown is the small r part of $g_{DH}(r)$ at $\Theta = 8.0$, see (5.53). The Debye-Huckel limit is not yet reached at $\Theta = 8.0$ for the lower density $r_s = 10.0$.

the Debye-Huckel pair correlation function given by,

$$g_{DH}(r) = \exp[-r\theta \exp(-r\sqrt{3/\theta})] \tag{5.53}$$

where $\theta \equiv \frac{r_s T}{2}$. As was noted in Ref. [52], convergence of $g(r)$ to the Debye-Huckel limit is slower than for the energy and even at $\Theta = 8.0$, the data does not yet converge to the Debye-Huckel limit.

Between the two densities, we see that the low density electron liquid has a much larger correlation hole than the high density liquid. This again reflects the increased role of the interaction potential at low density. To make this point clearer, in Figs. 5.7 and 5.8 we plot the pair correlation functions for each individual spin channel for the same two densities. For unlike spins, at high density the contact probability is much greater than zero. Interestingly, the correlation hole grows and shrinks as the system decreases in temperature with a maximum unlike spin correlation hole around the Fermi temperature. For like spins the contact probability is zero by definition. At low density the separate spin channels look qualitatively similar, both with larger correlation holes. Again for all cases, we see the smooth convergence to the previous ground state result. Finally, all densities simulated are still within the liquid regime, and thus the pair correlation function in

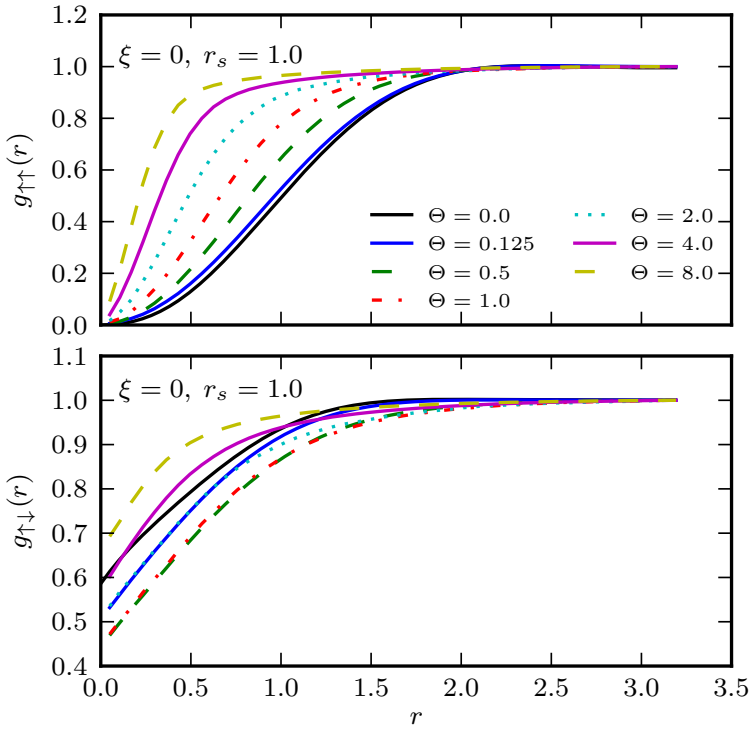

Figure 5.7: Pair correlation functions for each spin channel for $r_s = 1.0$ at several temperatures. Each extrapolates well to the ground state $\Theta = 0.0$ analytic result provided by [48].

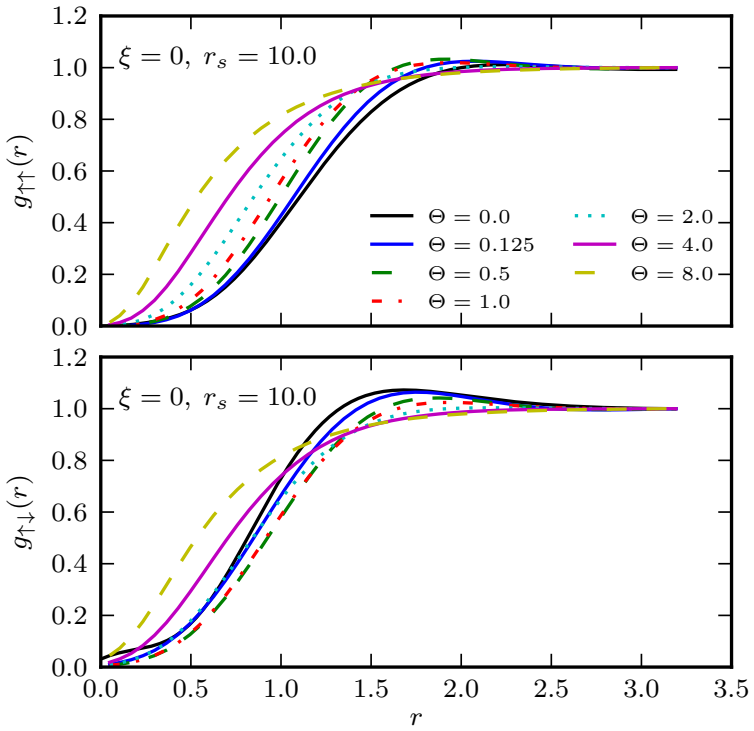

Figure 5.8: Pair correlation functions for each spin channel for $r_s = 10.0$ at several temperatures. Each extrapolates well to the ground state $\Theta = 0.0$ analytic result provided by [48].

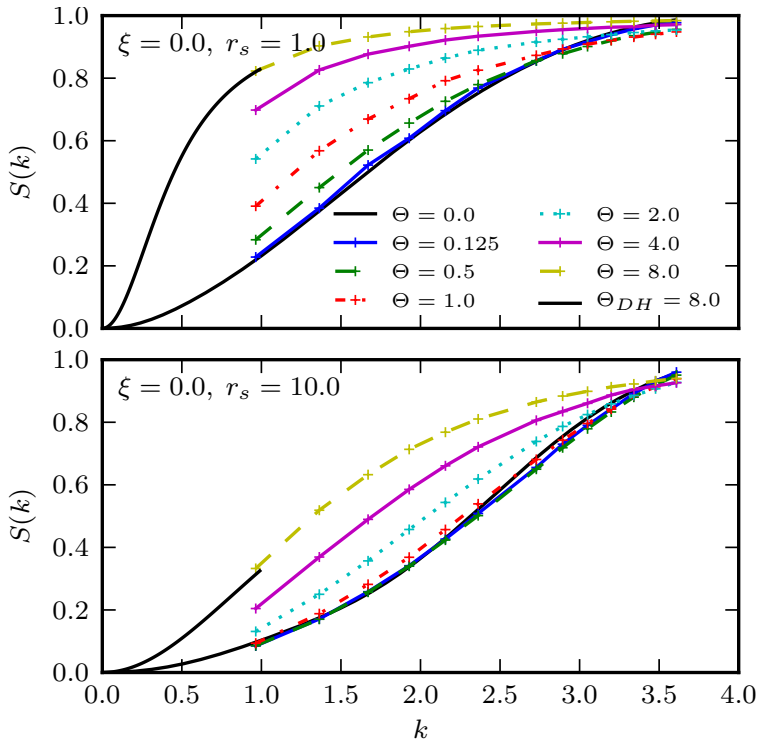

Figure 5.9: Total static structure factors for $r_s = 1.0$ and $r_s = 10.0$ in the unpolarized state. At $\Theta = 0.0$ we plot the ground state structure factor from Ref. [48]. Also shown is the small k part of $S_{DH}(k)$ at $\Theta = 8.0$, see (5.56).

smooth with a single rounded peak around the nearest neighbor distance.

5.2.7 Structure Factors

An alternative correlation function to measure is the structure factor, a quantity that derives its name from its use in the characterization of many-body structure. It is defined as

$$S(k) = \frac{1}{N}\langle \sum_{i<j} \mid \rho_k \mid^2 \rangle \tag{5.54}$$

where $\rho_k \equiv e^{-ik(r_{ij})}$. The structure factor can also be defined through the Fourier transform pair correlation function as

$$S(k) = 1 + \frac{N}{\Omega}\int dr e^{ikr}(g(r) - 1), \tag{5.55}$$

however this integral is much more difficult to compute in practice than measuring $S(k)$ as in (5.54).

Fig. 5.9 shows the calculated structure factors for the unpolarized state at $r_s = 1.0$ and $r_s = 10.0$. Note that for $\xi = 0$, $S(k) = S_{\uparrow\uparrow}(k) + S_{\uparrow\downarrow}(k)$. At all densities and polarizations, we again see a smooth convergence

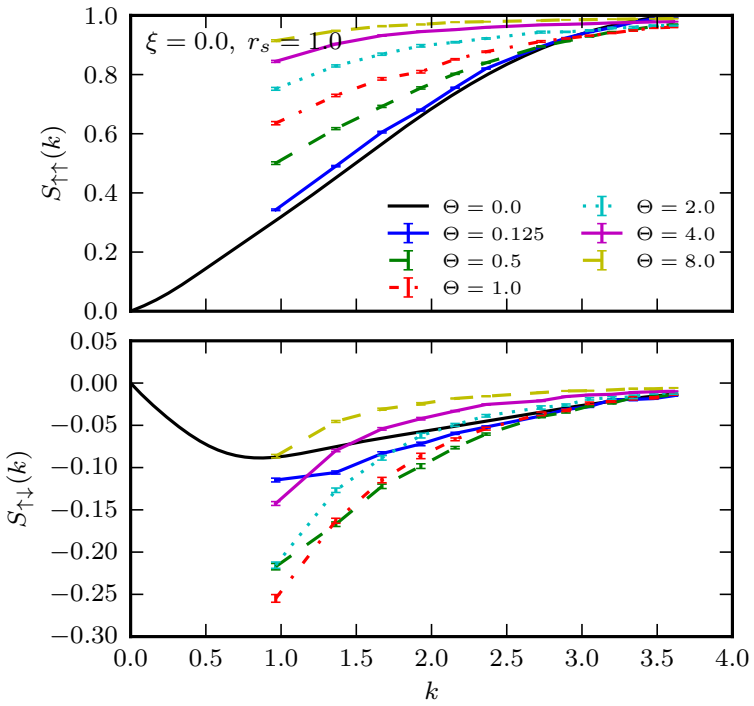

Figure 5.10: Static structure factors for each spin channel for $r_s = 1.0$ in the unpolarized state at several temperatures. At $\Theta = 0.0$ we plot the ground state structure factor from Ref. [48].

to both the ground-state and classical Debye-Huckel limits. Zero-temperature curves are generated through an analytic fit to previous QMC data [48], while Debye-Huckel curves are generated using [52],

$$S_{DH}(k) = \frac{k^2}{k^2 + 3\Gamma}. \tag{5.56}$$

The convergence to the classical limit is much faster for the structure factor than for the pair correlation function. Because of the finite box size, the simulation is incapable of measuring the structure factor for $k < 2\pi/L$. All finite-temperature data is bracketed by the ground state and classical limits and each has a k^2 dependence at small k. This leads us to believe the RPA finite-size correction discussed above is appropriate for these systems. In Figs. 5.10 and 5.11, we break the total structure factor into its constituent spin channels for the same densities and temperatures.

5.2.8 Exchange-correlation energy

Finally, we have evaluated the exchange-correlation energy E_{xc}, an essential quantity in any DFT formulation, defined

$$E_{xc}(T) \equiv E_{tot}(T) - E_0(T) \tag{5.57}$$

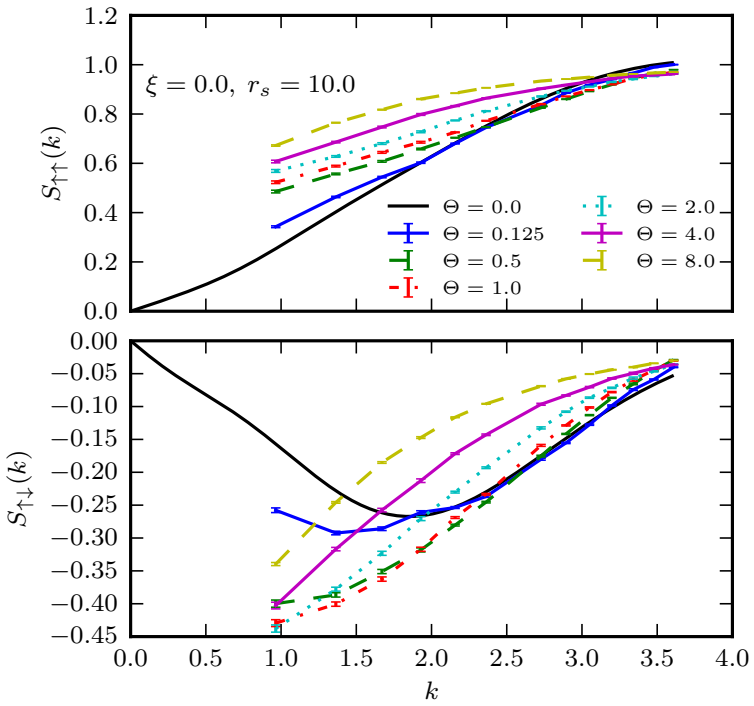

Figure 5.11: Static structure factors for each spin channel for $r_s = 10.0$ in the unpolarized state at several temperatures. At $\Theta = 0.0$ we plot the ground state structure factor from Ref. [48].

where E_0 is the kinetic energy of a free Fermi gas at temperature T. As is customary, we further break up E_{xc} into exchange and correlation parts,

$$E_{xc}(T) = E_x(T) + E_c(T) \tag{5.58}$$

where $E_x(T)$ is the Hartree-Fock exchange energy for a free Fermi gas at temperature T [3].

By calculating $E_{tot}(T)$ through RPIMC simulations we were able to determine $E_c(T)$ at all studied densities for both the fully spin-polarized and unpolarized states. As one can see in Fig. 5.12, correlation effects increase both with density (smaller r_s) and temperature up to a temperature above the Fermi temperature T_F. Above this temperature, the electron gas begins to be less correlated. This represents the point at which electron screening is a dominant effect, the interaction becomes effectively short-ranged, and the Debye-approximation becomes relatively accurate [52]. As the density increases, the value of Θ at which this occurs decreases. At $r_s = 1.0$ the maximal effect of interactions occurs very near T_F, $\Theta = 1$.

Most notably, we see a departure from the $\Theta = 0.0$ correlation energy used ubiquitously in both ground state and finite-temperature local density approximation DFT calculations. This discrepancy is significant

[3]Because the electron density is homogeneous, the Hartree-Fock and DFT orbitals are identical implying that the exchange energies in the two approximations are the same.

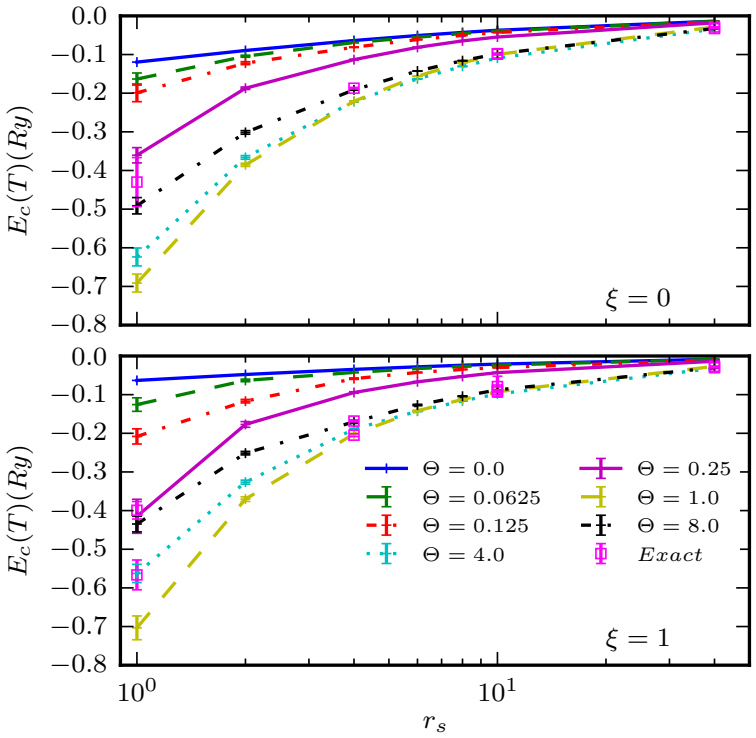

Figure 5.12: Correlation energy $e_c(T)$ of the $3D$ HEG at several temperatures and densities for the unpolarized (top) and fully spin-polarized (bottom) states. *Exact* (signful) calculations (squares) confirm the fixed-node results where possible ($\Theta = 8.0$ for $\xi = 0$ and $\Theta = 4.0, 8.0$ for $\xi = 1$). For comparison, we plot the $\Theta = 0.0$ correlation energy used in local density approximation DFT calculations.

throughout the warm-dense regime, calling into question the use of ground state correlation functionals at such temperatures and densities.

5.2.9 Conclusions

Through this comparison of our results against existing numerical and analytical data, we conclude the free-particle nodal approximation performs well for the densities studied. Further investigation is needed at even smaller values of r_s and lower temperatures in order to determine precisely where this approximation begins to fail. Such studies will necessarily require algorithmic improvements, however, because of difficulty in sampling paths at high density and low temperature, see Chapters 3.

In conclusion we have used RPIMC with free-particle nodes to calculate energies, pair correlation factors, and structure factors for the $3D$ HEG throughout the warm-dense regime. Systematic errors, including finite-size effects, time-step, and statistical fluctuations, are controlled for. Through cross-validation with previous ground-state and classical MC and exact finite-temperature calculations, we estimate that bias from the use of the free particle density matrix in the constraint is small for the density/temperature points simulated.

This does not exclude the possibility of fixed-node error at higher densities and lower temperatures. In future work we will quantify this error by finding better nodal structures and doing calculations without such uncontrolled approximations.

All data can be in a repository hosted at `http://github.com/3dheg/3DHEG`.

Chapter 6

Finite-temperature exchange-correlation functional

Density functional theory (DFT) is used ubiquitously in computational chemistry and condensed-matter physics [66]. Recently there has been intense interest in extending the success of ground-state DFT to finite-temperature systems such as stellar, planetary interiors and other hot dense plasmas [17, 26, 65]. However, such attempts have met both fundamental and technical barriers when electrons have significant correlations.

There are two broad approaches to building finite-temperature functionals, as discussed in Chapter 4. In one approach, the exact Mermin finite-T DFT is approximated by smearing the electronic density of states over a Fermi-Dirac distribution [78]. Although a useful approximation, this approach is not exact even in the limit of the exact ground state exchange functional as the Kohn-Sham orbitals need have no relation to the true excited states [60]. Additionally, as temperature increases, an ever-increasing number of molecular (Kohn-Sham) orbitals is required in order to evaluate the functional. This inevitably results in the DFT calculations becoming computationally intractable at some temperature. A second approach is to use Orbital-Free Density Functional Theory (OFDFT) where the usual Kohn-Sham orbitals are replaced by explicit density functionals for the kinetic energy and entropy terms [97,104]. However, an a priori way to determine such functionals has yet to materialize. Without a reliable benchmark, OFDFT has historically been left to rely on Thomas-Fermi-like approximations which can incur errors an order of magnitude larger than typical DFT errors [60]. Recently generalized gradient approximations have improved OFDFT, introducing higher accuracy orbital-free kinetic energy density functionals for both 0-T and finite-T, as well as an exchange-correlation density functional for 0-T [58]. Nevertheless, the field still lacks a high-accuracy, orbital-free exchange-correlation energy density functional for finite-T.

In Chapter 5 we provided accurate, first-principles thermodynamic data of the $3D$ homogeneous electron gas (HEG) throughout the warm-dense regime, making firm connections to both previous semi-classical and ground-state studies. In that work we utilized the Restricted Path Integral Monte Carlo (RPIMC) method described in Chapter 3. Now, we fit this data to a functional form for the exchange-correlation energy which obeys the exact limiting behavior in temperature and density.

In the first section of the chapter we use least squares regression fit finite-temperature path integral Monte

Carlo calculations of the exchange-correlation energy of the $3D$ finite-temperature homogeneous electron gas in the warm-dense regime ($r_s \equiv (3/4\pi n)^{1/3} a_B^{-1} < 40$ and $\Theta \equiv T/T_F > 0.0625$). In doing so, we construct a Padé approximant which collapses to Debye-Hückel theory in the high-temperature, low-density limit. Likewise, the zero-temperature limit matches the numerical results of ground-state quantum Monte Carlo, as well as analytical results in the high-density limit.

In the second section we apply our new finite-temperature functional to systems across huge ranges of temperature and density in an attempt to find where, if anywhere, the more precise temperature dependence affects the system. We specifically examine Aluminum where the largest discrepancies with previous results occur in the heart of the WDM regime.

6.1 Functional fitting

6.1.1 Asymptotic Limits

A satisfactory fit must match with known asymptotic limits. For the $3D$ HEG, analytic limits exist at high-temperature and low-density (the Debye-Hückel limit), and at zero-temperature.

In the Debye-Hückel (DH) limit, the quantum-mechanical Fermi-Dirac distribution may be approximated by the classical Boltzmann distribution, i.e. when $\Gamma \equiv 2/(r_s T) \ll 1$, where T is in Rydbergs and r_s is the Wigner-Seitz radius normalized by the Bohr radius. In this regime, the average potential energy per particle is much smaller than the thermal energy per particle, and each electron may be treated with a short-ranged, spherically-symmetric, screened interaction [31]. These approximations combined give the excess energy per particle to be $U_{DH} \equiv U - U_0 = -\frac{\sqrt{3}}{2}\Gamma^{3/2} T = -\sqrt{6} r_s^{-3/2} T^{-1/2}$, where U_0 is the energy of an ideal gas (classically) or of a free Fermi gas (quantum mechanically). Classical simulations have numerically extended these results to larger values of Γ [52, 92].

The first order quantum mechanical correction to these results is given through the Wigner-Kirkwood expansion in powers of $\hbar$, $U_Q = -\frac{\Gamma^3}{8} T^2 = -r_s^{-3} T^{-1}$. The next order correction as well as the first-order exchange correction have also been calculated explicitly [1, 51, 56]. Finally there has been some effort to calculate virial expansions of the excess energy at low-density and finite-temperature [3].

At zero-temperature, a significant body of numerical and analytical work has defined the exchange-correlation energy at all densities. In the high-density limit ($r_s \ll 1$) the total energy can be expressed as $E = a_1 r_s^{-2} + a_2 r_s^{-1} + a_3 \log r_s + a_4 + a_5 r_s \log r_s + a_6 r_s + \mathcal{O}(r_s^2 \log r_s)$. The first two coefficients can be determined through Hartree-Fock theory, with the first being the energy of a free Fermi gas and the second being the Fock exchange energy. Terms a_3 and a_4 were calculated by Gell-Mann and Brueckner [46]

using the random phase approximation (RPA). These results were extended by Carr and Maradudin [16] to determine a_5 and a_6. In the low-density limit ($r_s \gg 1$), one expects a body-centered cubic configuration, i.e. the Wigner crystal [108]. This suggests the form $E = A_1 r_s^{-1} + A_2 r_s^{-3/2} + A_3 r_s^{-2} + A_4 r_s^{-5/2} + \mathcal{O}(r_s^{-3})$ for the total energy. The first coefficient, the Madelung term, was first calculated by Fuchs [44]. The next three terms, coming from the zero-point harmonic vibration and its associated anharmonic corrections, were determined by Carr et al. [15].

High-precision quantum Monte Carlo (QMC) calculations have since spanned these two regimes [18, 22], paving the way for accurate parameterizations which leverage the foregoing limiting forms [88, 90, 106]. Such functionals have been integral to the development and expansion of the local density approximation (LDA) of zero-temperature DFT [67].

6.1.2 Prior Fits

Several attempts have been made at extending the success of ground state DFT to finite-temperature and this has resulted in the creation of a number of finite-temperature parameterizations of the exchange-correlation energy [29, 36, 91, 100]. A basic approach is the random phase approximation (RPA), which is accurate in the low-density, high-temperature limit (where it reduces to DH) and the low-temperature, high-density limit, since these are both weakly interacting regimes. Its failure, however, is most apparent in its estimation of the equilibrium, radial distribution function $g(r)$ which becomes unphysically negative for stronger coupling [36].

Extensions of the RPA into intermediate densities and temperatures have largely focused on constructing local-field corrections (LFC) through interpolation since diagrammatic resummation techniques often become intractable in strongly-coupled regimes. Singwi *et. al.* [95] introduced one such strategy relying on two assumptions. First, they use the static polarization-potential approximation allowing one to write the LFC, $G(k, \omega) \simeq G(k, \omega = 0) \equiv G(k)$. Next they assume the two-particle distribution function is a function of the Fourier transformed momentum distribution, $n(r)$, and the pair-correlation function, $g(r)$, allowing a self-consistent solution for $G(k)$. Tanaka and Ichimaru [100] (TI) extended this method to finite-temperatures and provided the parameterization of the $3D$ HEG correlation energy shown in Figs. 6.1 and 6.2. A similar method by *Dandrea et. al.* uses the Vashista-Singwi LFC [29] to interpolate between the high- and low-temperature limits. Both methods appear to perform marginally better than the RPA at all temperatures, though both still fail to produce a positive-definite $g(r)$ at values of $r_s > 2$.

A third, more recent approach introduced by Perrot and Dharma-wardana (PDW) [91] relies on a classical mapping wherein the distribution functions of a classical system at temperature T_{cf}, solved for through the hypernetted-chain equation, reproduce those for a quantum system at temperature T. In a previous work,

PDW showed such a temperature T_q existed for the classical system to reproduce the correlation energy of the quantum system at $T = 0$ [32]. To extend that work to finite-temperature quantum systems, they use the simple interpolation formula $T_{cf} = \sqrt{T^2 + T_q^2}$. This interpolation is clearly valid in the low-T limit where Fermi liquid theory gives the quadratic dependence [43] of the energy on T. Further in the high-T regime, T dominates over T_q as the system becomes increasingly classical.

6.1.3 Present Fit

For our fit to RPIMC data, we employ a similar fitting functional as was used by PDW. To this end we define,

$$E_{xc}(r_s, T) \equiv \frac{E_{xc}(r_s, 0) - P_1}{P_2} \tag{6.1}$$

where $E_{xc}(r_s, 0)$ is the ground-state exchange-correlation energy,

$$P_1 \equiv (A_2 u_1 + A_3 u_2)T^2 + A_2 u_2 T^{5/2}, \tag{6.2}$$

$$P_2 \equiv 1 + A_1 T^2 + A_3 T^{5/2} + A_2 T^3, \tag{6.3}$$

$$u_1(r_s) \equiv \frac{1}{r_s^3}, \tag{6.4}$$

$$u_2(r_s) \equiv \frac{\sqrt{6}}{r_s^{3/2}}, \tag{6.5}$$

and

$$A_k(r_s) \equiv \exp\left[a_k \log r_s + b_k + c_k r_s + d_k r_s \log r_s\right]. \tag{6.6}$$

Here u_1 and u_2 are chosen such that $\lim_{T\to\infty} E_{xc}(r_s, T) = U_{DH} + U_Q + \mathcal{O}(T^{-3/2})$. The higher-order terms reflect the higher-order quantum corrections mentioned above. Likewise, note that $\lim_{T\to 0} E_{xc}(r_s, T) = E_{xc}(r_s, 0) - \mathcal{O}(T^2)$, reproducing both the ground-state exchange-correlation energy of Ceperley-Alder [22] and the small-T quadratic behavior of Fermi liquid theory. Fitting exchange and correlation together avoids the canceling $T^2 \log T$ term coming from both. The Perdew-Zunger [88] parametrization is used throughout for $E_{xc}(r_s, 0)$. The exchange-correlation energy between this and other parameterizations is at least two orders of magnitude smaller than the difference between the lowest temperature simulated and the Perdew-Zunger result. Because of this, we expect the use of another 0-T functional to have negligible effect on the

Table 6.1: Fit parameters of the function in (6.6) for the unpolarized ($\xi = 0$) gas. The top table corresponds to $r_s < 10$, while the bottom table corresponds to $10 < r_s$.

k	a_k	b_k	c_k	d_k
1	6.94759	−0.34608	−1.97251	0.53700
2	7.70107	−0.95154	−1.80401	0.49086
3	12.68820	−1.59703	−4.74435	1.23569
1	1.54712	−1.97814	1.42976	−0.32967
2	2.65068	−2.45160	1.36907	−0.31701
3	3.07192	−4.65269	1.36324	−0.32247

Table 6.2: Fit parameters of the function in (6.6) for the polarized ($\xi = 1$) gas. The top table corresponds to $r_s < 10$, while the bottom table corresponds to $10 < r_s$.

k	a_k	b_k	c_k	d_k
1	0.63136	−10.58837	5.64356	−1.74378
2	−2.10145	−11.68122	7.92233	−2.33584
3	3.31926	−11.73144	4.49236	−1.44466
1	24.77079	−6.69224	−8.44165	1.79020
2	31.18076	−9.82004	−10.33823	2.18557
3	22.83940	−6.90395	−7.45133	1.58075

finite-T parametrization we present.

We determine the best parameters of (6.6) through a least squares fitting of RPIMC data. The RPIMC data shows a qualitative change in behavior around $r_s \approx 10$ and so we divide the fitting regime into two parts, $r_s < 10$ and $r_s > 10$. At $r_s = 10$, we make sure both the functional and its derivative are continuous. This is accomplished by ensuring each factor A_k and its respective r_s derivative is continuous at $r_s = 10$, providing 6 constraints and leaving 18 free parameters. For the unpolarized gas $\xi = 0$, we give the parameters in Table 6.1. Using these values, the fitting function has a maximum relative error of 14%. For the polarized gas $\xi = 0$, we give the parameters in Table 6.2. Using these values, the fitting function has a maximum relative error of 18%. Both of these maximum deviations occur at $r_s = 1.0$ where errors from RPIMC simulation were largest. For lower densities for both the polarized and unpolarized gas, most relative errors are less than 1%. For completeness, we provide the relative error for each density and polarization for the fitting parameters in Tables 6.3 and 6.4. All energies are in units of Rydbergs.

6.1.4 Discussion and Conclusions

In Figs. 6.1 and 6.2, we plot our fit, the RPIMC data, and all mentioned prior fits of the finite-temperature exchange-correlation energy. Clearly, the classical Debye-Hückel limit is obeyed by each fit. However, only our fit and PDW obey the correct zero-temperature behavior ($E_{xc}(\Theta)/E_{xc}(0) \to 1$ as $\Theta \to 0$). The STLS

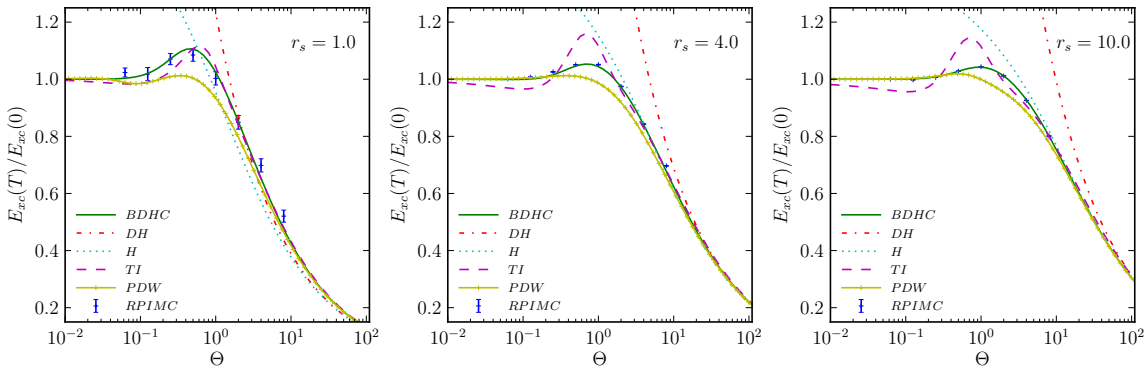

Figure 6.1: Ratio of the exchange-correlation energy E_{xc} at temperature T to that at $T = 0$ for the unpolarized $\xi = 0$ $3D$ HEG with $r_s = 1.0$, 4.0, and 10.0 (respectively). Shown are the results from numerical calculations (RPIMC), the present parameterization (BDHC), and several previous parameterizations. The latter include Debye-Hückel (DH), Hansen (H), Tanaka and Ichimaru (TI), and Perrot and Dharma-wardana (PDW), all of which are discussed in the text.

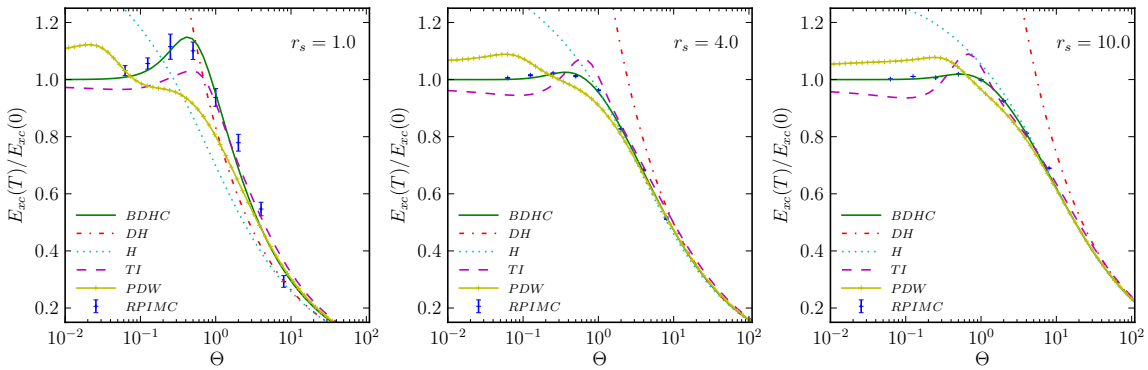

Figure 6.2: Ratio of the exchange-correlation energy E_{xc} at temperature T to that at $T = 0$ for the polarized $\xi = 1$ $3D$ HEG with $r_s = 1.0$, 4.0, and 10.0 (respectively). Shown are the results from numerical calculations (RPIMC), the present parameterization (BDHC), and several previous parameterizations. The latter include Debye-Hückel (DH), Hansen (H), Tanaka and Ichimaru (TI), and Perrot and Dharma-wardana (PDW), all of which are discussed in the text.

Table 6.3: Relative percentage error for the fit for the unpolarized gas, $\xi = 0$

r_s	Θ	% error of fit	% error of data
1.0	0.0625	2.180	1.478
1.0	0.1250	0.995	2.178
1.0	0.2500	3.033	1.780
1.0	0.5000	1.478	1.941
1.0	1.0000	4.110	2.243
1.0	2.0000	1.785	2.722
1.0	4.0000	11.430	3.200
1.0	8.0000	14.464	3.919
2.0	0.0625	1.077	0.488
2.0	0.1250	0.518	0.694
2.0	0.2500	1.149	0.566
2.0	0.5000	0.180	0.770
2.0	1.0000	1.514	0.742
2.0	2.0000	0.443	0.944
2.0	4.0000	3.933	1.134
2.0	8.0000	7.291	1.424
4.0	0.0625	0.197	0.234
4.0	0.1250	0.703	0.249
4.0	0.2500	1.217	0.264
4.0	0.5000	0.267	0.323
4.0	1.0000	0.048	0.336
4.0	2.0000	0.036	0.463
4.0	4.0000	1.108	0.516
4.0	8.0000	4.422	0.540
6.0	0.0625	0.564	0.136
6.0	0.1250	0.109	0.159
6.0	0.2500	0.149	0.241
6.0	0.5000	0.267	0.208
6.0	1.0000	0.224	0.221
6.0	2.0000	0.766	0.300
6.0	4.0000	0.278	0.331
6.0	8.0000	1.555	0.342
8.0	0.0625	0.257	0.088
8.0	0.1250	0.114	0.115
8.0	0.2500	0.009	0.183
8.0	0.5000	0.526	0.165
8.0	1.0000	0.359	0.164
8.0	2.0000	0.029	0.218
8.0	4.0000	0.108	0.244
8.0	8.0000	0.745	0.249
10.0	0.0625	0.087	0.070
10.0	0.1250	0.213	0.089
10.0	0.2500	0.166	0.103
10.0	0.5000	0.198	0.131
10.0	1.0000	0.070	0.126
10.0	2.0000	0.133	0.140
10.0	4.0000	0.409	0.192
10.0	8.0000	0.015	0.197
40.0	0.0625	0.048	0.008
40.0	0.1250	0.003	0.014
40.0	0.2500	0.001	0.033
40.0	0.5000	0.325	0.019
40.0	1.0000	0.556	0.019
40.0	2.0000	0.974	0.021
40.0	4.0000	1.172	0.025
40.0	8.0000	0.831	0.047

driven fit of Tanaka and Ichimaru (TI) only agrees well with the RPIMC data at high-density – i.e. where the RPA, the basis of STLS, is most applicable.

The PDW line in Figs. 6.1 and 6.2 clearly matches well with the RPIMC results in both temperature limits. It is not surprising, however, that in the intermediate temperature regime, where correlation effects are greatest, the quadratic interpolation of the temperature fails. A similar approach by Dutta and Dufty [36] uses the same classical mapping as PDW, matching the $T = 0$ pair correlation function instead of the correlation energy. While this gives accurate results near $T = 0$, the breakdown of Fermi liquid behavior near the Fermi temperature causes the method to overestimate the exchange hole of the pair correlation function. A direct comparison of E_{xc} is not yet available.

Finally we note that there has been some previous work on the low-density phases of $3D$ HEG both at $T = 0$ [110] and $T > 0$ [57]. These include a predicted second-order transition to a partially polarized state

Table 6.4: Relative percentage error for the fit for the polarized gas, $\xi = 1$

r_s	Θ	% error of fit	% error of data
1.0	0.0625	2.606	1.392
1.0	0.1250	3.523	1.525
1.0	0.2500	4.129	3.242
1.0	0.5000	2.250	2.285
1.0	1.0000	0.157	2.699
1.0	2.0000	16.504	3.102
1.0	4.0000	18.257	3.544
1.0	8.0000	5.723	5.727
2.0	0.0625	0.394	0.535
2.0	0.1250	4.181	0.696
2.0	0.2500	1.413	1.139
2.0	0.5000	1.720	0.914
2.0	1.0000	4.856	1.025
2.0	2.0000	0.266	1.210
2.0	4.0000	9.146	1.334
2.0	8.0000	9.546	1.612
4.0	0.0625	0.562	0.218
4.0	0.1250	1.292	0.589
4.0	0.2500	0.915	0.589
4.0	0.5000	0.827	0.539
4.0	1.0000	0.013	0.488
4.0	2.0000	0.225	0.478
4.0	4.0000	2.251	1.084
4.0	8.0000	0.829	2.453
6.0	0.0625	0.287	0.145
6.0	0.1250	0.732	0.416
6.0	0.2500	0.445	0.413
6.0	0.5000	0.877	0.510
6.0	1.0000	0.608	0.635
6.0	2.0000	0.364	0.762
6.0	4.0000	1.113	0.684
6.0	8.0000	7.034	1.333
8.0	0.0625	0.068	0.139
8.0	0.1250	0.733	0.333
8.0	0.2500	0.398	0.300
8.0	0.5000	0.553	0.382
8.0	1.0000	0.231	0.454
8.0	2.0000	0.323	0.573
8.0	4.0000	0.119	0.502
8.0	8.0000	5.315	0.948
10.0	0.0625	0.161	0.093
10.0	0.1250	0.944	0.207
10.0	0.2500	0.184	0.236
10.0	0.5000	0.050	0.170
10.0	1.0000	0.238	0.369
10.0	2.0000	0.445	0.454
10.0	4.0000	0.084	0.400
10.0	8.0000	3.403	0.735
40.0	0.0625	0.358	0.027
40.0	0.1250	0.119	0.038
40.0	0.2500	0.329	0.056
40.0	0.5000	0.051	0.053
40.0	1.0000	0.119	0.093
40.0	2.0000	0.001	0.108
40.0	4.0000	0.097	0.114
40.0	8.0000	0.220	0.192

around $r_s \simeq 50$, and a first-order transition into a Wigner-crystal for $r_s > 100$. Since both these transitions are outside the range of the fit data, we do not expect to see these transitions with the above functional.

In summary we have performed a least squares fitting of recent RPIMC data to a functional form which reproduces both high- and low-temperature asymptotic limits exactly. This fit outperforms all previous attempts at parameterizing the exchange-correlation energy at arbitrary temperature. We are providing a simple script of the functional in the Supplementary Material as well as at `http://github.com/3dheg/BDHC`. It is our hope that this newly created parameterization will be useful as a basis for new finite-temperature DFT functionals and as a benchmark for orbital-free DFT studies.

6.2 Alternative Fit

Soon after our original fit presented above, another group fit the same data through a different quantity [59]. Instead of directly fitting the exchange-correlation energy, this group fits the per particle interaction energy defined as,

$$e_{int} \equiv \frac{1}{N}\langle V(R,R')\rangle. \tag{6.7}$$

We note that this differs from what is typically defined as the potential energy in PIMC calculations, the β derivative of the potential action,

$$e_{\mathcal{U}} \equiv \frac{1}{N}\langle \frac{\partial \mathcal{U}(R,R')}{\partial \beta}. \tag{6.8}$$

Nevertheless, we still measured it and provided it to the group for their use. The per particle interaction energy can be conveniently related to the per particle exchange-correlation free energy as [96]

$$f_{xc}(r_s,\Theta) = \frac{1}{r_s^2}\int_0^{r_s} dr_s' r_s' e_{int}(r_s,\Theta). \tag{6.9}$$

To arrive back at the per particle exchange-correlation energy, we simply use the relation $f_{xc} = e_{xc} - Ts_{xc}$ where the entropic contribution to the exchange-correlation free energy s_{xc} may be defined as

$$s_{xc} = -\frac{1}{T}\frac{\partial f_{xc}(r_s,\Theta)}{\partial \Theta}\ |_{r_s}\ . \tag{6.10}$$

Thus we arrive back at the per particle exchange-correlation energy as

$$e_{xc} = f_{xc} - \frac{1}{T}\frac{\partial f_{xc}(r_s,\Theta)}{\partial \Theta}\ |_{r_s}\ . \tag{6.11}$$

The fit for f_{xc} is given also as a Padé approximant, only now resembling the form of Tanaka and Ichimaru [100],

$$f_{xc}^{\xi}(r_s,\Theta) = -\frac{1}{r_s}\frac{w_{xi}a(\Theta) + b_{xi}(\Theta)r_s^{1/2} + c_{xi}(\Theta)r_s}{1 + d_{\xi}(\Theta)r_s^{1/2} + e_{\xi}(\Theta)r_s} \tag{6.12}$$

Table 6.5: Fit parameters of the functions in (6.12) for the unpolarized ($\xi = 0$) and polarized ($\xi = 1$) gases.

	$\xi = 0$	$\xi = 1$
b_1	0.283997	0.329001
b_2	48.932154	111.598308
b_3	0.370919	0.537053
b_4	61.095357	105.086663
b_5	0.871837	1.590438
c_1	0.870089	0.848930
c_2	0.193077	0.167952
c_3	2.414644	0.088820
d_1	0.579824	0.551330
d_2	94.537454	180.213159
d_3	97.839603	134.486231
d_4	59.939999	103.861695
d_5	24.388037	17.750710
e_1	0.212036	0.153124
e_2	16.731249	19.543945
e_3	28.485792	43.400337
e_4	34.028876	120.255145
e_5	17.235515	15.662836

where the coefficients are defined as

$$a(\Theta) = 0.610887 \tanh\left(\frac{1}{\Theta}\right) \frac{0.75 + 3.04363\Theta^2 0.09227\Theta^3 + 1.7035\Theta^4}{1 + 8.31051\Theta^2 + 5.1105\Theta^4} \tag{6.13}$$

$$b(\Theta) = \tanh\left(\frac{1}{\sqrt{\Theta}}\right) \frac{b_1 + b_2\Theta^2 + b_3\Theta^4}{1 + b_4\Theta^2 + b_5\Theta^4} \tag{6.14}$$

$$c(\Theta) = [c_1 + c_2 \exp\left(\frac{c_3}{\Theta}\right)] e(t) \tag{6.15}$$

$$d(\Theta) = \tanh\left(\frac{1}{\sqrt{\Theta}}\right) \frac{d_1 + d_2\Theta^2 + d_3\Theta^4}{1 + d_4\Theta^2 + d_5\Theta^4} \tag{6.16}$$

$$e(\Theta) = \tanh\left(\frac{1}{\Theta}\right) \frac{d_1 + e_2\Theta^2 + e_3\Theta^4}{1 + e_4\Theta^2 + e_5\Theta^4} \tag{6.17}$$

with the parameters given in Table 6.5.

For the temperatures and densities simulated in Chapter 5, both our fit and this new fit perform very similarly. However, because they were fitting into the exchange-correlation free energy f_{xc}, an additional analytic limit was available as an anchor point. Specifically, the small r_s limit of f_{xc} is known to become only the exchange term f_x defined as,

$$lim_{r_s \ll 1} f_{xc}(r_s, \Theta) = f_x(r_s, \Theta) = -\frac{w_\xi}{r_s} a(\Theta) \tag{6.18}$$

and is reached exactly by the functional form [100]. Consequently, in the small r_s limit, beyond where

simulation data is currently available ($r_s < 1$), this fit may be slightly more representative of the real HEG exchange-correlation energy.

6.3 Effect of finite-temperature functionals

Now that we have an accurate finite-temperature parametrization of the electron liquid correlation energy, we can implement it in actual finite-temperature DFT codes. After doing so, we attempt to see where, if anywhere, there are deviations with the original calculation method that relied on only zero-temperature exchange-correlation energies. Here we apply both new functionals to a wide range of temperatures and densities of atomic Al.

6.3.1 Method

We employ the finite-temperature average atom DFT code *PURGATORIO*. It differs from other DFT formulations in that it treats explicitly only a single atom up to the Wigner-Seitz radius. Beyond this point, analytic forms are used to solve the Kohn-Sham integrals, effectively breaking up the calculation into bound and continuum regions. For a review of this method, see Ref. [109].

To make this code integrate both new finite-temperature functionals, we simply replace the routine that calls the zero-temperature exchange-correlation energy functional. The total exchange-correlation energy is then the usual sum over orbital occupations. Since this is all we do, the finite-temperature exchange-correlation form of the entropy remains unchanged, only shifted by the shift is occupations due to the new exchange-correlation energy functionals. In a true implementation of finite-temperature LDA, the entropy piece would be replaced by the real HEG finite-temperature entropy, which is the goal of the OFDFT community. Nevertheless, by only swapping the exchange-correlation energy, we can distill its solitary effect on finite-temperature thermodynamic quantities.

6.3.2 Application to Al

We run simulations across a large temperature-density range with three exchange-correlation functionals: zero-temperature Perdew-Zunger (PZ) [88] where finite-temperature effects are captured exclusively through the density of states summation technique, our fit (BHDC), and the alternative fit (KSDT) [59]. As a first attempt to ascertain the discrepancy between them, we look at their respective total energies. In Fig. 6.3, we plot the total energy for all three functionals applied to Al. A clear feature of this plot is the block-like structure of the energy in temperature and density. The diagonal of this block corresponds roughly to a

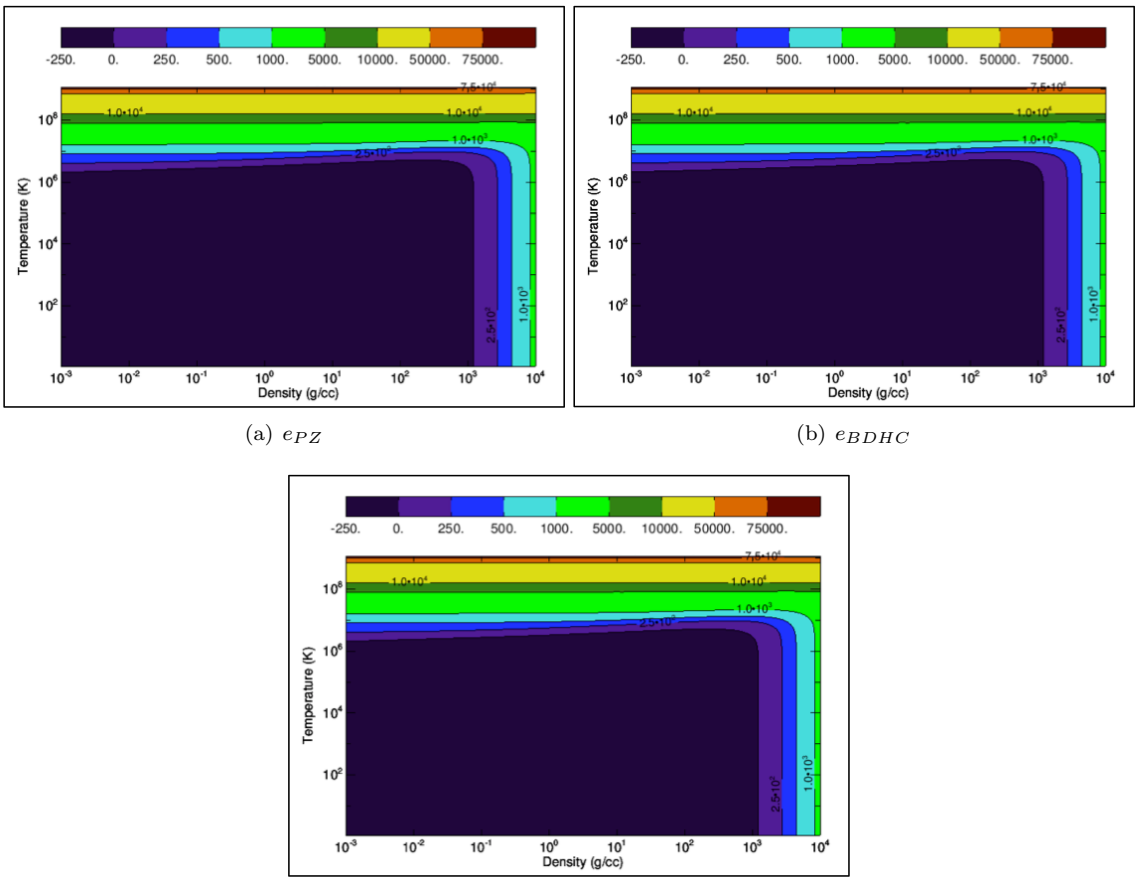

(a) e_{PZ} (b) e_{BDHC}

(c) e_{KSDT}

Figure 6.3: Per particle internal energies of a system of Al at various densities and temperatures, each with a different finite-temperature functional: (a) zero-temperature Perdew-Zunger [88], (b) our fit presented in this chapter (BDHC), and (c) the alternative fit presented in this chapter (KSDT) [59].

consistent value of the Fermi temperature, specifically the electron degeneracy parameter $\Theta \equiv T/T_F = 1$.

From the per particle internal energy plots alone it is difficult to see any difference, so in Fig. 6.4, we plot the energy difference between the two finite-temperature functionals and their respective energy difference with the zero-temperature functional. We see that here there is a clear discrepancy with the zero-temperature functional results. Above the same $\Theta = 1$ line discussed in 6.3, percent differences with PZ range from $\sim$ %1 to $>$ %50, increasing with higher temperatures and densities. This corresponds to the point in the PIMC study of the electron gas that we found the largest deviations from the ground state exchange-correlation energy.Likewise, we saw these deviations grow with increased density. Between the two new functions, there are small discrepancies at large density. This is likely due to poor limiting behavior of the BDHC functional at points with electron Wigner-Seitz radius $r_s < 1.0$. Nevertheless, the significant contrast with the PZ functional is consistent between the two new finite-temperature functional forms.

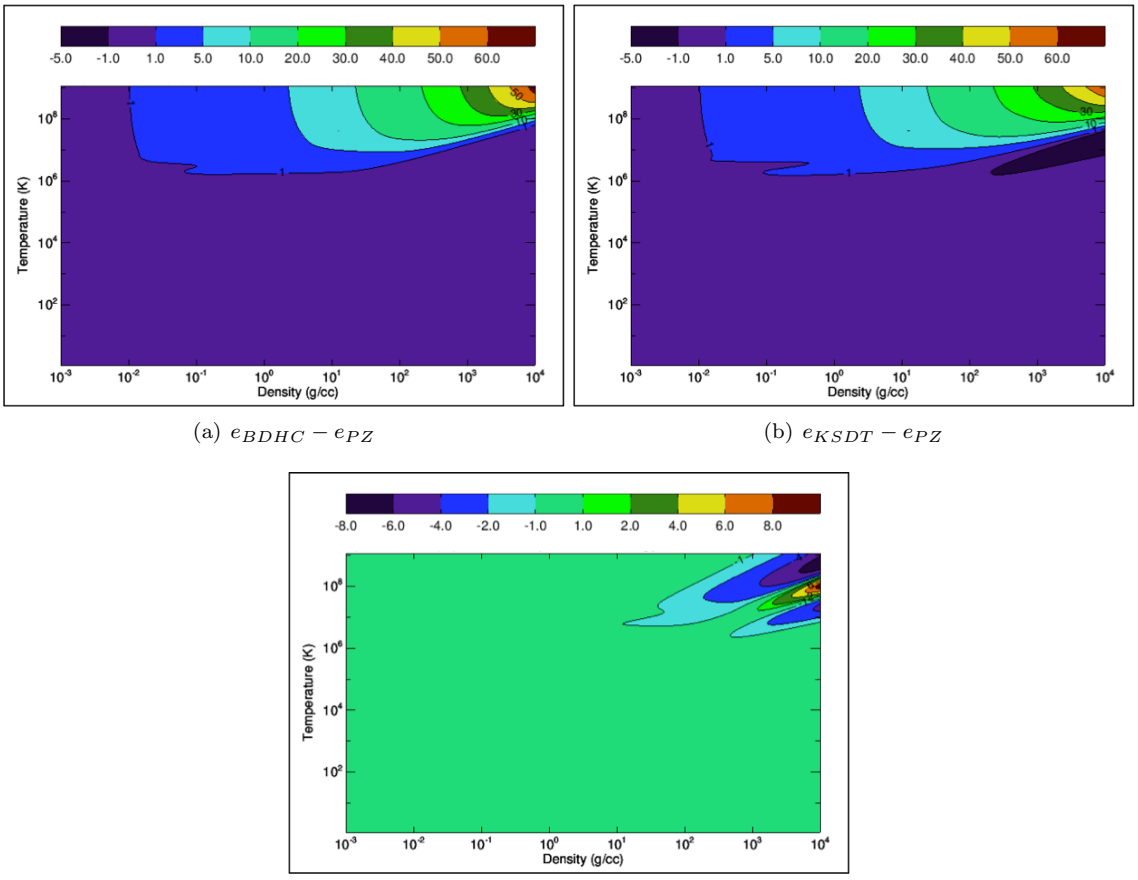

(a) $e_{BDHC} - e_{PZ}$

(b) $e_{KSDT} - e_{PZ}$

(c) $e_{BDHC} - e_{KSDT}$

Figure 6.4: Differences of the per particle internal energy of a system of Al at various densities and temperatures between different finite-temperature functionals: (a) our fit and zero-temperature Perdew-Zunger [88], (b) the alternative fit present in this chapter (KSDT) [59] and zero-temperature Perdew-Zunger [88], and (c) our fit presented in this chapter (BDHC) and the alternative fit presented in this chapter (KSDT) [59].

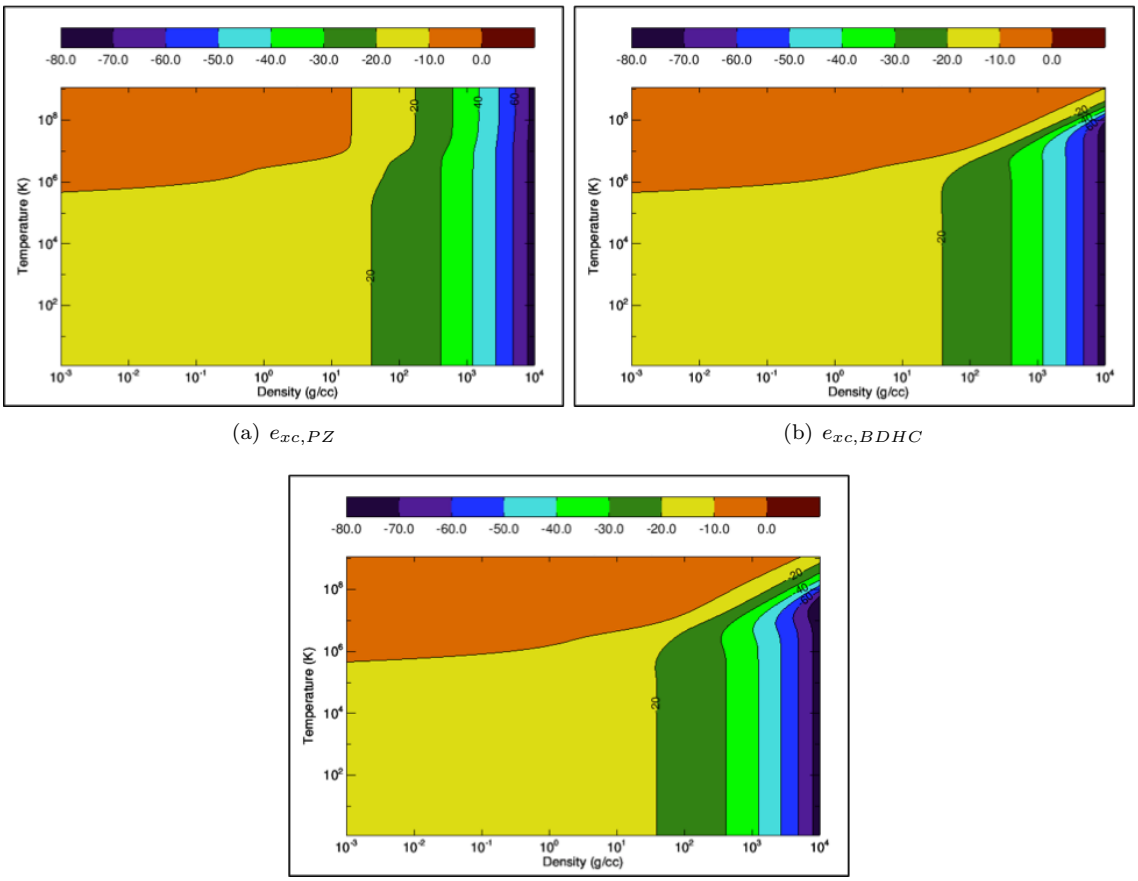

(a) $e_{xc,PZ}$

(b) $e_{xc,BDHC}$

(c) $e_{xc,KSDT}$

Figure 6.5: Per particle exchange-correlation energies of a system of Al at various densities and temperatures, each with a different finite-temperature functional: (a) zero-temperature Perdew-Zunger [88], (b) our fit presented in this chapter (BDHC), and (c) the alternative fit presented in this chapter (KSDT) [59].

The source of these differences can be seen in the measured exchange-correlation energies, which we plot in Fig. 6.5. We see that along the same $\Theta = 1$ line, the exchange-correlation energy has a qualitative change between the zero- and finite-temperature functionals. Specifically, again at high temperature and density, the finite-temperature functional E_{xc} maintains a near constant value along the $\Theta = 1$ line, while the zero-temperature functional does not. In the HEG exchange-correlation data, we see the largest discrepancies with the zero-temperature HEG at high densities around the Fermi temperature. We speculate that this is translated to the deviant behavior seen in the plots of the per particle exchange-correlation energy of Al.

To create a physical picture of the observed energy differences, we examine another quantity, the effective atomic number Z_{eff}. In the average atom method, there are three different measures of this quantity, corresponding to three separate definitions. First we define Z_{WS} as the charge density on the Wigner-Seitz sphere boundary, n_{WS}, and assume a constant conduction charge density of this value in the entire Wigner

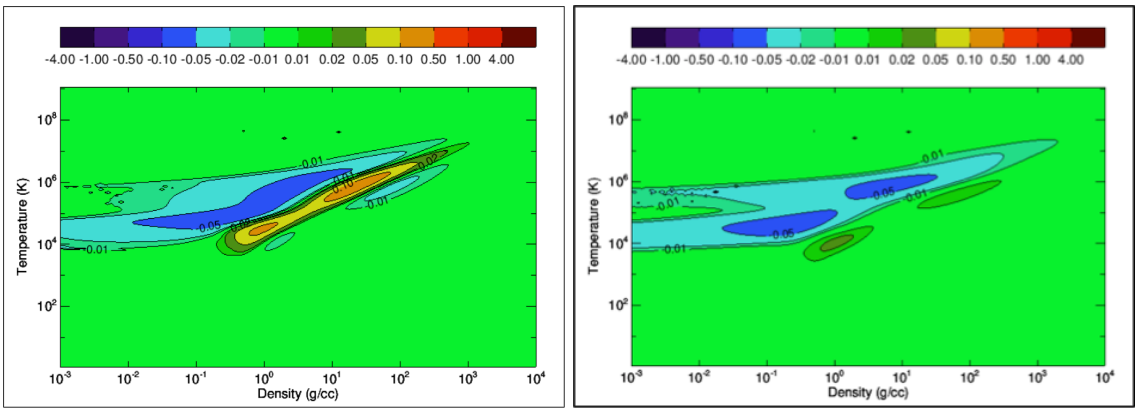

(a) $Z_{WS,BDHC} - Z_{WS,PZ}$ (b) $Z_{WS,KSDT} - Z_{WS,PZ}$

Figure 6.6: Difference for the effective atomic number Z_{WS} defined in 6.19 between the zero-temperature Perdew-Zunger functional finite-temperature functionals: (a) our fit presented in this chapter (BDHC) and (b) the alternative fit presented in this chapter (KSDT) [59].

Seitz sphere of radius R. Then

$$Z_{WS} = 4\pi R^3 n_{WS}/3. \tag{6.19}$$

Next, we define a continuum effective atomic number Z_{cntm} by first computing the number of bound electrons, Z_{bound}, that contribute to the charge density in the Wigner-Seitz sphere. Then the number of continuum electrons, and hence the effective Z is

$$Z_{cntm} = Z - Z_{bound}. \tag{6.20}$$

Finally, we define Z_{back} through the density of the electron gas n_{back} that gives the same chemical potential at the same temperature as the atom-in-jellium electronic structure calculation. Then the effective Z is n_{back} multiplied by the density by the Wigner-Seitz sphere volume,

$$Z_{back} = 4\pi R^3 n_{back}/3. \tag{6.21}$$

Similar to the energy, a naive plot of the average value of Z_{eff} will show little qualitative difference between the three functionals. Thus in Figs. 6.6, 6.7, and 6.8, we plot the difference in Z_{eff} between the finite-temperature functionals and the zero-temperature PZ functional. All three plots show clear deviations along the same $\Theta = 1$ line, though now there are some additional features. Since Z_{eff} is intimately related to the ionization of electrons, we suspect these extra discrepancies arise due to a shifting of the ionization edge. This is seen especially clearly for Z_{cntm}, which literally counts the number of bound electrons. Fig. 6.7 shows

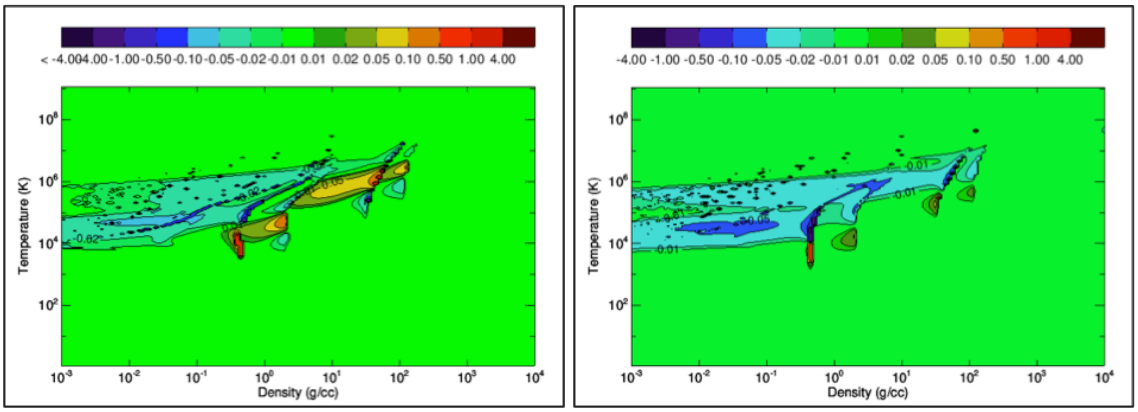

(a) $Z_{cntm,BDHC} - Z_{cntm,PZ}$ (b) $Z_{cntm,KSDT} - Z_{cntm,PZ}$

Figure 6.7: Difference for the effective atomic number Z_{cntm} defined in 6.20 between the zero-temperature Perdew-Zunger functional finite-temperature functionals: (a) our fit presented in this chapter (BDHC) and (b) the alternative fit presented in this chapter (KSDT) [59].

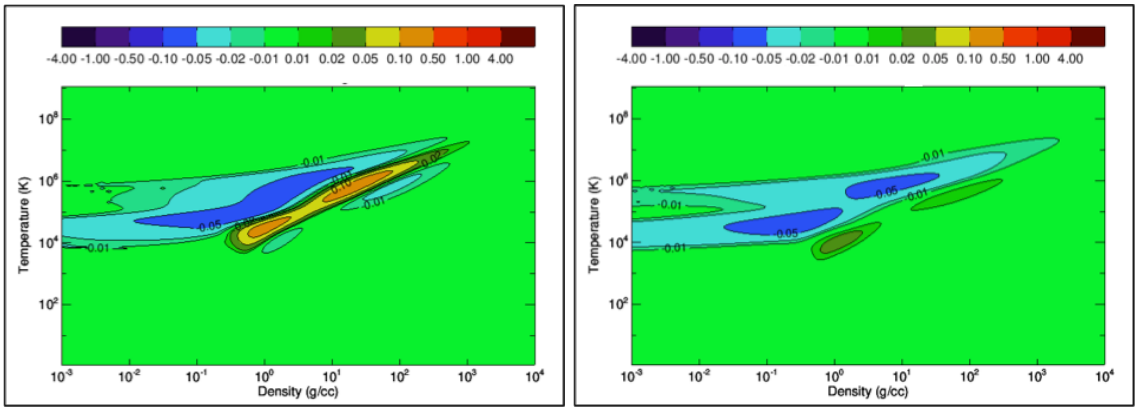

(a) $Z_{back,BDHC} - Z_{back,PZ}$ (b) $Z_{back,KSDT} - Z_{back,PZ}$

Figure 6.8: Difference for the effective atomic number Z_{back} defined in 6.21 between the zero-temperature Perdew-Zunger functional finite-temperature functionals: (a) our fit presented in this chapter (BDHC) and (b) the alternative fit presented in this chapter (KSDT) [59].

that for Z_{cntm} there are lines of difference between the finite-temperature and zero-temperature functionals corresponding to where different orbitals are ionizing. In Z_{WS} and Z_{back}, these edges are smoothed over a range of densities and temperatures due to their definition. Nevertheless, if we look at the average orbital occupations for Z_{WS} and Z_{back}, we see a difference between the two finite-temperature functionals and PZ. Finally between the BDHC and KSDT, there is some discrepancy in Z_{eff}, albeit an order of magnitude smaller than that with PZ. Again, we assume this is due to the difference between the two functionals in treating the small r_s (large density) limit.

Much more is left to done in quantifying the effect of finite-temperatures to the exchange-correlation functionals of inhomogeneous systems. As a first step, we aim to recreate the above study for several different elements of varying atomic number Z. Because we see a larger discrepancy between the ground state and finite-temperature HEG at higher densities, it may be that an atom with an atomic number greater than that of Al will have larger discrepancies. On the other hand, something like a hydrogen gas may be more qualitatively similar to an electron gas since its energy scale is close to that of the bare HEG. It would also be interesting to compare the above results to those of an OFDFT calculation that included finite-temperature exchange-correlation explicitly through the free energy. In this way, the entropic contribution will be accounted for at the same level as the exchange-correlation energy. Finally, it will be necessary to perform a benchmark study of a system with reliable experimental or PIMC data, in order to assess if including finite-temperature effects more accurately actually leads to more accurate results.

Chapter 7

Variational optimization of nodes

As mentioned in Chapter 3, the fixed-node approximation is the only uncontrolled approximation in our implementation of the PIMC method for fermions. A route to circumvent or control this approximation would represent a large step forward in creating a truly exact method. In the proceeding chapter, we present such a method which leverages the variational principle in the free energy for systems at finite-temperature.

7.1 Computing free energy differences

At zero temperature, it is well known that there exists a variational principle in the total energy of the system. In fact, we used this principle in Chapter 4 to derive ground state DFT. Ground state QMC also relies on this variational principle to minimize the energy of a trial wavefunction. Specifically, for zero-temperature QMC simulations of fermions, the fixed-node constraint can be optimized by tweaking the trial wave function's nodes to give the lowest possible energy [25]. In this way, zero-temperature QMC can discern between competing phases simply by finding which phase has the lowest energy.

In finite-temperature QMC, this has yet to be realized since the variational principle now only applies to the system's free energy [43]. Direct calculation of a system's absolute free energy can not be efficiently calculated in a single PIMC simulation for a single temperature and density. Thus, up until now, it was necessary to perform an integration over some constant coupling two systems. For example, if we take two systems with Hamiltonians $\hat{\mathcal{H}}_A$ and $\hat{\mathcal{H}}_B$, we may define a third Hamiltonian

$$\hat{\mathcal{H}}(\alpha) \equiv \hat{\mathcal{H}}_A + \alpha(\hat{\mathcal{H}}_B - \hat{\mathcal{H}}_A) \tag{7.1}$$

where α is a constant ranging from 0 to 1. The free energy of a system with this Hamiltonian can be written

$$F(\alpha) = -\frac{1}{\beta} \ln \mathcal{Z}(\alpha) \tag{7.2}$$

$$= -\frac{1}{\beta} \ln [\mathrm{Tr}\, e^{-\beta \hat{\mathcal{H}}(\alpha)}]. \tag{7.3}$$

Now if we want the difference in free energy between the two systems A and B, we may use the first law of calculus and take

$$\begin{aligned} F_A - F_B &= \int_0^1 d\alpha \frac{\partial F(\alpha)}{\partial \alpha} && (7.4) \\ &= \int_0^1 d\alpha \frac{\partial}{\partial \alpha}(-\frac{1}{\beta}\ln[\mathrm{Tr}\, e^{-\beta\hat{\mathcal{H}}(\alpha)}]) && (7.5) \\ &= \int_0^1 d\alpha \frac{\mathrm{Tr}[e^{-\beta\hat{\mathcal{H}}(\alpha)}\frac{\partial\hat{\mathcal{H}}(\alpha)}{\partial\alpha}]}{\mathrm{Tr}\, e^{-\beta\hat{\mathcal{H}}(\alpha)}} && (7.6) \\ &= \int_0^1 d\alpha \langle \frac{\partial\hat{\mathcal{H}}(\alpha)}{\partial\alpha}\rangle_\alpha && (7.7) \\ &= \int_0^1 d\alpha \langle \hat{\mathcal{H}}_B - \hat{\mathcal{H}}_A\rangle_\alpha. && (7.8) \end{aligned}$$

The final quantity can be recognized to be the average difference in energy between systems A and B within supersystem α. Choosing the quantity that α represents depends on what is already known about the limits of the systems. If, for example, we take A to be a free system, and B to be the same system with interactions, then α can represent the potential coupling constant. On the other hand, if we take A to be the classical analogue of system B, then the integration over α can represent an integration over inverse temperature from the classical limit, down to inverse temperature β. The latter choice is the originator of the title *thermodynamic integration*, though this name often applies to all such methods. Either way, a priori knowledge of the system's limits is required to find any free energy difference. On top of this, the integration of λ can sometimes be noisy, requiring a small grid spacing and many intermediate simulations. Finally, if we want to discern the free energy difference between two competing phases at the same coupling and temperature, we must perform the thermodynamic integration for both phases, starting from a known limit, and compare the resulting free energies. This requires many simulations and can be very expensive.

An alternative method to calculate free energy differences comes from Bennett [8]. We first generalize the Metropolis Monte Carlo acceptance ratio given in Chapter 2 to be for any move going from configurational space a to b,

$$A(a \to b) = min\{1, \frac{T(b \to a)\rho_b(\beta)}{T(a \to b)\rho_b(\beta)}\}, \tag{7.9}$$

where $T(a \to b)$ is the probability of proposing a MC move $a \to b$ and $\rho_a(\beta) = \exp[-S_a(\beta)]$ is the statistical weight of the configuration a. This form enforces the detailed balance condition

$$T(a \to b)A(a \to b)\rho_a(\beta) = T(b \to a)A(b \to a)\rho_b(\beta). \tag{7.10}$$

If we choose the transition probability to be a uniform distribution and trace over all space we find

$$\begin{aligned}
\mathrm{Tr}\left[A(a\to b)\rho_a(\beta)\right] &= \mathrm{Tr}\left[A(b\to a)\rho_b(\beta)\right] && (7.11)\\
\mathcal{Z}_a\frac{\mathrm{Tr}\left[A(a\to b)\rho_a(\beta)\right]}{\mathcal{Z}_a} &= \mathcal{Z}_b\frac{\mathrm{Tr}\left[A(b\to a)\rho_b(\beta)\right]}{\mathcal{Z}_b} && (7.12)\\
\mathcal{Z}_a\langle A(a\to b)\rangle_a &= \mathcal{Z}_b\langle A(b\to a)\rangle_b && (7.13)\\
\frac{\mathcal{Z}_a}{\mathcal{Z}_b} &= \frac{\langle A(a\to b)\rangle_a}{\langle A(b\to a)\rangle_b} && (7.14)
\end{aligned}$$

where the brackets $\langle\ldots\rangle_a$ represent a canonical average in the configuration space a and $\mathcal{Z}_a$ is its canonical partition function. To arrive upon a free energy difference between a and b, we write

$$\begin{aligned}
F_a - F_b &= -\frac{1}{\beta}\ln\mathcal{Z}_a + \frac{1}{\beta}\ln\mathcal{Z}_b && (7.15)\\
&= -\frac{1}{\beta}\ln\frac{\mathcal{Z}_a}{\mathcal{Z}_b} && (7.16)\\
&= -\frac{1}{\beta}\ln\frac{\langle A(b\to a)\rangle_b}{\langle A(a\to b)\rangle_a}. && (7.17)
\end{aligned}$$

Thus the free energy difference between two systems can be measured simply by switching between the systems and taking the ratio of their respective acceptance probabilities. Note there is no actual requirement to do the switching within a single simulation, so sometimes these averages are computed separately. Also, in general, the transition probability does not need to be uniform for (7.17) to hold, in which case,

$$F_a - F_b = -\frac{1}{\beta}\ln\frac{\langle T(b\to a)A(b\to a)\rangle_b}{\langle T(a\to b)A(a\to b)\rangle_a}. \quad (7.18)$$

The configurational spaces a and b are not limited to representing differences in coupling, as in the thermodynamic integration, but can be any arbitrary change to the many-body action. Provided there is finite overlap between a and b, (7.17) will hold. This allows calculation of free energy differences between competing phases in a single simulation. Finally, even though here we only consider two configurational spaces, the Bennett acceptance ratio (BAR) method is trivially generalizable to many more. In this way, by measuring the acceptance ratios when switching through a grid of variational parameters, we can find the optimal configuration. Thus applying the BAR method to optimizing nodal structures in PIMC amounts to creating a nodal ansatz, switching between sets of its variational parameters, and finding which point in the variational space the simulation spends the most time. Note that by *time*, we refer to number of Monte Carlo steps, not actual CPU time. To tackle the first step of generating variational spaces, in the following sections we propose several ansatzes.

7.2 Optimizing free particle nodes

As we saw in Chapter 5, free particle nodes seemingly work well for reproducing the actual nodal structure of the electron liquid. This was verified by projecting from the known classical limit down to previous zero-temperature QMC results. Nevertheless, at low density ($r_s > 10$), the free particle node approximation begins to show signs of failing, largely due to the increased role of the Coulomb interaction. It makes sense then to target this regime for optimizing the free particle nodal structure.

The simplest possible variational model constructed from free particle nodes involves inserting a single temperature-independent parameter α. Recalling the form of the free particle partition function from Chapter 3, we write

$$\rho_{ij_\star}(\alpha) = (4\pi\lambda\tau)^{-D/2} \exp\left[-\alpha \frac{(r_i - r_{j\star})^2}{4\lambda\tau}\right]. \tag{7.19}$$

The total many-body nodal partition function is then $\rho(\alpha) = \frac{1}{N!} \det \rho_{ij_\star}(\alpha)$. From this form, we see that we can subsume the parameter α into λ or τ, defining an effective mass or temperature, respectively. We note that this is not the same as the commonly defined effective mass which is defined as the mass of a non-interacting system that recreates the low energy excitations of the interacting system. Instead, this effective mass or temperature applies explicitly to the nodal structure. The full, interacting many-body partition function is already being sampled exactly while the nodes only constrain the configurational space. Nevertheless, we will see this notion of effective mass provides a worthwhile physical picture for optimization.

Before we attempt to optimize the nodes of an interacting system, we wish to check this variational treatment will give back the exact answer if applied to free particles, i.e. $\alpha = 1$. To this end, we test the method applied to a free particle system of $N = 7$ particles at $r_s = 1$ and $\Theta = 1/8$. Since the behavior of the free Fermi gas is independent of density for a given Θ value, we expect this point to be representative of the optimization procedure at all densities. We use a discrete grid of α points, enough to illustrate a clear free energy minimum, which we recall corresponds to the variational value at which the simulation spends the most time, denoted $p(\alpha)$. In Fig. 7.2, we plot the result of this test. We see a clear maximum in the probability $p(\alpha)$ at $\alpha = 1$, thus the method reproduces the exact result. Away from the exact result, we see an exponential drop off in both directions. This behavior is encouraging since often times free nodal surfaces can be noisy, which complicates the minimization procedure.

Now that we have verified that our method works in the exact case, we try applying it to the HEG at different densities and temperatures, specifically with $N = 7$ particles at $r_s = 1, 4, 10$ and $\Theta = 1/8, 1$ for the paramagnetic $\xi = 1$ liquid. We plot the results from these tests in Figs. 7.2, 7.2, and 7.2. As was the case for the free Fermi gas test, we see an exponential decay away from the optimal value, allowing a sparse α grid.

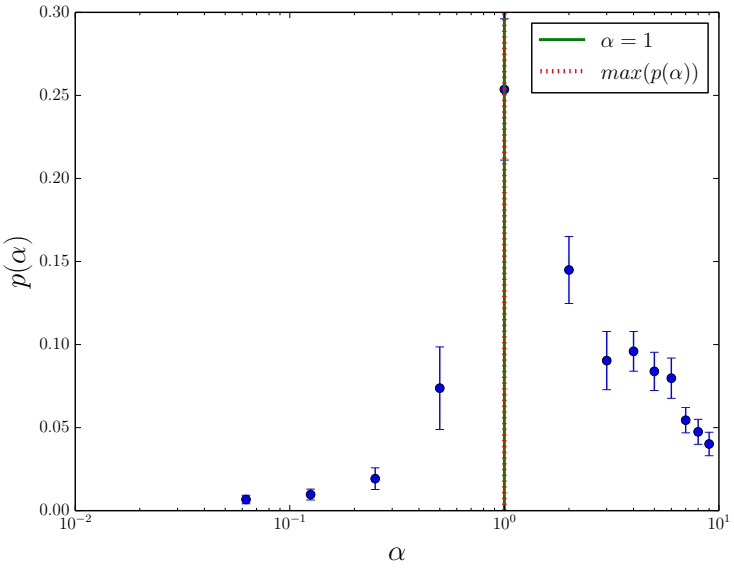

Figure 7.1: Variational optimization of free particle nodes in a free particle system at density $r_s = 1$ and temperature $\Theta = 1/8$. The most time is spent at the exact effective temperature, i.e. $\alpha = 1$.

Fortuitously, this decay is more pronounced for low temperatures where the nodal structure plays a greater role. At higher temperatures, the free energy surface flattens, though there the nodes play an insignificant role in observables like the energy.

For low temperatures ($\Theta = 1/8$), we see that at the highest density $r_s = 1$, the effective mass parameter is optimized at value $\alpha < 1$. In our physical picture of the nodal variational structure, $\alpha < 1$ corresponds to an effective mass that is smaller than the bare mass. This result is consistent with the exact zero-temperature RPA limit of the effective mass first derived by Gell-Mann [45] where,

$$\frac{m_{eff}}{m} = 1 + 0.083 r_s[-\ln r_s - 0.203] + \mathcal{O}(r_s^2). \tag{7.20}$$

We point out the consistency is merely qualitative, however, as at $r_s = 1$, (7.20) predicts $\frac{m_{eff}}{m} = 0.983151$ while we predict an optimal $\alpha = 0.41$.

As we decrease the density we see in Figs. 7.2 and 7.2, the effective mass parameter is optimized at a value $\alpha > 1$, implying $m_{eff} > m$. This result is consistent with previous ground state QMC studies in which the paramagnetic HEG has a rapidly increasing effective mass with decreased density [34]. At higher temperatures ($\Theta = 1$), we see that see that optimal values for α begin to approach unity. This is also consistent with the effective mass physical picture because the HEG one-body excitation levels approach the free Fermi gas limit as the temperature is raised.

Even though a clear free energy maximum can be seen in this variational space, it is useful to see how

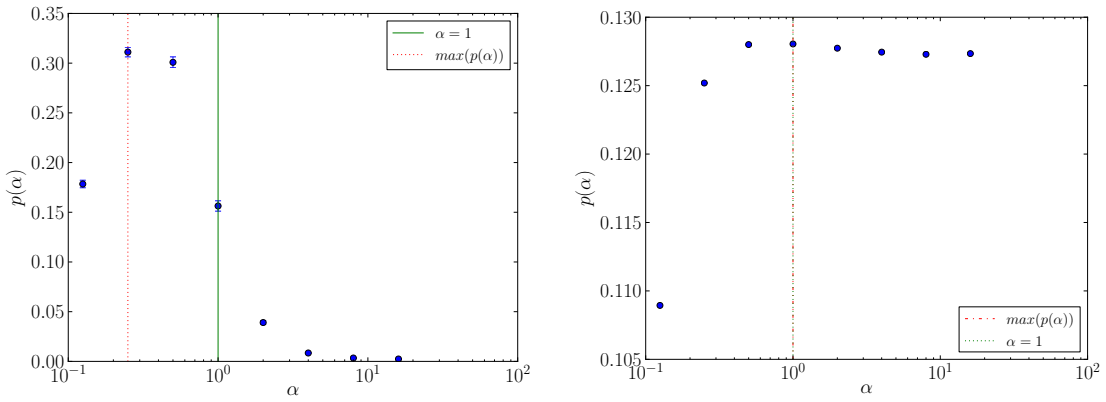

(a) (b)

Figure 7.2: Free energy optimization of the effective mass parameter α for the polarized ($\xi = 1$) HEG with $N = 7$ at density $r_s = 1$ for temperatures (a) $\Theta = 1/8$ and (b) $\Theta = 1$. At this density, we see that the optimal $\alpha < 1$ as is predicted in the high-density RPA limit [45].

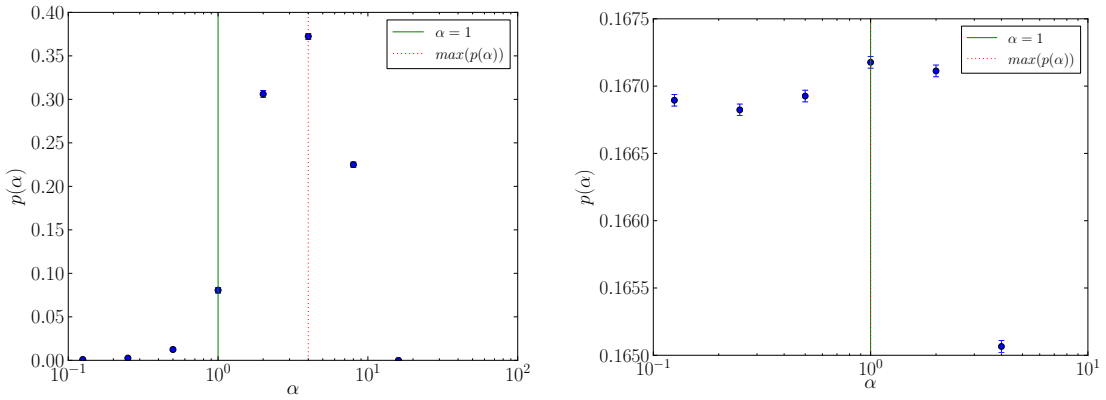

(a) (b)

Figure 7.3: Free energy optimization of the effective mass parameter α for the polarized ($\xi = 1$) HEG with $N = 7$ at density $r_s = 4$ for temperatures (a) $\Theta = 1/8$ and (b) $\Theta = 1$.

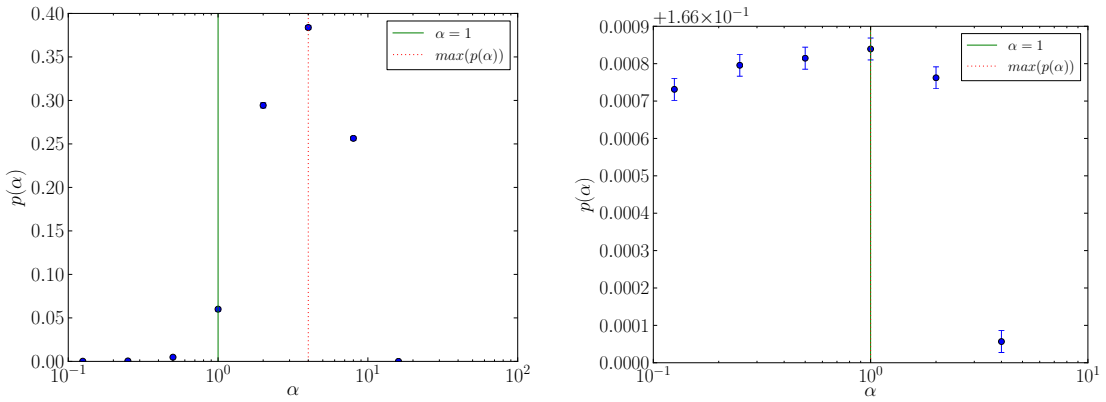

(a) (b)

Figure 7.4: Free energy optimization of the effective mass parameter α for the polarized ($\xi = 1$) HEG with $N = 7$ at density $r_s = 10$ for temperatures (a) $\Theta = 1/8$ and (b) $\Theta = 1$. At this density, we see that the optimal $\alpha > 1$ as is predicted for the paramagnetic HEG by low-density QMC studies [34].

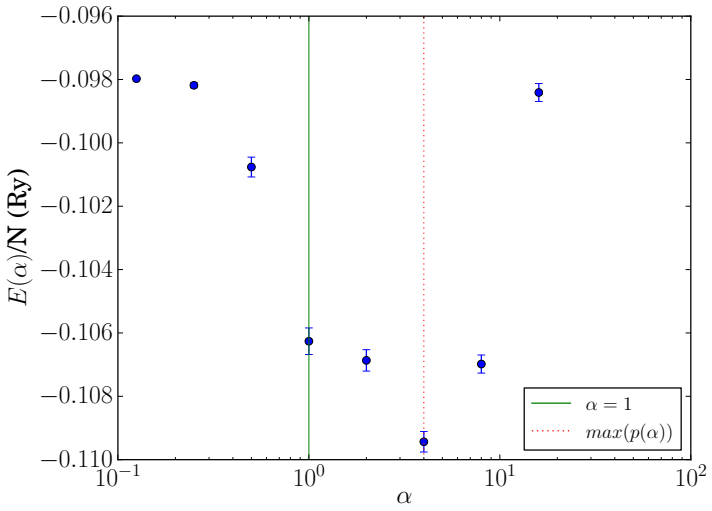

Figure 7.5: Per particle energies for each effective mass parameter α for the polarized ($\xi = 1$) HEG with $N = 7$ at density $r_s = 10$ and temperature $\Theta = 1/8$. We see that the energy is minimized near the same value as the free energy.

this translates to observables. Thus for each variational point for $r_s = 10$, $\Theta = 1/8$, we run an individual simulation to measure the energy. In Fig. 7.2, we plot the measured energies. We see the behavior in the energy resembles that of the free energy in that the variational parameters that minimized the free energy also minimize the energy. This is likely because the entropic part of the free energy is small at these low temperatures. On the other hand, it may be possible to differentiate between the free energy and internal energy minimums with a finer grid of variational parameters.

Through the direct physical analogue of the effective mass provided by this nodal variational model, we have shown that physical intuition can lead to better nodes. It has yet to be seen if this is the precise effective mass from many-body theory [45], however, its behavior suggests it is intimately related. At high density, screening reduces the effective mass to a value less than the bare mass. At low density, increased interaction strengths get renormalized into a larger effective mass.

To take the next step beyond this basic variational model is to allow the temperature dependence to change across the path such that,

$$\rho_{ij_\star}(n\tau) = (4\pi\lambda\tau)^{-D/2} \exp\left[-\frac{(r_i - r_{j\star})^2}{4\lambda_{eff}(n\tau)n\tau}\right], \tag{7.21}$$

where we define

$$\lambda_{eff}(n\tau) \equiv \lambda a_1 \frac{1 + (n\tau)^{a_2}}{1 + (n\tau)^{a_3}} \tag{7.22}$$

with a_1, a_2, a_3 as variational parameters and n defining the number of time slices to the nearest reference slice. With this form, time slices far away from the reference slice can have qualitatively different behavior than those close to it. For example, in the short-time limit $n\tau \to 0$, we see that $\lambda_{eff}(n\tau) \to a_1\lambda$, which is the same as the previous form. We suspect this to be the correct behavior since that short-time limit corresponds to the high-temperature, free particle limit. In the long-time limit, $\lambda_{eff}(n\tau) \to \lambda a_1 (n\tau)^{a_2 - a_3}$, which results in a density matrix of the form

$$\rho_{ij_\star}(n\tau) = (4\pi\lambda\tau)^{-D/2} \exp\left[-\frac{1}{a_1}\frac{(r_i - r_{j\star})^2}{4\lambda(n\tau)^{(a_2-a_3)+1}}\right]. \tag{7.23}$$

The end result is an effective mass or temperature that varies along the path. Since this model has more than one variational parameter, optimizing it is a more complex task. Creating an N_{param}-dimensional grid becomes increasingly expensive with N_{param} as it scales like $\mathcal{O}(N_{param}^{N_{param}})$. Instead, we use a downhill simplex algorithm, as known as the Nelder-Mead method [83]. In essence, this method computes the average time spent at a set of variational parameters or vertices that form a N_{param}-dimensional polygon. It then reflects this polygon and repeats the simulation. If it finds vertices with a large average time, it then extends the polygon in their direction. If it finds vertices that have a small average time, it shrinks the polygon away from them. This process is continued until convergence, within a specified tolerance, is reached on a point in the N_{param}-dimensional space. Importantly, we note that by setting $a_2 = a_3 = 0$, we get back the original effective mass model, allowing us to find a free energy difference between it and the new model. In this approach, for $r_s = 10$ and $\Theta = 1/8$, we find optimal variational parameters of $a_1 = 0.124$, $a_2 = 0$, and $a_3 = 2.01$ which give a per particle energy of $E = -0.112(1)Ry$. We again see that this is lower than the internal energy minimum of the previous variational ansatz of $E = -0.109(1)Ry$.

Another potential nodal ansatz is a parametrized formulation of the backflow coordinates used in zero-temperature QMC [54]. In essence, backflow incorporates many-body character into a single particle Slater determinant. A direct adaptation to PIMC has yet to materialize. However, it is possible to create a

variational framework flexible enough to include all N coordinates into each element of the ρ_{ij} determinant with tunable parameters,

$$\rho_{ij_\star}(\{\alpha_n\}) = exp-[\frac{|r_i - r_{j_\star}|^2 + \nabla_R y_{ij}(\{\alpha_n\})}{4\lambda\tau}]. \tag{7.24}$$

Future efforts will focus on optimizing this more general variational ansatz.

7.3 Optimizing nodes for ions

The free particle variational nodal structure provides valuable insight into the finite-temperature HEG likely because it starts as a close approximation to the real nodal structure. For inhomogeneous systems, e.g. systems with ions, no approximation to the nodal structure as yet exists. In systems of atomic gases, at high temperatures, it may makes sense to try the free particle nodal optimization above. However, at low temperatures, or for systems with few ions, the nodal structure will necessarily need to include the effect of the ion. To this end, we propose and test two such variational nodal ansatzes.

The first variational nodal ansatz we attempt again uses the free nodal nodal structure, but adds to it a parametrized form of the hydrogenic atomic orbital. Thus we write

$$\rho_{ij_\star}(\{\alpha_n\},\{\gamma_n\}) \equiv (4\pi\lambda\tau)^{-D/2} \exp\left[-\frac{(r_i - r_{j\star})^2}{4\lambda\tau}\right] + \sum_k \sum_n \alpha_n \phi_n^\dagger(r_i, r_k; \gamma_n)\phi_n(r_{j_\star}, r_{k_\star}, \gamma_n) \tag{7.25}$$

where the sum over k loops over all ions in the system while the sum over n loops over the desired atomic orbitals. Instead of a single variational parameter, we now have two sets over variational parameters $\{\alpha_n\}$ and $\{\gamma_n\}$. The first set $\{\alpha_n\}$ gives the relative weight of each atomic orbital with respect to both the free nodal density matrix and the other orbitals. This is meant to provide a simple extrapolation from the ground state nodal structure to the classical limit free particle nodal structure. The second set of parameters $\{\gamma_n\}$ parametrizes each atomic orbital. Typically, these values are used to create an effective atomic number $Z_{eff,n} \equiv \gamma_n Z$.

The simplest non-trivial implementation of the above method is the Li atom in which the ground state contains one spin-down and two spin-up electrons. The spin-down electron has no nodes since it is effectively distinguishable in this system. Here we include only the first term in the sum over orbitals, the $1s$ hydrogenic orbital defined as,

$$\phi_{1s}(r_i, r_j, \gamma_{1s}) \equiv \frac{1}{(\gamma_{1s}Z)^3} e^{-\gamma_{1s}Z|r_i - r_j|}, \tag{7.26}$$

where we have absorbed the rest of the normalization into α_{1s}. In applying this nodal ansatz at $T = 1260K$, we find that the free energy is at a minimum as $\alpha_{1s} \to 0$ or $\gamma_{1s} \to \infty$. In other words, the optimal nodal

structure within this variational space is the free particle nodal structure alone.

For a second trial ansatz for inhomogeneous systems we employ the exact harmonic nodal structure presented in Chapter 3, where we treat each ion as the center of a harmonic trap and use the harmonic frequency as a variational parameter. Thus we write,

$$\rho_{ij_\star}(\omega) = \sum_k \left(\frac{\omega}{4\pi\lambda \sinh(\beta\omega)}\right)^{D/2} \exp\left[-\frac{\omega}{4\lambda \sinh(\beta\omega)}(|r_i - r_k|^2 + |r_{j_\star} - r_{k_\star}|^2)\cosh(\beta\omega) - 2(r_i - r_k)(r_{j_\star} - r_{k_\star})\right] \tag{7.27}$$

where the sum over k represents a sum over all ions in the system.

The simplest non-trivial test of the harmonic structure must have more than two indistinguishable electrons, as was shown in Chapter 3. Thus we choose carbon in its ground state with 4 spin-up electrons and 2 spin-down electrons. Through variational optimization, we find there is a free energy minimum as ω tends to zero. Once again, this is the free particle node limit, implying that free particle nodes do quite well in estimating the ground state nodes of atomic carbon.

It is important to emphasize that for both these tests, the free energy minimum is found only within the variational space created by the ansatz, i.e. it is not a universal free energy minimum. The exact nodal structure is likely to be different from the naive free particle nodal structure, but may not be included in the parameter space being optimized. The next thing to try would be to apply the above variational models to a gas of atoms. Our work with the electron gas leads us to believe that the nodes may behave qualitatively differently in a periodic system. Also, some previous work indicates that the $1s$ model may provide a more varied free energy surface for a many-body system of Li atoms [61].

Chapter 8

Permutation space reconstruction

As explained in Chapter 3, explicit treatment of many-body Fermi statistics in path integral Monte Carlo (PIMC) results in exponentially scaling computational cost due to the near cancellation of contributions to observables from even and odd permutations. Through direct analysis of exchange statistics we find that individual exchange probabilities in homogeneous systems are, except for finite size effects, independent of the configuration of other permutations present. For two representative systems, ^3He and the homogeneous electron gas, we show that this allows the entire antisymmetrized density matrix to be generated from a simple model depending on only a few parameters obtainable directly from a standard PIMC simulation. The result is a polynomial scaling algorithm and up to a 10 order of magnitude increase in efficiency in measuring fermionic observables for the systems considered. We argue that this simple structure of permutation space will hold in many other homogeneous systems as well and, as a consequence, strategies analogous to our approach may be employed to reduce the computational complexity of treating Fermi statistics in a wide class of problems.

Path integral Monte Carlo (PIMC) methods provide essentially exact results for low temperature properties of N-body bosonic systems, see Chapter 2. The same algorithm can be applied to Fermions, however a sign problem, arising from the approximately equal weights of the $N!$ oppositely signed permutations, limits the accuracy of the results. In fact, as shown in Chapter 3, naive application of the PIMC method to fermions results in exponentially decreasing efficiency as the temperature decreases and N increases. Consequently, enforcement of Fermi symmetry for all but the smallest finite-temperature systems has so far required the introduction of an approximation that restricts path integrals to prevent sign changes, analogous to the fixed node approximation for the ground state quantum Monte Carlo (QMC).

In order to determine whether it is possible to overcome the sign problem directly, we have used the PIMC method to examine permutation space with great accuracy. From this data we are able to show that for homogeneous systems, the effective dimensionality of the sum over permutations can be reduced to a relative small finite number, allowing for exact treatment of large systems to low temperatures.

We begin this chapter with an overview of the formalism behind this new method. Then by application

to the free Fermi gas to calculate energies and pair correlation functions, we make rigorous its regime of applicability. Next we take a brief detour into the historical development of understanding permutation space through the lens of Feynman and Kikuchi's work on bosonic ^{4}He. With this work as a guide, we then present application of our new method to two fermionic interacting system: ^{3}He and the homogeneous electron gas (HEG). Finally we speculate on its application to inhomogeneous systems.

8.1 Formalism

In the proceeding, we provided a rigorous derivation of the permutation space structure of the free Fermi gas. We explicitly show how the entire $N!$ space may be written in terms of N variables or, in some limiting cases, a single parameter. We show how this affects various diagonal observables, namely the total energy and pair correlation function. We conclude with a discussion of how this knowledge of permutation space can greatly reduce the computational complexity of the path integral Monte Carlo simulation of fermions.

8.1.1 Permutation sectors

The diagonal density matrix of a fermionic system at temperature $T = 1/k\beta$, denoted $\rho^{\mathcal{A}}(\mathbf{R}, \mathbf{R}; \beta)$, can be expressed as a weighted sum over off-diagonal distinguishable density matrices, ρ^D, connecting the many-body coordinates $\mathbf{R}$ to all permutations $\mathcal{P}(\mathbf{R})$ in imaginary time β. This gives

$$\rho^{\mathcal{A}}(\mathbf{R}, \mathbf{R}; \beta) = \frac{1}{N!} \sum_{\mathcal{P} \in S_N} (-1)^{\mathcal{P}} \rho^D(\mathbf{R}, \mathcal{P}(\mathbf{R}); \beta). \tag{8.1}$$

where S_N is the symmetric group of all possible permutations.

Direct treatment of this sum over permutations is made difficult in two ways: the high dimensionality of the full quantum many-body density matrix necessitates the use of a stochastic sampling method for evaluation of expectation values of observables, and the alternating sign arising from antisymmetrization over permutations of paths $(-1)^{\mathcal{P}}$ results in a large variance. Summing over all $N!$ permutation sectors of (8.1) with their respective signs results in the notorious fermion sign problem. One can show this explicitly by looking at the average value of the sign which may be written exactly as

$$\langle \sigma \rangle = \frac{\mathcal{Z}_F^{(N)}(\beta)}{\mathcal{Z}_B^{(N)}(\beta)} = \exp\left[-\beta(F_F - F_B)\right] \tag{8.2}$$

where the subscripts F and B representation fermion and boson quantities respectively. For free fermions

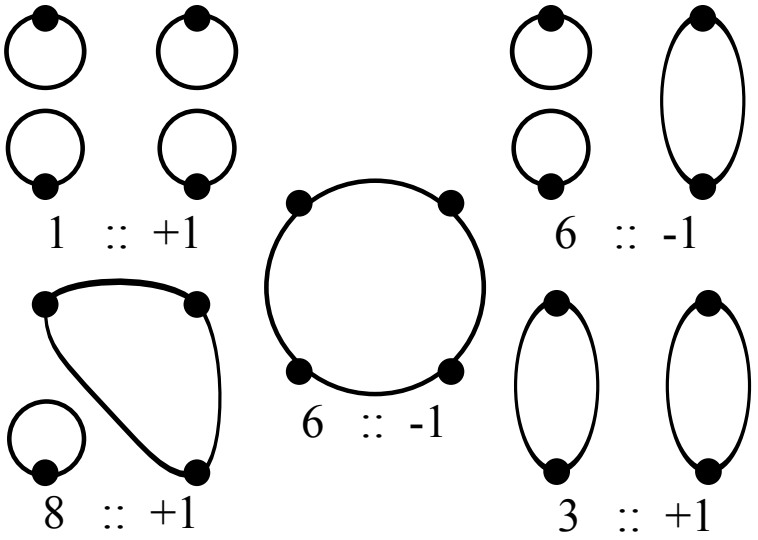

Figure 8.1: Diagrammatic representation of the equivalence classes of the symmetric group for 4 particles, S_4, the number of elements in each class and the sign of the contribution of members of each class to the antisymmetric partition function are shown below each diagram.

this becomes

$$\langle\sigma\rangle_0 = \exp\left[-\frac{N^2}{V}(2\pi\lambda\beta)^{D/2}\right]. \tag{8.3}$$

Since all observables measured in simulation must be normalized by $\langle\sigma\rangle$, there is an exponential increase in variance with increased number of particles and decreased temperature. Nevertheless, at finite-temperature and finite N, $\langle\sigma\rangle$ is still non-zero leaving the door cracked for a possible solution. Our goal in this work is to reduce the effective dimensionality of the sum over permutations.

As a starting point along these lines we note that evaluation of (8.1) can be simplified by recognizing that while there are $N!$ possible permutations of N particles, the symmetry group S_N can be further organized into subsets of topologically equivalent diagrams $[p] \equiv \{\mathcal{P} \in S_N | \mathcal{P} \sim p\}$ [43]. Figure 8.1 shows representative members from the five equivalence classes of the symmetric group for four particles, S_4. This provides a dramatic reduction in the number of sectors needed to sum over. For example, for $N = 33$ particles the sum is reduced from $\sim 10^{38}$ to $\sim 10^5$ terms.

Expectations evaluated within different members of the same class are identical, and one need only evaluate a single representative permutation in each class rather than the full sum. The observables for each equivalence class $[p]$ may be written as

$$\langle\mathcal{O}\rangle_{[p]} = \frac{\sum_{\mathcal{P}\in[p]} \int d\mathbf{R}\ \hat{\mathcal{O}}\rho(\mathbf{R}, \mathcal{P}(\mathbf{R}); \beta)}{\sum_{\mathcal{P}\in[p]} \int d\mathbf{R}\ \rho(\mathbf{R}, \mathcal{P}(\mathbf{R}); \beta)} \tag{8.4}$$

and may be measured independently during simulation.

To then reconstruct the fully antisymmetrized observable one must sum over the equivalence classes with their respective sign,

$$\langle \mathcal{O} \rangle = \frac{\sum_{[p]} (-1)^{[p]} \omega_{[p]}(\beta) \langle \mathcal{O} \rangle_{[p]}}{\sum_{[p]} (-1)^{[p]} \omega_{[p]}(\beta)} \tag{8.5}$$

where we have defined $\omega_{[p]}(\beta)$ as the probability of a given equivalence class relative to the symmetric sum over all permutations,

$$\omega_{[p]}(\beta) \equiv \frac{\mathcal{Z}_{[p]}}{\mathcal{Z}_B} \tag{8.6}$$

$$\equiv \frac{\sum_{\mathcal{P} \in [p]} \int d\mathbf{R}\ \rho(\mathbf{R}, \mathcal{P}(\mathbf{R}); \beta)}{\sum_{\mathcal{P} \in S_N} \int d\mathbf{R}\ \rho(\mathbf{R}, \mathcal{P}(\mathbf{R}); \beta)}. \tag{8.7}$$

At zero-temperature, the denominator of (8.5) becomes exactly zero. At any finite-temperature, however, each nonequivalent permutation sector will have a different mean energy and therefore a different probability and a nonzero contribution to the antisymmetrized partition function.

The cost of summing over all unique equivalence classes of S_N still scales exponentially with N and attempts to make use of the structure afforded by the symmetry group directly have met with mixed success [75, 107]. Ultimately, in order to obtain a polynomial scaling algorithm, it is therefore essential to determine whether all sectors need to be evaluated equally or at all. To this end, we outline a scheme to dramatically reduce the parameterization of the permutation space.

8.1.2 Separating permutation space

In general, each permutation class is uniquely identified by the number of loops of a given length so that $[C_1, C_2, \ldots, C_N]$ represents the class with C_1 cycles of length one, C_2 cycles of length two, and so on. The number of sectors in $[p]$ consisting of $C_{[p]1} \ldots C_{[p]N}$ cycles of length $l_1 \ldots l_N$ is

$$M_{[p]} = \frac{N!}{\prod_{l=1}^{N} C_{[p]l}! l^{C_{[p]l}}} \tag{8.8}$$

allowing us to write

$$\mathcal{Z}^{(N)}(\beta) = \frac{1}{N!} \sum_{[p]} (-1)^{[p]} M_{[p]} \int d^D x_1 \ldots d^D x_N \Big(\prod_{i=1}^{N} \int_{x_i(0)}^{x_{[p](i)}(\hbar\beta)} d^D x_i \Big) \exp^{-\mathcal{A}^{(N)}/\hbar} \tag{8.9}$$

where the N-particle action is given by,

$$\mathcal{A}^{(N)} = \int_0^{\hbar\beta} d\tau \sum_{i=1}^{N} [\frac{1}{2} m\dot{x}_i^2 - V_{ext}(x_i) - \frac{1}{2}\sum_{j\neq i}^{N} V_{int}(x_i, x_j)]. \tag{8.10}$$

For free particles $V_{ext}, V_{int} = 0$. Thus,

$$\begin{aligned} (\prod_{i=1}^{N} \int_{x_i(0)}^{x_{[p](i)}(\hbar\beta)} d^D x_i) \exp^{-\mathcal{A}^{(N)}/\hbar} &= \prod_{i=1}^{N} \int_{x_i(0)}^{x_{[p](i)}(\hbar\beta)} d^D x_i \exp[-\frac{1}{\hbar}\int_0^{\hbar\beta} d\tau \frac{1}{2} m\dot{x}_i^2] & (8.11) \\ &= \prod_{i=1}^{N} \frac{1}{\sqrt{2\pi\hbar^2\beta/m}^D} \exp[-\frac{m}{2\hbar^2\beta}(x_{[p](i)} - x_i)^2]. & (8.12) \end{aligned}$$

Defining $\lambda \equiv \frac{\hbar^2}{2m}$, we are left with following form for the free particle many-body partition function,

$$\mathcal{Z}_0^{(N)}(\beta) = \frac{1}{N!}\sum_{[p]} (-1)^{[p]} M_{[p]} \int d^D x_1 \ldots d^D x_N \prod_{i=1}^{N} \frac{1}{\sqrt{4\pi\lambda\beta}^D} \exp[-\frac{(x_{[p](i)} - x_i)^2}{4\lambda\beta}]. \tag{8.13}$$

Now each $[p]$ decomposes into mutually disconnected groups, each with a winding number ℓ, subject to the constraint that $N = \sum_\ell \ell C_{[p]\ell}$. For each group, we can then take each integral separately, leading to

$$\mathcal{Z}_0^{(N)}(\beta) = \frac{1}{N!}\sum_{[p]} (-1)^{[p]} M_{[p]} \prod_{\ell=1}^{N} \mathcal{Z}_0^{(1)}(\ell\beta)^{C_{[p]\ell}} \tag{8.14}$$

where $\mathcal{Z}_0^{(1)}(\ell\beta)$ is the partition function for a single particle at inverse temperature $\ell\beta$. We find it convenient to rearrange terms slightly in order to make a more general statement. To this end, we write,

$$\begin{aligned} \mathcal{Z}_0^{(N)}(\beta) &= \mathcal{Z}_B \sum_{[p]} (-1)^{[p]} \frac{\mathcal{Z}_{[p]}}{\mathcal{Z}_B} & (8.15) \\ &\equiv \mathcal{Z}_B \sum_{[p]} (-1)^{[p]} \omega_{[p]}(\beta) & (8.16) \end{aligned}$$

with

$$\omega_{[p]}(\beta) \equiv \frac{1}{\mathcal{Z}_B} \prod_{\ell=1}^{N} M_{[p]\ell} P_\ell(\beta)^{C_{[p]\ell}} \tag{8.17}$$

where $M_{[p]\ell} \equiv 1/(C_{[p]\ell}!\ell^{C_{[p]\ell}})$ is a new combinatorial factor, and P_ℓ is related to the single-particle partition function and independent of the equivalence class $[p]$. This final form shows that all $N!$ permutation sectors may be written in terms of N parameters, specifically the N free one particle partition functions at inverse temperatures $\ell\beta$ with $\ell = 1 \ldots N$.

The net result is an algorithm with an effective computational cost scaling as well as $\mathcal{O}(N^2)$ in the number

of particles since the probability density associated with each of the equivalence classes can be reconstructed from the probability densities of an $\mathcal{O}(N)$ subset of S_N (e.g. $[N,0,0,\ldots],[0,N/2,0,0,\ldots],[0,0,N/3,0,\ldots],etc.$) and the computational cost of the PIMC algorithm for free particles can be $\mathcal{O}(N)$.

Going further, we can write the free one particle partition function in a box of volume $\Omega \equiv L^D$ as

$$\mathcal{Z}_0^{(1)}(\beta) = \sum_n \exp\left[-\beta\lambda(\frac{2\pi n}{L})^2\right] \tag{8.18}$$

where $n \equiv (n_1,\ldots,n_D)$ with $n_i = -\infty,\ldots,\infty$. Alternatively, through Laplace transform, this may be written,

$$\mathcal{Z}_0^{(1)}(\beta) = \frac{\Omega}{\sqrt{4\pi\lambda\beta}^D}\sum_n \exp\left[-\frac{(nL)^2}{4\lambda\beta}\right]. \tag{8.19}$$

Now, in the limit $L \gg 4\lambda\beta$, the sum over states may be approximated as an integral leading to

$$\mathcal{Z}_0^{(1)}(\ell\beta) = \frac{\Omega}{\sqrt{4\pi\lambda\ell\beta}^D} = (\frac{\gamma}{\ell})^{D/2}\mathcal{Z}_0(\gamma\beta). \tag{8.20}$$

Thus in this limit, the entirety of permutation space may be formed from a single parameter. Taking advantage of these observations allow us to reduce the task of finding the relative probability of different sectors to that of determining a single temperature dependent parameter, leading to an $O(N)$ algorithm.

8.1.3 Observables

Given the expression for $\omega_{[p]}$ in (8.17), observables also take a simple form.

Average Sign

The first obvious quantity to try calculating is the average value of the sign since all other observables with require it in their denominator. Recall from 8.2 its definition,

$$\langle\sigma\rangle = \frac{\mathcal{Z}_F^{(N)}(\beta)}{\mathcal{Z}_B^{(N)}(\beta)} \tag{8.21}$$

$$= \frac{\sum_{\mathcal{P}\in S_N}(-1)^{\mathcal{P}}\int d\mathbf{R}\rho(\mathbf{R},\mathcal{P}(\mathbf{R});\beta)}{\sum_{\mathcal{P}\in S_N}\int d\mathbf{R}\ \rho(\mathbf{R},\mathcal{P}(\mathbf{R});\beta)}. \tag{8.22}$$

Rewriting this in terms of the reduced parametrization above, we find

$$\langle\sigma\rangle = \frac{\sum_{[p]}(-1)^{[p]}\omega_{[p]}(\beta)}{\sum_{[p]}\omega_{[p]}(\beta)} \tag{8.23}$$

$$= \sum_{[p]}(-1)^{[p]}\prod_{\ell=1}^{N} M_{[p]\ell}P_\ell(\beta)^{C_{[p]\ell}} \tag{8.24}$$

where again there are only N free parameters, i.e. each P_ℓ with $l = 1 \dots N$.

Total Energy

Now recall the energy may be defined as,

$$E^{(N)}(\beta) = \frac{\partial}{\partial\beta}\log \mathcal{Z}_F^{(N)}(\beta) = \frac{1}{\mathcal{Z}_F^{(N)}(\beta)}\frac{\partial}{\partial\beta}\mathcal{Z}^{(N)}(\beta). \tag{8.25}$$

For the model presented in (8.17) then,

$$E^{(N)}(\beta) = \frac{1}{\mathcal{Z}_F^{(N)}(\beta)}\frac{\partial}{\partial\beta}[\sum_{[p]}(-1)^{[p]}\omega_{[p]}(\beta)] \tag{8.26}$$

$$= \frac{1}{\mathcal{Z}_F^{(N)}(\beta)}\sum_{[p]}(-1)^{[p]}\frac{\partial}{\partial\beta}\prod_{\ell=1}^{N} M_{[p]\ell}P_\ell(\beta)^{C_{[p]\ell}} \tag{8.27}$$

$$= \frac{1}{\mathcal{Z}_F^{(N)}(\beta)}\sum_{[p]}(-1)^{[p]}\prod_{\ell=1}^{N} M_{[p]\ell}P_\ell(\beta)^{C_{[p]\ell}}\sum_{\gamma=1}^{N} C_{[p]\gamma}\frac{\frac{\partial}{\partial\beta}P_\gamma(\beta)}{P_\gamma(\beta)} \tag{8.28}$$

$$\equiv \frac{\mathcal{Z}_B^{(N)}(\beta)}{\mathcal{Z}_F^{(N)}(\beta)}\sum_{[p]}(-1)^{[p]}\omega_{[p]}(\beta)\sum_{\gamma=1}^{N} C_{[p]\gamma}\frac{\frac{\partial}{\partial\beta}P_\gamma(\beta)}{P_\gamma(\beta)} \tag{8.29}$$

$$\equiv \frac{1}{\langle\sigma\rangle}\sum_{[p]}(-1)^{[p]}\omega_{[p]}(\beta)\sum_{l=1}^{N} C_{[p]l}E_l(\beta) \tag{8.30}$$

where we have defined $E_l(\beta) \equiv \frac{\frac{\partial}{\partial\beta}P_l(\beta)}{P_l(\beta)}$ as the energy of a given cycle length. What we have found is that if the permutation sector probabilities can be described by N parameters, so may the energy.

Pair Correlation Function

Finally recall the pair correlation function is defined as,

$$g(x) = \frac{2\Omega}{N^2}\langle\sum_{i<j}\delta(x^{(i)} - x^{(j)} - x)\rangle. \tag{8.31}$$

The expectation value is given by

$$\langle\sum_{i<j}\delta(x^{(i)}-x^{(j)}-x)\rangle = \frac{1}{\mathcal{Z}_F^{(N)}(\beta)}\frac{1}{N!}\sum_{\mathcal{P}\in S_N}(-1)^{\mathcal{P}}\int d^Dx_1\ldots d^Dx_N \sum_{i<j}\delta(x_i-x_j-x)\prod_{k=1}^{N}\frac{1}{\sqrt{4\pi\lambda\beta}^D}\exp[-\frac{(x_{\mathcal{P}(k)}-x_k)^2}{4\lambda\beta}]. \quad (8.32)$$

In terms of permutation sectors this becomes

$$\langle\sum_{i<j}\delta(x^{(i)}-x^{(j)}-x)\rangle = \frac{1}{\mathcal{Z}_F^{(N)}(\beta)}\sum_{[p]}(-1)^{[p]}\int d^Dx_1\ldots d^Dx_N \sum_{i<j}\delta(x_i-x_j-x)\prod_{k=1}^{N}\frac{M_{[p]k}}{\sqrt{4\pi\lambda\beta}^D}\exp[-\frac{(x_{[p](k)}-x_k)^2}{4\lambda\beta}]. \quad (8.33)$$

We note that we only get a contribution to this sum if i and j are part of the same cycle. For each cycle length ℓ in permutation sector $[p]$, there are $C_{[p]\ell}\binom{\ell}{2}$ equal contributions. Finally we note that the integral over the δ-function gives an extra factor of $\sqrt{\frac{\ell}{\ell-1}}\exp[-\frac{\ell x^2}{4(\ell-1)\lambda\beta}]$. Thus we are left with,

$$\begin{aligned}
\langle g(x)\rangle &= \frac{1}{\mathcal{Z}_F^{(N)}(\beta)}\frac{2\Omega}{N^2}\sum_{[p]}(-1)^{[p]}\prod_{\ell=1}^{N}P_\ell(\beta)^{C_{[p]\ell}}M_{[p]k}\sum_{k=2}^{N}C_{[p]k}\binom{k}{2}\sqrt{\frac{k}{k-1}}\exp[-\frac{kx^2}{4(k-1)\lambda\beta}] && (8.34)\\
&= \frac{\mathcal{Z}_B^{(N)}}{\mathcal{Z}_F^{(N)}(\beta)}\frac{2\Omega}{N^2}\sum_{[p]}(-1)^{[p]}\omega_{[p]}\sum_{\ell=2}^{N}C_{[p]\ell}\binom{\ell}{2}\sqrt{\frac{\ell}{\ell-1}}\exp[-\frac{\ell x^2}{4(\ell-1)\lambda\beta}] && (8.35)\\
&\equiv \frac{1}{\langle\sigma\rangle}\frac{2\Omega}{N^2}\sum_{[p]}(-1)^{[p]}\omega_{[p]}\sum_{\ell=2}^{N}C_{[p]\ell}g_\ell(x;\beta) && (8.36)
\end{aligned}$$

where we have defined $g_\ell(x;\beta)$ as the pair correlation function within a cycle length ℓ at temperature β. Thus it is plausible that a similar reconstruction may be done for the pair correlation function as is done for the total energy and average value of the sign. Again the significance of this within the context of the sign problem in PIMC is that expectation values can be obtained by evaluating the N positive definite parameters $P_\ell(\beta)$ rather than the $N!$ terms in (8.1).

8.2 Permutations with interactions

All the above analysis is explicitly true for non-interacting systems. Thus, we now turn our attention to what happens when we include interactions. To do so, it is useful to take overview previous work by Feynman and Kikuchi in which they develop an intuitive picture of the permutation space of ^4He [41, 42, 62, 63].

In the mid 20th century Feynman presented a model for the λ transition in liquid ^4He [41, 42]. First recall the definition of the full partition function,

$$\mathcal{Z}^{(N)}(\beta) = \frac{1}{N!}\sum_{\mathcal{P}\in S_N}(-1)^{\mathcal{P}}\int d^Dx_1\ldots d^Dx_N(\prod_{i=1}^{N}\int_{x_i(0)}^{x_{\mathcal{P}(i)}(\hbar\beta)} d^Dx_i)\exp^{-\mathcal{A}^{(N)}/\hbar} \tag{8.37}$$

where the N-particle action is given by,

$$\mathcal{A}^{(N)} = \int_0^\beta d\tau\sum_{i=1}^{N}[\frac{1}{2}m\dot{x}_i^2 - \frac{1}{2}\sum_{j\neq i}^{N}V_{int}(x_i,x_j)]. \tag{8.38}$$

Leveraging the classical analogue of the path integral, one can imagine a particle i's path as its movement from one position $x_i(0)$ to another $x_i(\tau)$ in a time τ. Clearly if the velocity $\dot{x}_i(\tau)$ or potential $V_{int}(x_i(\tau),x_j(\tau))$ become large, the contribution to the total path integral will become negligible. For ^4He, the latter occurs when at time τ particles i and j are close together. If one now imagines a scenario where a particle i at position $x_i(0)$ permutes with particle j in time τ, such that

$$x_i(\tau) = x_j(0), \tag{8.39}$$

it must first navigate its way past other particles. We designate one such particle k at position $x_k(0)$ between $x_i(0)$ and $x_j(0)$. The only paths that contribute a non-negligible weight require particle i to avoid long paths to $x_i(\tau)$ which circumvent particle k at position $x_k(0)$. Instead particle k must jostle out of the way to $x_k(\tau)$. If we define

$$r \equiv x_i(\tau) - x_i(0), \tag{8.40}$$

then the number of particles that have to be jostled out of the way is $N_{aff} = r/a$ where a is the average interparticle spacing. Suppose also each of these particles is moved an amount d to avoid a large V_{int}. Then in a time τ, particle k must move out of the way with a velocity

$$\dot{x}_k = \frac{d}{\tau/N_{aff}}. \tag{8.41}$$

This makes the contribution to the action of all jostled particles

$$\int_0^\beta d\tau\sum_{k=1}^{N_{aff}}\frac{1}{2}m\dot{x}_k^2 \approx \frac{N_{aff}^2md^2}{2\beta} \tag{8.42}$$

$$= \frac{mr^2d^2}{2a^2\beta}. \tag{8.43}$$

By itself, particle i will contribute

$$\int_0^\beta d\tau \frac{1}{2} m\dot{x}_i^2 \approx \frac{mr^2}{2\beta}, \tag{8.44}$$

thus the total contribution of this permutation will be

$$\frac{m'r^2}{2\beta} \equiv \frac{mr^2 d^2}{2a^2\beta} + \frac{mr^2}{2\beta} \tag{8.45}$$

$$= \frac{m'r^2}{2\beta} \tag{8.46}$$

where we have defined an effective mass $m' \equiv (1 + (d/a)^2)m$.

Thus through the use of physical intuition granted by the path integral representation, Feynman was able to show the effect of the potential during a permutation is only to change the effective mass. This allows one to write down the many-body partition function as

$$\mathcal{Z}^{(N)}(\beta) \approx \frac{1}{N!} \sum_{\mathcal{P}} \int d^D x_1 \dots d^D x_N \rho_{int}(x_1, \dots, x_N; \beta) \prod_{i=1}^{N} \frac{1}{\sqrt{4\pi\lambda'\beta}^D} \exp\left[-\frac{(x_{\mathcal{P}(i)} - x_i)^2}{4\lambda'\beta}\right] \tag{8.47}$$

where the first term ρ is the potential contribution to the initial configuration and $\lambda' \equiv \hbar^2/2m'$. Now, as in the free gas case, we may assume that exchanges are essentially independent, allowing us to write the many-body partition function in terms of exchange frequencies P_l. At first glance this assumption may seem a large one, though it has been used before in another context. For quantum crystals, the Thouless theory of exchange in homogeneous systems assumes that at low temperatures the system will almost always be close to one of the $N!$ permutation sectors with rapid tunnelings between them [103]. With this in mind, we may write

$$\mathcal{Z}^{(N)}(\beta) = \frac{1}{N!} \sum_{[p]} \prod_{l=1}^{N} M_{[p]\ell} P_l(\beta)^{C_{[p]l}}. \tag{8.48}$$

This bears a remarkable resemblance to the free Fermi particle partition function of (8.14), except here $Z_0^{(1)}(l\beta)$ has been replaced by an exchange frequency $P_l(\beta)$ which includes an essentially mean-field effect of interactions and the sign has been dropped for bosons. Thus, we have again reduced the required simulation space from $N!$ to N.

Feynman takes this a step further, proposing an intuitive model for $P_l(\beta)$ for ^4He. Because of ^4He's the hard-sphere like interaction, one can assert that $\rho_{int} = 0$ if $(x_{[p](i)} - x_i)$ is less than the sphere width b and $\rho_{int} = 1$ otherwise. This forces the particles to be relatively evenly distributed throughout space and restricts permutations to only be between neighboring particles. The system can then be seen as particles

on a fixed lattice with permutations represented by forming closed polygons by connecting the lattice sites. Assuming the lattice interparticle separation is a, one can replace $(x_{[p](i)} - x_i)$ in (8.47),

$$\mathcal{Z}^{(N)}(\beta) \approx \frac{1}{N!}\sum_{\mathcal{P}'}\int d^D x_1 \ldots d^D x_N \rho_{int}(x_1,\ldots,x_N;\beta)\frac{1}{\sqrt{4\pi\lambda'\beta}^D}\exp\left[-\frac{a^2 n(\mathcal{P})}{4\lambda'\beta}\right] \tag{8.49}$$

$$= \frac{1}{N!}\sum_{\mathcal{P}'}\frac{1}{\sqrt{4\pi\lambda'\beta}^D}\exp\left[-\frac{a^2 n(\mathcal{P}')}{4\lambda'\beta}\right]\int d^D x_1 \ldots d^D x_N \rho_{int}(x_1,\ldots,x_N;\beta) \tag{8.50}$$

where the restricted sum $\sum_{\mathcal{P}'}$ is over all possible polygons on the lattice and $n(\mathcal{P})$ is the total number of sides in the set of polygons form by $\mathcal{P}'$.

Examining only the term in the sum, we have

$$\sum_{\mathcal{P}'}\exp\left[-\frac{a^2 n(\mathcal{P}')}{4\lambda'\beta}\right] = \sum_{[p]'} M_{[p]'}\prod_{\ell=1}^{N}\exp\left[-\frac{a^2\ell C_{[p]'\ell}}{4\lambda'\beta}\right]. \tag{8.51}$$

The primed quantities maintain their previous definitions, only now $[p]'$ defines sets of polygons that fit on the lattice, $C_{[p]'\ell}$ is the number of polygons with sides ℓ, and $M_{[p]'}$ is the number of permutations with $C_{[p]'\ell}$ polygons of ℓ sides. By assuming that the number of polygons with sides ℓ is independent of other polygons and that said polygons do not overlap, Feynman then chose to approximate $M_{[p]'}$ as a Poisson distribution,

$$M_{[p]'} = \prod_{\ell}\frac{R_\ell^{C_{[p]'\ell}}}{C_{[p]'\ell!}} \tag{8.52}$$

where R_ℓ is the number of ways to draw a polygon of sides ℓ. Finally if we define the relative probability of a pair-wise exchange to be

$$p_2(\beta) \equiv \exp\left[-\frac{a^2}{4\lambda'\beta}\right], \tag{8.53}$$

we arrive at the form

$$\mathcal{Z}^{(N)}(\beta) = \sum_{[p]} M_{[p]'}\prod_{l=1}^{N} p_2^{\ell C_{[p]'l}}(\beta). \tag{8.54}$$

Thus we have once again reduced the full problem to a single unknown parameter.

Feynman concludes his calculation by approximating the value of R_ℓ to arrive upon a many-body partition function that reproduces the qualitative features of λ transition of ^{4}He, though it failed to predict the actual discontinuity in the specific heat. Shortly after, Kikuchi improved this result by extending Feynman's short-range approximations for R_s and $M_{[p]'}$ to include the role of next-nearest neighbor interactions [62, 63]. In other words, Kikuchi was able to devise a more precise form for $P_\ell(\beta)$ to use in reconstructing the many-

body partition function which recovered the discontinuity in Feynman's original work. What we offer now is the next evolution of this improvement. Instead of trying to write down a more clever analytic form, we find it is possible precisely determine the best $P_\ell(\beta)$ through direct simulation. We note that this has been done previously for low density ^{3}He [23], however at this density the particles are treated as distinguishable without Fermi statistics.

8.3 Simulation details

When presenting the above analysis, Feynman mentions, "The above results apply only to Bose particles. Fermi particles behave differently" [43]. Luckily, in PIMC simulation of fermions, we actually simulate bosons and only keep tracking of the current overall sign as a weight, see (8.5). At the end of the simulation, we divide all observables by the expectation value of this weight, i.e. the average value of the sign $\langle\sigma\rangle$. As explained above, the variance in $\langle\sigma\rangle$ is the source of the sign problem, so any new approach to the sign problem must address it.

The first step in our approach to improving this variance is to measure and examine the probability of each permutation sector $\omega_{[p]}(\beta)$ as defined above. What we find is not so surprising: if the average value of the sign is on the order of or less than the lowest probability sectors, the variance of the sign is larger than its value. Our goal then is bring this line down below the order of the sign. Naively this is accomplished by simply running the simulation for longer and collecting more statistics, however as mentioned this process scales exponentially. A second simple approach is to truncate the sum over permutation sectors for successively smaller probabilities, eliminating the variance from the sectors with poor statistics. However if the average value of the sign is still much smaller than the value of truncation, this method will also fail. Instead we propose a new technique wherein the sectors with already good statistics are used to precisely fit the aforementioned models, moving from an $\mathcal{O}(N!)$ space to an $\mathcal{O}(N)$ or even $\mathcal{O}(1)$ one. This fitted model is then used to reconstruct the rest of the lower probability permutation sectors, thus moving the line well below that of the average value of the sign.

In order to empirically demonstrate this process can actually be used to reconstruct previously unattainable results, we apply it to the free Fermi gas where the analytic answer is known. In Fig. 8.2 we plot this process for a free Fermi gas. Measured permutation sector probabilities from direct PIMC simulation are plotted in blue. We see that the low probability sectors begin to form straight lines since during simulation they were only visited $1, 2, 3, \ldots$ times. For the temperature simulated, the average value of the sign $\langle\sigma\rangle$ is smaller than these smallest (unphysical) probabilities. To overcome this, we use least squares regression to

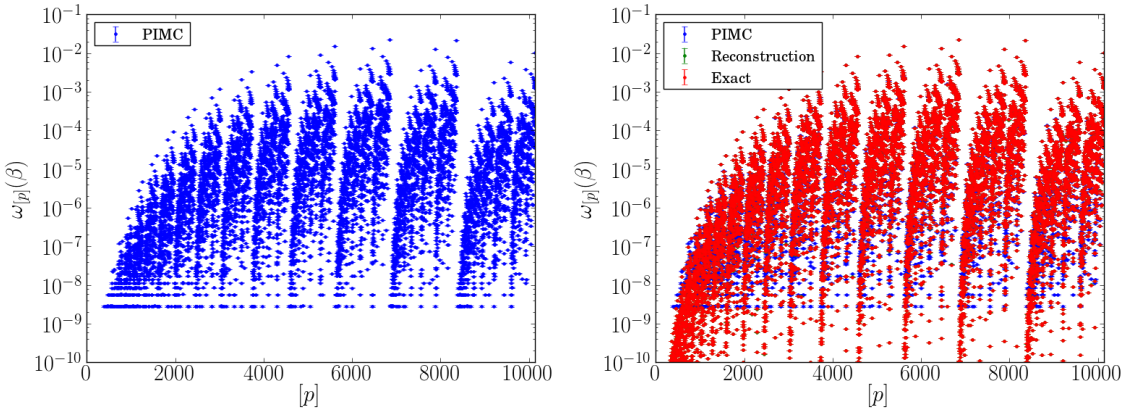

Figure 8.2: Permutation sector probabilities $\omega_{[p]}(\beta)$ for each permutation sector $[p]$ (trivially indexed) for a free Fermi gas of 33 particles at $r_s = 1.0$ and $\Theta = 0.125$. The blue points shown in both plots are from PIMC simulation. At the lowest probabilities the blue points form straight lines representing visiting those sectors $[p]$ only $1, 2, 3, \ldots$ times. The green points represent reconstructed values using the model (8.48). However, these points are perfectly masked by the exact analytical values, shown in red. One can see the reconstruction extends the permutation structure to orders of magnitude lower probabilities.

fit our model P_ℓ to reproduce the probabilities with the best statistics. In this example we use all sectors with probability $\omega_{[p]}(\beta) > 10^{-4}$. These fit values for P_ℓ are then used to reproduce the entirety of permutation space, shown in red. We see that the straight lines are replaced by the physical probabilities for those permutation sectors. Finally we plot the exact, analytic probabilities and find that they are completely recreated by our model.

We also attempt the same procedure by fitting the probability of a pairwise exchange $p_2 \equiv P_\ell^\ell$. For high temperature or large systems, this works well. However, for low temperature or small systems, the fit fails. For the free Fermi gas, this behavior precisely follows the large L limit of the one particle partition function defined in (8.20), i.e.

$$\lim_{L \gg 4\lambda\beta} \mathcal{Z}_0^{(1)}(\ell\beta) = \frac{\Omega}{\sqrt{4\pi\lambda l\beta}^D}. \tag{8.55}$$

Generally then, poor fitting to p_2 can be seen as a finite-size error since increasing N at a fixed density increases L. Alternatively, we can introduce a model that approximates the more general form of the free Fermi gas one particle partition function,

$$\mathcal{Z}_0^{(1)}(\ell\beta) = \sum_n \exp\left[-\ell\beta\lambda\left(\frac{2\pi n}{L}\right)^2\right], \tag{8.56}$$

though we do not see much of an improvement over simply fitting $Z_0^{(1)}(\ell\beta)$ itself.

Beyond measuring sector probabilities in simulation, we also measure the energy of each sector $E_{[p]}$. It

also follows the rule that rarely visited sectors have poor statistics and contribute mostly to the variance of the estimate. To account for this, we also attempt fitting the $N\ E_\ell$ values as defined in (8.26). Finally the total energy is computed according to (8.5). Again we attempt fitting to a single parameter, and again we find it to only work in the thermodynamic limit.

In essence, we have traded exponential cost for a linear or sub-linear scaling approximate method. It is certainly not obvious, however, that this procedure, motivated by the work of Feynman and Kikuchi, should be applicable to arbitrary interacting systems. What is incredible, is that the separability of permutation space is numerically verified for ^3He and the $3D$ homogeneous electron gas. Though we restrict ourselves to these two $3D$ systems, we believe this result generalizes to all homogeneous systems no matter the dimensionality. Extension to inhomogeneous systems, e.g. a hydrogen gas, is still an open question we are currently exploring.

8.4 Application to interacting, homogeneous systems

Through numerical simulation we find the same simple structure of the free many-body partition function is obeyed in strongly interacting systems. Our key finding is that, aside from small finite size effects, the contribution of a loop of length ℓ to the probability of a permutation sector is the same for all permutation sectors. This remarkable result implies that the full $N!$ permutation space can be written in terms of N parameters, leading to a dramatic reduction in the number of quantities necessary to converge a signed observable.

In what follows, we present detailed results of this approach applied to the homogeneous electron gas (HEG) and liquid ^{3}He. The character of exchange interactions in these two systems represent two qualitative extremes. In the HEG, a weak correlation hole results in a high probability of exchange between nearest neighbors. In contrast, ^{3}He has a strong correlation hole resulting in a significantly lower nearest neighbor exchange probability. As a consequence of its higher compressibility and higher exchange probability, the permutation structure of the HEG more closely resembles the noninteracting gas and the average value of the sign in the HEG, $\langle\sigma\rangle$, decays to zero more rapidly with decreasing temperature and increasing number of particles than in ^{3}He. Exact simulations of the HEG to date have been unable to extend to temperatures lower than the Fermi energy, as seen in Chapter 5. In this work we have found the free gas $\omega_{[p]}$ is an excellent representation of the HEG permutation sector structure. The strong correlation hole in ^{3}He has the effect of modifying the combinatorial factor, $M_{[p]\ell}$, in (8.17) for a finite simulation box requiring the addition of a model to account for the absence of overlapping exchange loops.

8.4.1 ^{3}He

^3He has a strong correlation hole and is, like its bosonic analogue ^{4}He, often modeled as a system of hard-spheres. This makes sampling permutation space a difficult task since particles are not likely to become close enough to permute. In the past this has been overcome by the use of the grand-canonical *worm algorithm* [12, 13]. Though not reviewed here, the worm algorithm breaks a single path loop, effectively sampling the off-diagonal components of the many-body density matrix and for ^{3}He is able to generate permuting configurations more efficiently than the canonical method described in Chapter 2.

It has been shown that for weakly interacting systems at low temperatures, the probability of permutations becomes proportion to their length [55]. Indeed we see this behavior in simulating ^{3}He. Figure 8.3 shows the observed probability of finding a particle participating in a permutation cycle of length k, $kP(k)$, at $T = 0.5$ Kelvin for $N = 66$ identical ^{3}He atoms in a periodic box with density 0.016355 Å^{-3} (as represented by the phenomenological Aziz-2 potential [5]). The figure shows a clear plateau in the region extending from $12 < k < 37$. The drop-off in $kP(k)$ for $k > 36$ is a consequence of the reduction in the number of ways long loops can be formed when N is finite and appears in the finite noninteracting gas as well for any $T > 0$. Since their probabilities are roughly equal at low temperatures, in general we find sectors containing long permutations of ^{3}He to be very low probability and consequently are main generators of variance in the average value of the sign. Because of this, we find that we can gather better statistics through importance sampling of short permutations by simply penalizing permutations proportionally to their length and dividing out this penalty after simulation.

Since during simulation, we sample a bosonic analogue density matrix of ^{3}He, it seems the most obvious to attempt to fit our measured permutation probabilities to the form for ^{4}He motivated by Feynman and Kikuchi of (8.54). In accordance, we attempt to use a combinatorial factor $M_{[p]\ell}$ of (8.17) which resembles a Poisson distribution as proposed by Feynman for ^{4}He. Alternatively, we also determine precise values for $M_{[p]\ell}$, by numerically solving for probabilities of the lattice permutation ^{4}He lattice model. For this method, which we term an *inverse Ising model*, we simply solve for the probability to form permuting polygons on a finite lattice which each site representing a single particle. For both of these possible combinatorial factors, we then use our simulation data to fit the pairwise exchange probability p_2.

Figure 8.4 shows the fitted values of p_2 for a range of permutation sectors for $N = 66$ ^{3}He at $T = 1.2$ Kelvin. Solid squares in the figure show results for p_2 obtained based on an uncorrected Poisson model. The statistically significant drift in the mean value of p_2 with increasingly long permutation cycles resulting from use of Feynman's Poisson model is evident. It is possible that this is an expression of a finite size error since the Poisson model is only correct in the thermodynamic limit. In contrast, results for p_2 obtained from the

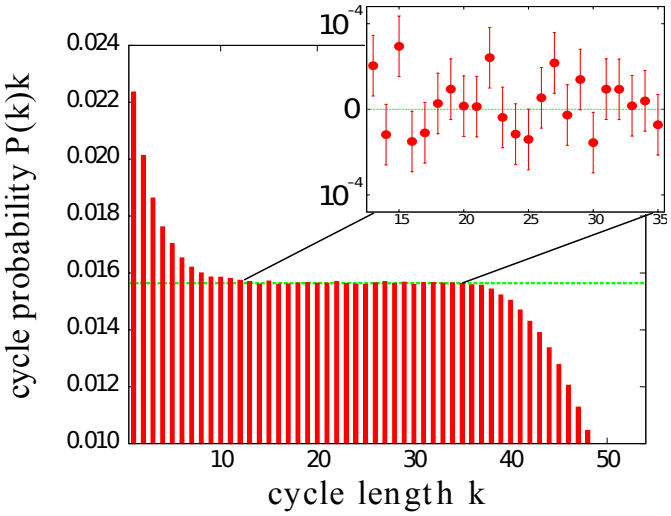

Figure 8.3: Cycle probability times cycle length for spin polarized bosonic ^{3}He at $T = 0.5K$ with $N = 66$ atoms [105]. Inset shows the extended flat region of the distribution which allows higher order permutation sectors to be ignored. The large contribution of non-permuting paths ($P(k = 1) = 0.202$) is not shown so that the small contribution of short cycles $k < 12$ can be seen clearly. The inset shows the small deviation of the observed probability from the mean value between $k = 13$ and $k = 36$.

inverse Ising model are found to agree with the mean value obtained over all sectors within statistical error bars ($\approx 1\%$). The mean value of p_2 obtained in this way was used to weight expectation values over the full antisymmetrized density matrix. Our choice for the lattice is somewhat ad hoc in the sense that a square lattice is assumed, where each He atom has 6 nearest neighbors whereas if we had assumed an HCP lattice it would have 12 neighbors. However, we have found that while the choice of lattice will change the mean extracted value of p_2 somewhat, the reconstructed values of $\omega_{\mathcal{P}}$ do not depend significantly on the choice of lattice, being insensitive to the detailed form of the lattice for the temperatures we have considered.

Results of the antisymmetrized grand canonical PIMC applied to liquid ^{3}He are shown in Figure 8.5. Results from direct (truncated) summation over permutations (solid circles) agree well with experimental data [49] (dashed line) down to temperatures well below the ^{3}He Fermi temperature, $T_f = 1.7K$. The reconstructed energies obtained using the inverse Ising model are represented as open triangles. Results for the reconstructed energies were obtained with an ≈ 2 order of magnitude reduction in computational cost compared to the truncated results and agree to within statistical error bars with the experimental values as opposed to the approximation introduced by the restricted path method [20].

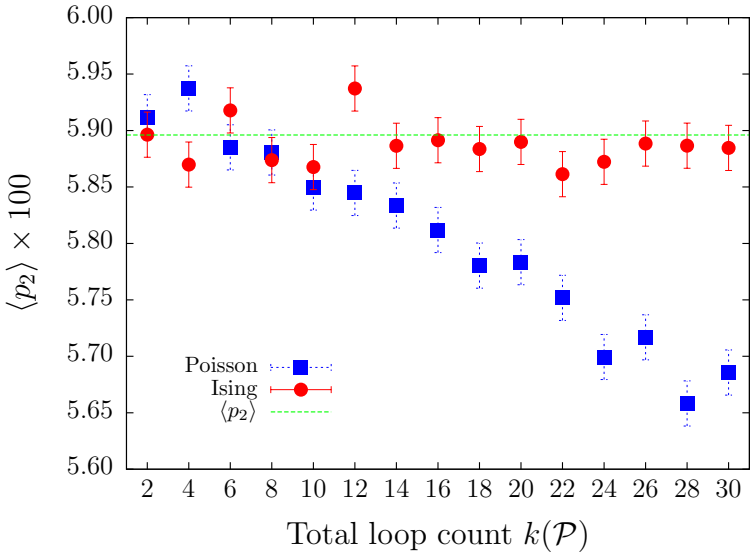

Figure 8.4: Representative values of the extracted pair exchange probability p_2 across a representative subset of equivalence classes containing increasingly long loops using Poisson statistics (squares) and the numerically inverted Ising model (circles) [105]. The dashed line shows the mean value $\langle p_2 \rangle$ over all sectors obtained via the numerical lattice method.

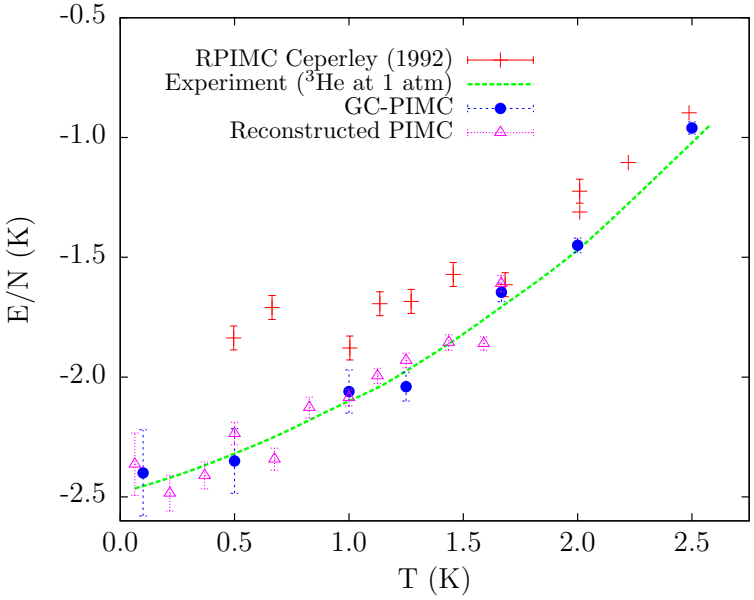

Figure 8.5: Results of antisymmetrized grand canonical PIMC applied to liquid ^{3}He [105]. For $N = 66$ spin-unpolarized ^3He, our direct results (solid circles) and the reconstructed energies described in the text (open triangles) agree well with experimental data (dashed line) down to temperatures well below the ^{3}He Fermi temperature. Results obtained with restricted PIMC with free particle nodes from Ref. [20] (+ signs) are shown for comparison.

r_s	T/T_F	$PIMC$	$RPIMC$	P_l	p_2
1.0	0.125	1(10)	2.35(1)	2.3(1)	2.33(6)
1.0	1.0	3(7)	8.69(3)	8.7815(7)	8.7801(7)
10.0	0.125	−0.0(1)	−0.1038(2)	−0.1030(1)	−0.1033(1)
10.0	1.0	−0.040(2)	−0.0403(5)	−0.0402(1)	−0.04025(5)

Table 8.1: Total energies per particle for 33 spin-polarized electrons at $r_s = 1$, 10 and $T/T_F = 0.125$, 1.0. From left to right, we plot energy estimates for standard signful PIMC, restricted PIMC from Chapter 5, reconstructed PIMC using P_ℓ as in (8.17), and reconstructed PIMC using p_2.

8.4.2 Homogeneous electron gas

The HEG has a much weaker correlation hole and long-ranged interactions than ^3He. For this reason, we find the simple canonical PIMC sampling of permutations to work well. For the same reason, however, permutations are much more prevalent, and the sign problem in the HEG is much worse, resembling that of a free Fermi gas. In Chapter 5, we presented some exact, signful simulations of the HEG, but were unable to extend to temperatures lower than the Fermi energy. On the other hand, it is because of this resemblance that we have found the free gas combinatorial factor $M_{[p]\ell}$ to be an excellent representation of the HEG permutation sector structure. The finite-size effects present in the study of ^{3}He are still present in the HEG reconstruction. However, we have found that the cycle lengths with P_ℓ values that deviate most from p_2, contribute naturally to the most probable sectors. Because of this, we are able to avoid both the need to importance sample as well as the need to use an inverse Ising model.

In confirmation of this idea, we have examined both a low density ($r_s = 10$) and high density ($r_s = 1$) state of the HEG both at the T_F and at 1/8 T_F. In Table 8.1, we give energies of the HEG for these two densities and temperatures with the previous exact and fixed-node results of Chapter 5. We find that our reconstructed energies, both by fitting p_2 and P_ℓ directly, match well with previous fixed-node results. Importantly, however, we note that this new method extends the regime where unbiased exact simulations are possible. Previous exact simulations were not possible below the Fermi temperature, giving estimates for the energy with a variance larger than the value itself, while both reconstructions work well at 1/8 T_F. For some of the points examined, we see up to $\sim 1\%$ discrepancies with the fixed-node result. We speculate this to difference to be due to the fixed-node approximation, making these new results more accurate. Between fitting p_2 and P_ℓ, we see essentially negligible differences.

8.5 Conclusions and prospects

We have thus shown that it is possible to directly address the sign problem for homogeneous systems by taking advantage of their relatively simple permutation space structure. Though here, we only plot energies,

other diagonal observables may be accessed in the same way. Current efforts are focused on reconstructing off-diagonal quantities like the Fourier transform of the momentum distribution which exemplifies the fermionic nature of the superfluid transition. We are also interested in reconstructing the permutation space of inhomogeneous systems in the hope that we can also exactly calculate properties of general many-body Fermion systems much below the Fermi temperature.

In a general interacting system, the simple N parameter does not necessarily hold as the relative probability of different cycle lengths P_ℓ can in general depend on the permutation sector $[p]$. It is reasonable, however, to construct a general expression for a sector dependent $P_{[p]\ell}$ as an expansion around an averaged $\bar{P}_\ell$ such that

$$\begin{aligned} P_{[p]\ell}/\bar{P}_\ell = \quad & 1 + \textstyle\sum_{m=1}^{N} C_{[p]m}(\frac{\bar{P}_{\ell m}}{\bar{P}_\ell} - 1) + \\ & \textstyle\sum_{m,n=1}^{N} C_{[p]m}C_{[p]n}(\frac{\bar{P}_{\ell mn}}{\bar{P}_\ell} - 1) + \ldots \end{aligned} \tag{8.57}$$

where $\bar{P}_{\ell m\ldots}$ is related to the probability of finding a cycle length ℓ given the existence of cycles of length $m\ldots$. Clearly in the above cases of ^{3}He and the HEG, setting all higher order terms to zero is sufficient to reproduce diagonal observables. On the other hand, it is reasonable to suspect that for inhomogeneous systems, higher order terms will be required. If there is still a truncation to this series, however, the computational complexity of the algorithm will still be better than exponential, scaling as $\mathcal{O}(N^m)$ where m is the required order of the expansion.

Appendix A

Coulomb pair actions

In this appendix, we seek to provide a resource for derivations and properties pertaining to the Coulomb pair action. We focus mainly on the $3D$ case, and will be using energy units of Rydbergs. For $D = 2$, we refer to the reader to Ref. [93].

To begin, we recall it is often convenient to express the Coulomb pair action as a sum over partial waves, such that

$$\rho(r, r'; \tau) = \frac{1}{4\pi r r'} \sum_{l=0}^{\infty} (2l+1) \rho_l(r, r', \tau) P_l(cos(\theta)) \tag{A.1}$$

where P_l are Legendre polynomials and θ is the angle between r and r'.

Each $rho_l(r, r'; \tau)$ can then written as a sum over states with

$$\rho_l(r, r'; \tau) = \sum_i \Psi^{\dagger}_{i,l}(r) \Psi_{i,l}(r') \exp\left[-\tau E_{i,l}\right] + \int_0^{\infty} dk \Psi_{k,l}(r)^{\dagger} \Psi_{k,l}(r') \exp\left[-\tau E_{k,l}\right] \tag{A.2}$$

representing both bound and continuum states, respectively.

Supposing the interacting is between two species with atomic numbers Z_1 and Z_2 and reduced mass μ, we can define the constants,

$$\lambda \equiv \frac{1}{2\mu} \tag{A.3}$$

$$Z \equiv Z_1 Z_2 / \lambda. \tag{A.4}$$

Then the radial bound state wavefunctions can be written,

$$\Psi_{i,l}(r) = C_{i,l} \exp\left(-\frac{r|Z|}{2i}\right) r^l L^{2l+1}_{i-l-1}(fracr|Z|i) \tag{A.5}$$

where the L are generalized Laguerre polynomials and the C are normalization constants given by

$$C_{i,l} = (\frac{|Z|}{i})^{l+3/2}\sqrt{\frac{(i-l-1)!}{(2i)(i+1)!}}. \tag{A.6}$$

The bound state energies are given by

$$E_i = -\frac{\lambda Z^2}{4i^2}. \tag{A.7}$$

The radial continuum wavefunctions can be written,

$$\Psi_{k,l}(r) = \sqrt{\frac{2}{\pi}}F_l(\frac{Z}{2k}, kr)/r \tag{A.8}$$

where F_l is the usual Coulomb wavefunction given in [2]. The excited state energies are given simply by

$$E_k = \lambda k^2. \tag{A.9}$$

It has been shown that it is possible to derive the full density matrix from the s-wave term alone, often dubbed the *s-wave miracle* [93]. This fact suggests a change of coordinates to

$$x \equiv (r + r' + |r - r'|)/2 \tag{A.10}$$

$$y \equiv (r + r' - |r - r'|)/2. \tag{A.11}$$

Putting these together with (A.2), we find that

$$\rho_l(r, r'; \tau) = \rho_l^b(r, r'; \tau) + \rho_l^c(r, r'; \tau) \tag{A.12}$$

where

$$\rho_l^b(r, r'; \tau) = \frac{1}{4\pi|r - r'|}\sum_i e^{-\tau E_i}|C_i^0|^2\frac{n^3}{|Z|}e^{-(|Z|/2i)(r+r')}(L_{i-1}^0(\frac{|Z|x}{i})L_i^0(\frac{|Z|y}{i}) - L_{i-1}^0(\frac{|Z|y}{i})L_i^0(\frac{|Z|x}{i})) \tag{A.13}$$

and

$$\rho_l^c(r, r'; \tau) = \frac{1}{2\pi^2|r - r'|}\int dk e^{-\tau E_k}[F_0(\frac{Z}{2k}; kx)F_0'(\frac{Z}{2k}; ky) - F_0(\frac{Z}{2k}; ky)F_0'(\frac{Z}{2k}; kx)]. \tag{A.14}$$

Both these equations may be computed numerically, however, it is often more convenient to only do so for the repulsive case in which there are no bound states. To find the corresponding attractive solution, first fit

the repulsive case to a form like,

$$\rho_l(r,r';\tau) = rho_{l,free}(r,r';\tau)\exp -\sum_{j=1}^{\infty} U_j(\frac{r}{\sqrt{\lambda\tau}},\frac{r'}{\sqrt{\lambda\tau}};Z\sqrt{\lambda\tau}), \tag{A.15}$$

where U_j is a rapidly converging in $Z\sqrt{\lambda\tau}$. Then the attractive solution is simply the same expansion with the sign changed on the odd powers.

As an example of the above expansion technique, we can look at the cusp condition, i.e. $r = r' = 0$. At the origin, only the $l = 0$ contribution remains, allowing us to write

$$\rho(0,0;\tau) = \frac{|Z|^3}{2\pi}\int_0^{\infty} dk \frac{ke^{-\gamma k^2}}{e^{\pi/k}-1} \tag{A.16}$$

$$= \frac{|Z|^3}{(4\pi\gamma)^{3/2}}[1-(\pi\gamma)^(1/2) + \sum_{j=0}^{\infty}\frac{(-1)^j}{j!}(\frac{j}{2})!\zeta(j+2)\gamma^{j/2+1}] \tag{A.17}$$

where $\gamma =\equiv |Z|\lambda\tau$ and ζ is the Riemann zeta function. We compare this to a cumulant expansion,

$$1+\sum_{j=1}^{\infty}\frac{\mu_j t^j}{j!} = \exp(\sum_{n=1}^{\infty}\frac{\kappa j t^j}{j!}) \tag{A.18}$$

where the cumulants κ_j are related to the moments μ_j via the recursion relation

$$\kappa_j = \mu_j - \sum_{i=1}^{j-1}\binom{j-1}{i-1}\kappa_i\mu_{j-i}. \tag{A.19}$$

We see that in this instance, if we write

$$\mu_j = \frac{1}{(j+2)!}(\frac{j+2}{2})!\zeta(j), \tag{A.20}$$

with $\mu_1 = -\sqrt{\pi}$, the recursion relation holds. We may then write the exact cusp condition as

$$\rho_l(0,0;\tau) = \frac{|Z|^3}{(4\pi\gamma)^{3/2}}\exp(-\sum_{j=1}^{\infty}\kappa_j\gamma^{j/2}). \tag{A.21}$$

For the attractive case, simply replace all the odd terms with their negative. To be concrete, we give several values for the cumulant coefficients κ_j in Table A.1.

Other limiting properties are apparent from the above form. The next order term near the origin is given by,

$$\lim_{r,r'\to 0}\rho_l(r,r';\tau) = \rho_l(0,0;\tau)\exp -[\frac{Z}{2}(r+r')] \tag{A.22}$$

Table A.1: Cumulant coefficients κ_j.

κ_1	1.77245385091
κ_2	0.0741377400533
κ_3	0.00583480451282
κ_4	0.000382686412738
κ_5	$8.7380485818e-06$
κ_6	$2.13783515523e-06$
κ_7	$3.56034303663e-07$
κ_8	$2.07958135737e-08$
κ_9	$1.91042959407e-09$
κ_{10}	$5.68660748412e-10$

where the second term is the $1s$ contribution to the density matrix. This makes the cusp condition on the derivative

$$\lim_{r,r'\to 0} \rho_l(r,r';\tau) = -\frac{Z}{2}\rho_l(0,0;\tau)\exp -[\frac{Z}{2}(r+r')]. \tag{A.23}$$

Finally in the small time-step limit, we know the pair approximation to be true on the diagonal such that

$$\lim_{\tau\to 0} \rho_l(r,r;\tau) = \frac{|Z|^3}{(4\pi\gamma)^{3/2}}\exp -\frac{Z\lambda\tau}{r}. \tag{A.24}$$

Appendix B

Algorithm

The PIMC algorithm at its highest level is fairly straightforward. As mentioned in Chapter 2, it contains many of the same features found in most QMC algorithms, including statistical blocking and a Metropolis rejection step. The actual codebase currently resides on github at `http://github.com/ethan/pimcpp`. Here we present its pseudocode. Note that here R represents the MND-dimensional space where M is the number of time slices, N is the number of particles, and D is the physical dimension of the simulation box. Since the real code is written using object oriented best principles, each move $\mathcal{M}$ and observable $\mathcal{O}$ is represented as an object in a vector of moves $\{\mathcal{M}\}$ and observables $\{\mathcal{O}\}$, respectively.

Algorithm 1 PIMC algorithm in psuedocode.

$R \leftarrow R_0$ ▷ Initialized all M beads of all N particles in space.
for $i := 1 \rightarrow N_{equil}$ **do** ▷ Loop over N_{equil} steps.
  for $\mathcal{M} \in \{\mathcal{M}\}$ **do** ▷ Loop over moves.
    $\mathcal{M}(R \rightarrow R')$ ▷ Sample new configuration.
    if $A(R \rightarrow R') \geq rand(0,1)$ **then** ▷ Check acceptance ratio against uniform random number.
      $R \leftarrow R'$ ▷ Accept new configuration.
    end if
  end for
end for
for $i := 1 \rightarrow N_{block}$ **do** ▷ Loop over N_{block} blocks.
  for $j := 1 \rightarrow N_{step}$ **do** ▷ Loop over N_{step} steps within block.
    for $\mathcal{M} \in \{\mathcal{M}\}$ **do** ▷ Loop over moves.
      $\mathcal{M}(R \rightarrow R')$ ▷ Sample new configuration.
      if $A(R \rightarrow R') \geq rand(0,1)$ **then** ▷ Check acceptance ratio against uniform random number.
        $R \leftarrow R'$ ▷ Accept new configuration.
      end if
    end for
    for $\mathcal{O} \in \{\mathcal{O}\}$ **do** ▷ Loop over observables.
      if $j \mod f_{\mathcal{O}} == 0$ **then** ▷ Each observable will has its own measurement frequency, $f_{\mathcal{O}}$.
        $\mathcal{O}_{tot} \leftarrow \mathcal{O}_{tot} + \mathcal{O}(R)$, $N_{\mathcal{O}} \leftarrow N_{\mathcal{O}} + 1$ ▷ Compute observable and add to total
      end if
    end for
  end for
  for $\mathcal{O} \in \{\mathcal{O}\}$ **do** ▷ Loop over observables.
    $\langle \mathcal{O} \rangle \leftarrow \mathcal{O}_{tot}/N_{\mathcal{O}}$ ▷ Average observable and write to disk.
    $\mathcal{O}_{tot} \leftarrow 0$, $N_{\mathcal{O}} \leftarrow 0$ ▷ Reset total.
  end for
end for

Appendix C

Fermion Nodes

In this appendix we prove the tiling theorem for the fixed-node constraint for path integrals. This implies it is possible to access the entire positive region defined by the nodes of many-body partition function.

Recall the many-body density matrix may be defined as the solution to the Bloch equation. For fermions this takes the form

$$-\frac{d}{d\beta}\rho_F(R,R';\beta)=\hat{\mathcal{H}}\rho_F(R,R';\beta) \tag{C.1}$$

with the initial condition $\rho_F(R,R';0)=\hat{\mathcal{A}}\delta(R-R')$ where $\hat{\mathcal{A}}$ is the anti-symmetrization operator. The fixed-node method for path integrals supplants this initial condition with zero boundary conditions.

Recall in Chapter 3, to prove uniqueness of this solution, we supposed there are two solutions to the Bloch equation $\rho_1(R,R^\star;\tau)$ and $\rho_2(R,R^\star;\tau)$ which both satisfy the zero boundary condition at t_1. We may then define a third function $\phi\equiv\rho_1-\rho_2$ which clearly also solves the Bloch equation with the same boundary conditions,

$$0 \quad = \quad (\hat{\mathcal{H}}+\frac{d}{d\tau})\phi(R,R^\star;\tau). \tag{C.2}$$

Recalling that $\hat{\mathcal{H}}=-\lambda\nabla_R^2+V(R)$, we can write

$$0 \quad = \quad \int_{t_1}^{t_2}d\tau\int dR e^{2V_0\tau}\phi(R,R^\star;\tau)(-\lambda\nabla_R^2+V(R)+\frac{d}{d\tau})\phi(R,R^\star;\tau) \tag{C.3}$$

where V_0 is defined as a lower bound to the potential $V(R)$. Recall to integrate by parts,

$$\int_a^b dx u(x)v'(x)dx=u(x)v(x)|_a^b-\int_a^b u'(x)v(x)dx. \tag{C.4}$$

Performing this on (C.3) and enforcing the zero boundary condition, we find

$$0 = \int dR \frac{e^{2V_0 t_2}}{2} \phi(R, R^\star; t_2)^2 \tag{C.5}$$

$$+ \int dR \int_{t_1}^{t_2} d\tau \{(V(R) - V_0) e^{2V_0 \tau} \phi(R, R^\star; \tau)^2 \tag{C.6}$$

$$- e^{2V_0 \tau} \phi(R, R^\star; \tau) \nabla_R^2 \phi(R, R^\star; \tau) - e^{2V_0 \tau} \phi(R, R^\star; \tau) \frac{\partial}{\partial \tau} \phi(R, R^\star; \tau)\}. \tag{C.7}$$

Next we recall Stokes theorem which relates an integral over the volume Ω to one over the surface of that volume Γ,

$$\int_\Omega d\Omega u \nabla^2 v = -\int_\Omega d\Omega \nabla u \cdot \nabla v + \int_\Gamma d\Gamma u \nabla v \cdot \hat{n}. \tag{C.8}$$

Applying this to (C.7) and again enforcing the zero boundary condition, we find

$$0 = \int dR \frac{e^{2V_0 t_2}}{2} \phi(R, R^\star; t_2)^2 \tag{C.9}$$

$$+ \int dR \int_{t_1}^{t_2} d\tau \{(V(R) - V_0) e^{2V_0 \tau} \phi(R, R^\star; \tau)^2 \tag{C.10}$$

$$+ e^{2V_0 \tau} (\nabla_R \phi(R, R^\star; \tau))^2 - e^{2V_0 \tau} \phi(R, R^\star; \tau) \frac{\partial}{\partial \tau} \phi(R, R^\star; \tau)\}. \tag{C.11}$$

We then recognize that the final term is the same as the one used in the integration by parts. Thus through substitution, we find,

$$0 = \int dR \frac{e^{2V_0 t_2}}{2} \phi(R, R^\star; t_2)^2 \tag{C.12}$$

$$+ \int dR \int_{t_1}^{t_2} d\tau \{(V(R) - V_0) e^{2V_0 \tau} \phi(R, R^\star; \tau)^2 + e^{2V_0 \tau} (\nabla_R \phi(R, R^\star; \tau))^2\}. \tag{C.13}$$

Since each term is positive, we immediately realize that $\phi(R, R^\star; \tau) = 0$ and thus $\rho_1 = \rho_2$. Therefore the zero boundary condition defines a unique solution to the Bloch equation.

Now suppose that the tiling property does not hold. Then there exists a region in the configurational space with a non-zero density matrix from which no path extends to $R^\star$ or any of its permutations $\mathcal{P}R^\star$ without crossing a node. On the contrary, in the classical limit , we know the tiling theorem must hold since only a single permutation exists. Thus this hypothetical domain cannot extend to $t_1 = 0$. Therefore, for some $t_1 > 0$, the zero boundary condition holds, making the domain vanish completely, contradicting our original assumption. Thus through reducio ad absurdum, we have shown that the tiling property holds.

References

[1] R. Abe. Giant Cluster Expansion Theory and Its Application to High Temperature Plasma. Progress of Theoretical Physics, 22:213–226, August 1959.

[2] M. Abramowitz and I. Stegun. Handbook of Mathematical Functions. Dover Publications, 1965.

[3] Angel Alastuey and Asher Perez. Virial expansions for quantum plasmas: Fermi-bose statistics. Phys. Rev. E, 53:5714–5728, Jun 1996.

[4] P.W. Anderson. Random-phase approximation in the theory of superconductivity. Phys.Rev., 112:1900–1916, 1958.

[5] R. A. Aziz, V. P. S. Nain, J. S. Carley, W. L. Taylor, and G. T. McConville. An accurate intermolecular potential for helium. J. Chem. Phys., 70(9):4330–4342, 1979.

[6] L. Baguet, F. Delyon, B. Bernu, and M. Holzmann. Properties of Hartree-Fock solutions of the three-dimensional electron gas. ArXiv e-prints, April 2014.

[7] J. Bardeen, L. N. Cooper, and J. R. Schrieffer. Theory of superconductivity. Phys. Rev., 108:1175–1204, Dec 1957.

[8] C. H. Bennett. Efficient estimation of free energy differences from Monte Carlo data. Journal of Computational Physics, 22:245–268, October 1976.

[9] F. Bloch. The electron theory of ferromagnetism and electrical conductivity. Z. Physik, 57:545–555, 1929.

[10] David Bohm and David Pines. A collective description of electron interactions: Iii. coulomb interactions in a degenerate electron gas. Phys. Rev., 92:609–625, Nov 1953.

[11] M. Boninsegni. Permutation Sampling in Path Integral Monte Carlo. Journal of Low Temperature Physics, 141:27–46, October 2005.

[12] M. Boninsegni, N. V. Prokof'ev, and B. V. Svistunov. Worm algorithm and diagrammatic monte carlo: A new approach to continuous-space path integral monte carlo simulations. Phys. Rev. E, 74:036701, Sep 2006.

[13] Massimo Boninsegni, Nikolay Prokof'ev, and Boris Svistunov. Worm algorithm for continuous-space path integral montecarlo simulations. Phys. Rev. Lett., 96:070601, Feb 2006.

[14] Ethan W. Brown, Bryan K. Clark, Jonathan L. DuBois, and David M. Ceperley. Path-integral monte carlo simulation of the warm dense homogeneous electron gas. Phys. Rev. Lett., 110:146405, Apr 2013.

[15] W. J. Carr, Rosemary A. Coldwell-Horsfall, and A. E. Fein. Anharmonic contribution to the energy of a dilute electron gas¯interpolation for the correlation energy. Phys. Rev., 124:747–752, Nov 1961.

[16] W. J. Carr and A. A. Maradudin. Ground-state energy of a high-density electron gas. Phys. Rev., 133:A371–A374, Jan 1964.

[17] R. Cauble, D.K. Bradley, P.M. Celliers, G.W. Collins, L.B. Da Silva, and S.J. Moon. Experiments using laserdriven shockwaves for eos and transport measurements. Contributions to Plasma Physics, 41(2-3):239–242, 2001.

[18] D. Ceperley. Ground state of the fermion one-component plasma: A monte carlo study in two and three dimensions. Phys. Rev. B, 18:3126–3138, Oct 1978.

[19] D. Ceperley, G. V. Chester, and M. H. Kalos. Monte carlo simulation of a many-fermion study. Phys. Rev. B, 16:3081–3099, Oct 1977.

[20] D. M. Ceperley. Path-integral calculations of normal liquid ^{3}He. Phys. Rev. Lett., 69:331–334, 1992.

[21] D. M. Ceperley. Path integrals in the theory of condensed helium. Rev. Mod. Phys., 67:279–355, Apr 1995.

[22] D. M. Ceperley and B. J. Alder. Ground state of the electron gas by a stochastic method. Phys. Rev. Lett., 45:566–569, Aug 1980.

[23] D. M. Ceperley and G. Jacucci. Calculation of exchange frequencies in bcc ^{3}He with the path-integral monte carlo method. Phys. Rev. Lett., 58:1648–1651, Apr 1987.

[24] David Ceperley. Path integral monte carlo methods for fermions. In K. Binder and G. Ciccotti, editors, Monte Carlo and Molecular Dynamics of Condensed Matter Systems. Italian Physical Society, Singapore, 1996.

[25] D.M. Ceperley. Fermion nodes. Journal of Statistical Physics, 63(5-6):1237–1267, 1991.

[26] G Chabrier, F Douchin, and A Y Potekhin. Dense astrophysical plasmas. Journal of Physics: Condensed Matter, 14(40):9133, 2002.

[27] Simone Chiesa, David M. Ceperley, Richard M. Martin, and Markus Holzmann. Finite-size error in many-body simulations with long-range interactions. Phys. Rev. Lett., 97:076404, Aug 2006.

[28] Bryan Clark. Strongly correlated systems through quantum Monte Carlo. PhD thesis, University of Illinois at Urbana-Champaign, 2009.

[29] R. G. Dandrea, N. W. Ashcroft, and A. E. Carlsson. Electron liquid at any degeneracy. Phys. Rev. B, 34:2097–2111, Aug 1986.

[30] Hans De Raedt and Bart De Raedt. Applications of the generalized trotter formula. Phys. Rev. A, 28:3575–3580, Dec 1983.

[31] P. Debye and E. Hückel. Zur Theorie der Elektrolyte. I. Gefrierpunktserniedrigung und verwandte Erscheinungen. The theory of electrolytes. I. Lowering of freezing point and related phenomena. Physikalische Zeitschrift, 24:185–206, 1923.

[32] M. W. C. Dharma-wardana and F. Perrot. Simple classical mapping of the spin-polarized quantum electron gas: Distribution functions and local-field corrections. Phys. Rev. Lett., 84:959–962, Jan 2000.

[33] P. A. M. Dirac. The quantum theory of the electron. Proceedings of the Royal Society of London. Series A, 117(778):610–624, 1928.

[34] N. D. Drummond and R. J. Needs. Quantum monte carlo calculation of the energy band and quasi-particle effective mass of the two-dimensional fermi fluid. Phys. Rev. B, 80:245104, Dec 2009.

[35] N. D. Drummond, R. J. Needs, A. Sorouri, and W. M. C. Foulkes. Finite-size errors in continuum quantum monte carlo calculations. Phys. Rev. B, 78:125106, Sep 2008.

[36] Sandipan Dutta and James Dufty. Classical representation of a quantum system at equilibrium: Applications. Phys. Rev. E, 87:032102, Mar 2013.

[37] Helmut Eschrig. T¿0 ensemble-state density functional theory via legendre transform. Phys. Rev. B, 82:205120, Nov 2010.

[38] Kenneth P. Esler. Advancements in the path integral Monte Carlo method for many-body quantum systems at finite temperature. University of Illinois at Urbana-Champaign, PhD Thesis, 2006.

[39] P. P. Ewald. Die berechnung optischer und elektrostatischer gitterpotentiale. Ann. Physik, 369:253–287, 1921.

[40] E. Fermi. Application of statistical gas methods to electronic systems. Rendiconti dell'Accademia Nazionale dei Lincei, 6:602–607, 1927.

[41] R. P. Feynman. Atomic theory of liquid helium near absolute zero. Phys. Rev., 91:1301–1308, Sep 1953.

[42] R. P. Feynman. Atomic theory of the transition in helium. Phys. Rev., 91:1291–1301, Sep 1953.

[43] Richard Feynman. Statistical Mechanics: A Set of Lectures. Westview Press, New York, USA, 1998.

[44] K. Fuchs. A Quantum Mechanical Investigation of the Cohesive Forces of Metallic Copper. Royal Society of London Proceedings Series A, 151:585–602, October 1935.

[45] Murray Gell-Mann. Specific heat of a degenerate electron gas at high density. Phys. Rev., 106:369–372, Apr 1957.

[46] Murray Gell-Mann and Keith A. Brueckner. Correlation energy of an electron gas at high density. Phys. Rev., 106:364–368, Apr 1957.

[47] Paola Gori-Giorgi and John P. Perdew. Pair distribution function of the spin-polarized electron gas: a first-principles analytic model for all uniform densities. Phys. Rev. B, 66:165118, Oct 2002.

[48] Paola Gori-Giorgi, Francesco Sacchetti, and Giovanni B. Bachelet. Analytic static structure factors and pair-correlation functions for the unpolarized homogeneous electron gas. Phys. Rev. B, 61:7353–7363, Mar 2000.

[49] Dennis S. Greywall. Specific heat of normal liquid ^{3}He. Phys. Rev. B, 27:2747–2766, 1983.

[50] F. D. M. Haldane. 'Luttinger liquid theory' of one-dimensional quantum fluids. I. Properties of the Luttinger model and their extension to the general 1D interacting spinless Fermi gas. Journal of Physics C Solid State Physics, 14:2585–2609, July 1981.

[51] J. P. Hansen and P. Vieillefosse. Quantum corrections in dense ionized matter. Physics Letters A, 53:187–188, June 1975.

[52] Jean Pierre Hansen. Statistical mechanics of dense ionized matter. i. equilibrium properties of the classical one-component plasma. Phys. Rev. A, 8:3096–3109, Dec 1973.

[53] P. Hohenberg and W. Kohn. Inhomogeneous electron gas. Phys. Rev., 136:B864–B871, Nov 1964.

[54] M. Holzmann, D. M. Ceperley, C. Pierleoni, and K. Esler. Backflow correlations for the electron gas and metallic hydrogen. Phys. Rev. E, 68:046707, Oct 2003.

[55] Markus Holzmann and Werner Krauth. Transition temperature of the homogeneous, weakly interacting bose gas. Phys. Rev. Lett., 83:2687–2690, Oct 1999.

[56] B. Jancovici. Exchange quantum corrections in the one-component plasma. Physica A Statistical Mechanics and its Applications, 91:152–160, April 1978.

[57] M. D. Jones and D. M. Ceperley. Crystallization of the one-component plasma at finite temperature. Phys. Rev. Lett., 76:4572–4575, Jun 1996.

[58] Valentin V. Karasiev, Debajit Chakraborty, Olga A. Shukruto, and S. B. Trickey. Nonempirical generalized gradient approximation free-energy functional for orbital-free simulations. Phys. Rev. B, 88:161108, Oct 2013.

[59] Valentin V. Karasiev, Travis Sjostrom, James Dufty, and B. Trickey, S.˙Accurate homogeneous electron gas exchange-correlation free energy for local spin-density calculations. Phys. Rev. Lett., 112:076403, Feb 2014.

[60] V.V. Karasiev and S.B. Trickey. Issues and challenges in orbital-free density functional calculations. Computer Physics Communications, 183(12):2519 – 2527, 2012.

[61] S. A. Khairallah, J. Shumway, and E. W. Draeger. Path Integral Calculations of the Hydrogen Hugoniot Using Augmented Nodes. ArXiv e-prints, August 2011.

[62] Ryoichi Kikuchi. transition of liquid helium. Phys. Rev., 96:563–568, Nov 1954.

[63] Ryoichi Kikuchi, Harry H. Denman, and Charles L. Schreiber. Statistical mechanics of liquid ^{4}He. Phys. Rev., 119:1823–1831, Sep 1960.

[64] Hagen Kleinert. Path Integrals in Quantum Mechanics, Statistics, Polymer Physics, and Financial Markets. World Scientific, Singapore, 2009.

[65] M Koenig, A Benuzzi-Mounaix, A Ravasio, T Vinci, N Ozaki, S Lepape, D Batani, G Huser, T Hall, D Hicks, A MacKinnon, P Patel, H S Park, T Boehly, M Borghesi, S Kar, and L Romagnani. Progress in the study of warm dense matter. Plasma Physics and Controlled Fusion, 47(12B):B441, 2005.

[66] W. Kohn. Nobel lecture: Electronic structure of matter¯wave functions and density functionals. Rev. Mod. Phys., 71:1253–1266, Oct 1999.

[67] W. Kohn and L. J. Sham. Self-consistent equations including exchange and correlation effects. Phys. Rev., 140:A1133–A1138, Nov 1965.

[68] Stephan Kümmel and Leeor Kronik. Orbital-dependent density functionals: Theory and applications. Rev. Mod. Phys., 80:3–60, Jan 2008.

[69] Yongkyung Kwon, D. M. Ceperley, and Richard M. Martin. Effects of backflow correlation in the three-dimensional electron gas: Quantum monte carlo study. Phys. Rev. B, 58:6800–6806, Sep 1998.

[70] D.P. Landau and K. Binder. A Guide To Monte Carlo Simulations In Statistical Physics. Cambridge University Press, 2005.

[71] L.D. Landau. Theory of the fermi liquid. Soviet Physics JETP, 3:920–925, 1957.

[72] Richard W. Lee, Stephen J. Moon, Hyun-Kyung Chung, Wojciech Rozmus, Hector A. Baldis, Gianluca Gregori, Robert C. Cauble, Otto L. Landen, Justin S. Wark, Andrew Ng, Steven J. Rose, Ciaran L. Lewis, Dave Riley, Jean-Claude Gauthier, and Patrick Audebert. Finite temperature dense matter studies on next-generation light sources. J. Opt. Soc. Am. B, 20(4):770–778, Apr 2003.

[73] Mel Levy. Universal variational functionals of electron densities, first-order density matrices, and natural spin-orbitals and solution of the v-representability problem. Proceedings of the National Academy of Sciences, 76(12):6062–6065, 1979.

[74] Elliott H. Lieb. Density functionals for coulomb systems. International Journal of Quantum Chemistry, 24(3):243–277, 1983.

[75] A. P. Lyubartsev and P. N. Vorontsov-Velyaminov. Path-integral monte carlo method in quantum statistics for a system of n identical fermions. Phys. Rev. A, 48:4075–4083, Dec 1993.

[76] Richard M. Martin. Electronic Structure: Basic Theory and Practical Methods (Vol 1). Cambridge University Press, April 2004.

[77] M. Keith Matzen, M. A. Sweeney, R. G. Adams, J. R. Asay, J. E. Bailey, G. R. Bennett, D. E. Bliss, D. D. Bloomquist, T. A. Brunner, R. B. Campbell, G. A. Chandler, C. A. Coverdale, M. E. Cuneo, J.-P. Davis, C. Deeney, M. P. Desjarlais, G. L. Donovan, C. J. Garasi, T. A. Haill, C. A. Hall, D. L. Hanson, M. J. Hurst, B. Jones, M. D. Knudson, R. J. Leeper, R. W. Lemke, M. G. Mazarakis, D. H. McDaniel, T. A. Mehlhorn, T. J. Nash, C. L. Olson, J. L. Porter, P. K. Rambo, S. E. Rosenthal, G. A. Rochau, L. E. Ruggles, C. L. Ruiz, T. W. L. Sanford, J. F. Seamen, D. B. Sinars, S. A. Slutz, I. C. Smith, K. W. Struve, W. A. Stygar, R. A. Vesey, E. A. Weinbrecht, D. F. Wenger, and E. P. Yu. Pulsed-power-driven high energy density physics and inertial confinement fusion research. Physics of Plasmas, 12(5):055503, 2005.

[78] N. David Mermin. Thermal properties of the inhomogeneous electron gas. Phys. Rev., 137:A1441–A1443, Mar 1965.

[79] Nicholas Metropolis, Arianna W. Rosenbluth, Marshall N. Rosenbluth, Augusta H. Teller, and Edward Teller. Equation of state calculations by fast computing machines. The Journal of Chemical Physics, 21(6):1087–1092, 1953.

[80] B. Militzer and D. M. Ceperley. Path integral monte carlo calculation of the deuterium hugoniot. Phys. Rev. Lett., 85:1890–1893, Aug 2000.

[81] B. Militzer and R. L. Graham. Simulations of dense atomic hydrogen in the Wigner crystal phase. Journal of Physics and Chemistry of Solids, 67:2136–2143, September 2006.

[82] Vincent Natoli and David M. Ceperley. An optimized method for treating long-range potentials. Journal of Computational Physics, 117(1):171 – 178, 1995.

[83] J. A. Nelder and R. Mead. A simplex method for function minimization. The Computer Journal, 7(4):308–313, 1965.

[84] P. Nozires and D. Pines. A dielectric formulation of the many body problem: Application to the free electron gas. Il Nuovo Cimento Series 10, 9(3):470–490, 1958.

[85] J. Orenstein and A. J. Millis. Advances in the physics of high-temperature superconductivity. Science, 288(5465):468–474, 2000.

[86] A.W. Overhauser. Spin Density Waves in an Electron Gas. Phys.Rev., 128:1437–1452, 1962.

[87] W. Pauli. ber den zusammenhang des abschlusses der elektronengruppen im atom mit der komplexstruktur der spektren. Zeitschrift fr Physik, 31(1):765–783, 1925.

[88] J. P. Perdew and Alex Zunger. Self-interaction correction to density-functional approximations for many-electron systems. Phys. Rev. B, 23:5048–5079, May 1981.

[89] John P. Perdew, Kieron Burke, and Yue Wang. Generalized gradient approximation for the exchange-correlation hole of a many-electron system. Phys. Rev. B, 54:16533–16539, Dec 1996.

[90] John P. Perdew and Yue Wang. Accurate and simple analytic representation of the electron-gas correlation energy. Phys. Rev. B, 45:13244–13249, Jun 1992.

[91] François Perrot and M. W. C. Dharma-wardana. Spin-polarized electron liquid at arbitrary temperatures: exchange-correlation energies, electron-distribution functions, and the static response functions. Phys. Rev. B, 62:16536–16548, Dec 2000.

[92] E. L. Pollock and J. P. Hansen. Statistical mechanics of dense ionized matter. ii. equilibrium properties and melting transition of the crystallized one-component plasma. Phys. Rev. A, 8:3110–3122, Dec 1973.

[93] E.L. Pollock. Properties and computation of the coulomb pair density matrix. Computer Physics Communications, 52(1):49 – 60, 1988.

[94] Quantum Theory Project. Warm-dense matter. January 2012.

[95] K. S. Singwi, M. P. Tosi, R. H. Land, and A. Sjölander. Electron correlations at metallic densities. Phys. Rev., 176:589–599, Dec 1968.

[96] Travis Sjostrom and James Dufty. Uniform electron gas at finite temperatures. Phys. Rev. B, 88:115123, Sep 2013.

[97] Travis Sjostrom, Frank E. Harris, and S. B. Trickey. Temperature-dependent behavior of confined many-electron systems in the hartree-fock approximation. Phys. Rev. B, 85:045125, Jan 2012.

[98] R. G. Storer. Pathintegral calculation of the quantumstatistical density matrix for attractive coulomb forces. Journal of Mathematical Physics, 9(6):964–970, 1968.

[99] Masuo Suzuki. Generalized trotter's formula and systematic approximants of exponential operators and inner derivations with applications to many-body problems. Communications in Mathematical Physics, 51(2):183–190, 1976.

[100] S. Tanaka and S. Ichimaru. Thermodynamics and Correlational Properties of Finite-Temperature Electron Liquids in the Singwi-Tosi-Land-Sjölander Approximation. Journal of the Physical Society of Japan, 55:2278, July 1986.

[101] B. Tanatar and D. M. Ceperley. Ground state of the two-dimensional electron gas. Phys. Rev. B, 39:5005–5016, Mar 1989.

[102] J.J. Thomson. Cathode rays. Proceedings of the Royal Institution, (1-14), 1897.

[103] D J Thouless. Exchange in solid 3 he and the heisenberg hamiltonian. Proceedings of the Physical Society, 86(5):893, 1965.

[104] S. B. Trickey, V. V. Karasiev, and A. Vela. Positivity constraints and information-theoretical kinetic energy functionals. Phys. Rev. B, 84:075146, Aug 2011.

[105] Norm M. Tubman, Jonathan L. DuBois, and Berni J. Alder. Recent Results in the Exact Treatment of Fermions at Zero and Finite Temperature. In Tanaka, S and Rothstein, SM and Lester, WA, editor, ADVANCES IN QUANTUM MONTE CARLO, volume 1094 of ACS Symposium Series, pages 41–50. Amer Chem Soc, Phys Chem Div; Silicon Graph Inc, 2012. Symposium on Advances in Quantum Monte Carlo, Honolulu, HI, DEC 15-20, 2010.

[106] S. H. Vosko, L. Wilk, and M. Nusair. Accurate spin-dependent electron liquid correlation energies for local spin density calculations: a critical analysis. Canadian Journal of Physics, 58(8):1200–1211, 1980.

[107] M. A. Voznesenskiy, P. N. Vorontsov-Velyaminov, and A. P. Lyubartsev. Path-integralexpanded-ensemble monte carlo method in treatment of the sign problem for fermions. Phys. Rev. E, 80:066702, Dec 2009.

[108] E. Wigner. On the interaction of electrons in metals. Phys. Rev., 46:1002–1011, Dec 1934.

[109] B. Wilson, V. Sonnad, P. Sterne, and W. Isaacs. Purgatorioa new implementation of the inferno algorithm. Journal of Quantitative Spectroscopy and Radiative Transfer, 99(13):658 – 679, 2006. Radiative Properties of Hot Dense Matter.

[110] F. H. Zong, C. Lin, and D. M. Ceperley. Spin polarization of the low-density three-dimensional electron gas. Phys. Rev. E, 66:036703, Sep 2002.